Dissertation

submitted to the

Combined Faculty of Natural Sciences and Mathematics

of the Ruperto Carola University Heidelberg, Germany

for the degree of

Doctor of Natural Sciences

Presented by

M.Sc. Hannah Sonntag

born in: Seeheim-Jugenheim

Oral examination: 27th September 2019

Elucidating astrocyte and neuron interactions

using genetically encoded fluorescent indicators

Referees: Prof. Dr. Andreas Draguhn

Dr. Rolf Sprengel

Summary

Astrocytes are organized in what can be regarded as parallel networks to local neuronal networks. On the cellular level astrocytes immediately react to stimulated neuronal activity by transient increases in intracellular calcium concentration ($[Ca^{2+}]_i$) which results *in vitro* in a vesicular release of so-called gliotransmitters such as ATP, D-serine and glutamate. In turn these gliotransmitters directly modulate synaptic transmission. Those synapses are regarded as tri-partite connections composed of the pre- and post-synapse enveloped by astrocyte processes. Several mouse models suggested astrocytes as key entities to tune synaptic transmission to vigilance states of synchronized neuronal activity oscillations. However, due to conflicting findings it is still under debate whether gliotransmission takes place under physiological conditions and, in particular, whether and how the activity of a single astrocyte or the general astrocyte population is an indicator for altered coordinated activity of a neural network.

In the presented study the bidirectional communication of astrocytes and neurons was investigated. First, by a glia-neuron tracing approach *in vivo* and second by the simultaneous recording of neuronal and astrocytic activity during pharmacologically-induced oscillatory activity of cultured hippocampal slices. The tracing approach demonstrated in multiple independent experiments, that the rAAV-delivered retrograde tetanus toxin heavy chain tracer (eGFP-TTC) in hippocampal neurons is transferred to retrogradely connected neurons but is not translocated to, or between astrocytes. This excludes the existence of the neuron-like presynaptic target structures in astrocytes, exploited by eGFP-TTC. Likewise, eGFP-TTC is not transferred from astrocytes to neurons. Thus, the eGFP-TTC experiments cannot be used for tracing of neurons in putative networks build of tripartite synapses and moreover do not support the gliotransmission hypothesis. For the population analysis during neuronal oscillations, astrocyte $[Ca^{2+}]_i$ and neuronal $[Ca^{2+}]_i$ transients were recorded simultaneously by neuron- and astroglia-transduced Ca^{2+} indicators jRGeco and GCaMP6f, respectively. In both cell types the frequency and the kinetics of $[Ca^{2+}]_i$ transient were not affected by the pharmacologically induced oscillations. Temporal cross-correlation analysis of the activity failed to identify any correlations in astrocytes and neuronal $[Ca^{2+}]_i$ signals and could not identify any preferred $[Ca^{2+}]_i$ transient sequence patterns. From these observations it can be concluded, that in the pharmacologically induced oscillation model either the $[Ca^{2+}]_i$ transients in both cell populations are independent from the conditions and from each other, or that the applied virus delivered activity indicators combined with epifluorescence imaging are insufficient to allow detection of subtle correlations in these cells.

Zusammenfassung

Astrozyten sind in parallelen Netzwerken zu lokalen neuronalen Netzwerken organisiert und es wurde wiederholt nachgewiesen, dass einzelne Astrozyten *in vitro* direkt auf stimulierte neuronale Aktivität mit transienten Anstiegen der intrazellulären Kalziumkonzentration $[Ca^{2+}]_i$ reagieren. Diese Transienten führen zu einer vesikulären Freisetzung von Transmittern wie z.Bsp. ATP, D-Serin oder auch Glutamat durch die Astrozyten, die sog. Gliotransmission. Diese Transmitter beeinflussen direkt die neuronale synaptische Signalübertragung, weshalb man seit einigen Jahren bestimmte Synapsen als drei-, statt zwei-teilige Struktur versteht. Der dritte Teil wird hierbei von Astrozytenausläufern gebildet und umhüllt die Prä- und Postsynapse. *In vivo* Mausmodelle suggerieren, dass die Astozytenaktivität synchronisierte Oszillationen in der neuronalen Aktivität wesentlich beeinflussen. Es ist jedoch nach wie vor ist umstritten, ob Gliotransmission unter physiologischen Bedingungen stattfindet und insbesondere, ob und wie Veränderungen in der Aktivität von neuronalen Netzwerken durch die Aktivität einzelner Astrozyten oder der Gesamtheit der Astrozytenpopulation gemessen werden kann.

In der vorliegenden Studie wurde die bidirektionale Kommunikation zwischen Astrozyten und Neuronen im Detail zum einen mit einem Glia-Neuron-Tracing-Ansatz *in vivo* und zum anderen mit simultanen Aktivitätsmessungen von Neuronen und Astrozyten während pharmakologisch induzierter neuronaler Oszillationen in Gehirnschnittkulturen, untersucht. Im Tracing-Ansatz konnte eindeutig gezeigt werden, dass der von rAAV gelieferte retrograde Tracer (eGFP-TTC), welcher auf Tetanustoxin basiert, von hippocampalen Neuronen retrograd auf synaptisch verbundene Neurone übertragen wird, dabei jedoch nicht auf Astrozyten. Daher kann geschlussfolgert werden, dass die von eGFP-TTC benötigten Neuronen-ähnlichen präsynaptischen Strukturen nicht bei Astrozyten existieren. Weiterhin bedeutet das Ergebnis, dass das präsentierte Tracing-system nicht für die Kartierung von neuronalen Netzwerken, welche sich drei-teilige Synapsen mit Astrozyten teilen, genutzt werden kann. Für die Aktivitätsmessungen wurden gleichzeitig $[Ca^{2+}]_i$ -Transienten von Astrozyten und Neuronen mit den zellspezifisch transduzierten Ca^{2+}-Indikatoren jRGeco bzw. GcaMP6f gemessen. In beiden Zelltypen wurden die Frequenz und die Kinetik der $[Ca^{2+}]_i$ transienten durch Gamma-Oszillationen nicht beeinflusst. Auch Kreuzkorrelationsanalysen von Astrozyten- und Neuronenaktivität konnten keine zeitlichen Zusammenhänge oder bevorzugte $[Ca^{2+}]_i$ -Sequenzmuster identifizieren. Diese Ergebnisse zeigen, dass das in dem pharmakologisch induzierten Oszillationsmodel entweder die Astrozyten- oder die Neuronenaktivität unabhängig voneinander und von den Oszillation sind, oder dass die angewandten Methoden, wie z.B. die viral transduzierten Kalziumindikatoren oder die Verwendung von Epifloureszenzmikroskopie, nicht ausreichen um subtile Muster in der Aktivität dieser Zellen zu detektieren.

Declaration

I, Hannah Sonntag, hereby declare that the work in this thesis represents my original research results. The thesis has been written by myself using the references and resources indicated. Any work of other has been appropriately marked. The work has been conducted under the joint supervision of Prof. Dr. Andreas Draguhn and Dr.Rolf Sprengel. This thesis is being submitted for the degree of Doctor of Natural Sciences at Heidelberg University, Germany, and has not been presented to any other university as part of an examination or degree.

Date

Hannah Sonntag

Table of content

Abbreviations

	$[Ca^{2+}]_i$	Intracellular calcium concentration
A	AAV	Adeno-associated virus
	AChR	Acetylcholine receptors
	ACSF	Artificial cerebrospinal fluid
	AMPAR	α-amino-3-hydroxy-5-methyl-4-isoxazolepropionic acid receptor
	ATP	Adenosine triphosphate
	AP	Anterior-posterior
B	bp	Base pair
	BSA	Bovine serum albumin
C	cAMP	Cyclic adenosine monophosphate
	CA	*Cornu ammonis*
	CCH	Carbachol
	CCH-GM	Carbachol induced gamma oscillations
	cm	Centimetre
	contra	Contralateral
D	DAPI	4',6-Diamidino-2-phenylindole
	DF	Dorsal fornix
	DG	Dentate gyrus
	DIO	Double inverted orientation
	DMEM	Dulbecco's modified eagle medium
	DNA	Deoxyribonucleic acid
	dNTP	Deoxyribose nucleoside triphosphate
	DV	Dorso-ventral
E	EC	Entorhinal cortex
	EEG	Electroencephalography
	eGFP	Enhanced green fluorescent protein
F	FCS	Fetal calf serum
	FISH	Fluorescence in situ hybridisation
G	$GABA_AR$	γ-aminobutyric acid receptor type A
	GBZ	Gabazine
	GFAP	Glial fibrillary acidic protein
	GFP	Green fluorescent protein
	gr	Granular layer
H	HEK293	Human embryonic kidney 293 cell line
I	IP3	Inositol-3-phosphate
	i.p.	Intraperitoneal
	IF	Immunofluorescence
	ipsi	Ipsilateral
K	KO	Knock out
	KusO	Kusabira orange
	LB	Lysogeny broth medium
L	LD	Lateral dorsal nucleus of the thalamus

	LFP	Local field potential
	LS	Lateral septal nucleus of the thalamus
	LTP	Long term potentiation
M	mAChR	Metabotropic acetylcholine receptor
	MCS	Multiple cloning site
	MEM	Minimum essential medium
	mGluRs	Metabotropic glutamate receptors
	MPI	Max Planck Institute
N	NeuN	Neuronal nuclear antigen
	NGS	Normal goat serum
	NMDAR	N-methyl-D-aspartate receptor
O	or	Stratum oriens
P	PBS	Phosphate buffered saline
	PCR	Polymerase chain reaction
	PFA	Paraform aldehyde
	Pks	Peaks
	pM	Picomolar
	po	Polymorph layer
	py	Pyramidal layer
R	ra	Stratum radiatum
	rAAV	Recombinant adeno-associated virus
	RNA	Ribonucleic acid
	ROI	Region of interest
	rpm	Rounds per minute
	RSP	Restrosplenial cortex
	RT	Room temperature
S	s	Second
	SD	Standard deviation
	SEM	Standard error of the mean
	Syn	Synapsin promoter
T	TAE	Tris-Acid-EDTA buffer
	TB	Terrific broth medium
	TeNT	Tetanus neuro toxin
	TTC	Tetanus toxin c-fragment
	TTX	Tetrodotoxin
W	WT	Wild type

1. Introduction

Since the discovery of astrocytes as cellular structures in the late 19th century by Michael Lenhossek, scientists speculated and discussed their functional importance (Kettenmann and Ransom, 2005). Astrocytes are electrically silent partners of neurons (Petersen et al., 2005). Today it is well established, that astrocytes, which surround neurons, are critical for numerous tasks, such as establishing the blood brain barrier (Bundgaard and Abbott, 2008) and the clearance of extracellular potassium and neurotransmitters released from neurons (Djukic et al., 2007). More recently it has been proposed that astrocytes also maintain energy homeostasis by shuttling metabolites (Allaman et al., 2011), and by establishing neuro-vascular coupling, to adjust blood flow depending on neuronal activity (Iadecola and Nedergaard, 2007; Nizar et al., 2013). A number of studies also provided evidence that astrocytes are involved in pathological processes for example in Alzheimer's disease (von Bernhardi, 2007; Taylor et al., 2007).

Thus, there is a plethora of functions identified and putative pathways to regulate these, drafting a very complex image of the astrocytes' physiological performance. It is challenging to dissect how astrocytes orchestrate their versatile functions and while more and more details are explored on how they achieve these tasks, some results are contradicting and require further and deeper investigation.

Since astrocytes and neurons coexist in all brain areas, it is crucial to understand if and how they cooperate and how one influences the others performance. This aspect has been neglected in the past and only recently the contribution of astrocytes to physiological processes in the brain have been started to be elucidated.

1.1 The astrocyte network

Named after their shape, astrocytes in general have small cell bodies (10 – 20 μm) compared to their neighbouring neurons and have numerous so-called perisynaptic nano-processes spanning non-overlapping territories (Bushong et al., 2002; Jayant et al., 2017). Organized in these territories, astrocytes form a network, parallel to that of the neurons, by gap-junction coupling. Gap-junctions are formed by connexons, hetero-hexamers of the connexin (Cx) proteins. Astrocytes specifically express the connexin subtypes Cx43 and Cx30 (Giaume et al., 2010). These hexamers sit in the plasma membrane and bind connexons from adjacent astrocytes in order to

form gap-junctions (Theis et al., 2005). These aqueous channels are roughly 1.5 nm in diameter and are permeable for small molecules between 1 and 1.2 kDa (Bruzzone et al., 2003; Dermietzel et al., 1989). Therefore, gap-junction coupling facilitates extensive network communication by allowing direct exchange of ions and small molecules such as calcium ions (Ca^{2+}), inositol-3-phosphate (IP3), and cyclic adenosine monophosphate (cAMP) from one astrocyte to another. The formation of these networks is by no means global but is selective to subpopulations of astrocytes. One example are astrocytes of the olfactory bulb extra- and intraglomerular region. Infusing one astrocyte in the extraglomerular region with gap-junction permeable indicator dye labelled all surrounding astrocytes within the region of the glomerulus. The dye however, would not diffuse to the intraglomerular region but stop directly at the border of the next glomerulus (Bushong et al., 2002). Similar examples can be seen throughout the brain, especially in strictly compartmentalized regions such as the somatosensory cortex and the hippocampus (Dallérac et al., 2018). Interestingly, in the latter the coupling strength differs in between regions; CA1 astrocytes show stronger coupling compared to their CA3 neighbours (D'Ambrosio et al., 1998). The selective gap-junction coupling of astrocytes is thought to be achieved by heterogeneous expression of the Cx proteins which is in turn depending on the tissue type as well as the developmental stage (Tsai et al., 2012). The exact functional relevance of intercellular coupling and its differential characteristics depending on regions is unknown. Compartmentalization, however, coincides with large functional neuronal territories (Medina et al., 1999) hinting towards an important role of these astrocyte networks in modulating and supporting neurons in their functions. Further, conditional knock-out (KO) animals for Cx30 and Cx43 showed impaired neuronal functions (Wallraff et al., 2006). While the electrophysiological properties of the Cx-deficient astrocytes remained the same, the potassium buffering properties and the threshold for epileptiform activity in slices obtained from Cx30 and Cx40 deficient mice were lowered (Wallraff et al., 2006). Moreover, Chever et al. 2016 showed that a loss of Cx43 and Cx30 results in an increase of bursting incidences in disinhibited slice preparations, concluding that the astrocyte network is involved in coordination of neuronal activity (Chever et al., 2016). While it remains unclear how exactly astrocyte gap-junction coupling contributes to neuronal coordination, the anatomical features of compartmentalized astrocyte networks as well as functional consequences in Cx KO mouse lines implicate that astrocyte to astrocyte communication is vital also for neuronal networks (Pannasch and Rouach, 2013). In the past, studies focusing on astrocytes especially *in vitro* failed to take this important functional aspect into consideration, therefore omitting a prominent feature that most likely has an impact also on astrocyte to neuron communication.

1.2 The tripartite synapse

It has been proposed that neurons not only sit embedded in the above described astrocyte network, but that astrocytes are an important and intimate partner in synaptic transmission. Due to their spongiform morphology a single astrocyte is potentially in contact with an estimated 100.000 synapses of about 4 – 8 different neurons (Bushong et al., 2002). Anatomical studies (Ventura and Harris, 1999) showed that astrocytes envelope synapses and recent functional assays showed that astrocytes can shape synapses by secreting signalling molecules (Di Castro et al., 2011; Henneberger et al., 2010; Jourdain et al., 2007; Miller et al., 2019; Pascual et al., 2005; Shigetomi et al., 2013). Therefore, the model of the tri-partite synapse was proposed adding to the pre- and the post synapse a third interaction partner; the astrocyte (Araque et al., 1999).

The details how astrocytes influence or even participate in neurotransmission are in the process of being elucidated and a number of possible mechanisms are being discussed. It is undisputed that astrocytes directly react to synaptic activity, which can be observed with fluorescent Ca^{2+} indicators (Tang et al., 2015; Verkhratsky and Parpura, 2013). Almost three decades ago in 1990 Cornell-Bell was able to show, that astrocytes exhibit intracellular calcium transients ($[Ca^{2+}]_i$) in response to neuronal stimulation (Cornell-Bell et al., 1990). With the development of genetically encoded Ca^{2+} sensors, such as GCaMP (Nakai et al., 2001) and improvements in imaging techniques (Bindocci et al., 2017) a plethora of studies was done, probing the pathways triggering astrocyte $[Ca^{2+}]_i$ transients and their downstream effects.

One example are metabotropic glutamate receptors (mGluRs) such as mGluR5 - a neurotransmitter receptor expressed in astrocytes. Activation of mGluR5 results in $[Ca^{2+}]_i$ transients in astrocytes, by release of Ca^{2+} from internal stores via the IP3 second-messenger pathway (Panatier et al., 2011; Porter and McCarthy, 1996). In turn glutamate-triggered $[Ca^{2+}]_i$ transients have been linked to a number of effects such as changes in vasodilation (Attwell et al., 2010; Mulligan and MacVicar, 2004) as well as influences on synaptic plasticity by release of transmitters such as D-serine, purines and glutamate itself (Di Castro et al., 2011; Jourdain et al., 2007; Min and Nevian, 2012; Panatier and Robitaille, 2018; Pirttimaki et al., 2017). This mechanism of Ca^{2+} -dependent vesicular release of transmitters is called gliotransmission (Araque et al., 2014). The discovery of gliotransmission is in line with the functional assay proving that astrocytes *in vitro* use the most common pathway for Ca^{2+}-dependent vesicular release, the SNARE complex (Schwarz et al., 2017; Zhang et al., 2004). This complex consists of a

set of proteins tethered to the inside of the cell membrane (syntaxin and SNAP-25) and to the outside of the vesicle membrane (synaptobrevin). Upon Ca^{2+} influx into the cell the complex is formed, and the vesicle can fuse with the membrane, emptying its cargo into the extracellular space (Jahn and Südhof, 1999). Together, these findings suggest, that astrocytes sense local neuronal activity through neurotransmitter receptors and directly react by gliotransmission to adjust local neurotransmission properties.

In vivo astrocyte $[Ca^{2+}]_i$ imaging has confirmed that local glutamate signals enhance $[Ca^{2+}]_i$ astrocyte activity, and found that locomotor activity can trigger $[Ca^{2+}]_i$ transients *in vivo* in the cerebellum (Nimmerjahn et al., 2009) as well as in the cortex (Paukert et al., 2014). In the latter case it was found that administering the broad inhibitor of adrenergic, serotonergic and histaminergic receptors, trazodone (Cusack et al., 1994), reduced locomotion-induced $[Ca^{2+}]_i$ transients. Further studies showed that long-range cholinergic and noradrenergic (Ding et al., 2013; Fellin et al., 2009; Takata et al., 2011) neuromodulatory inputs trigger astrocyte $[Ca^{2+}]_i$ transients. This adds the incorporation of global inputs depending on brain states like wakefulness, to astrocyte functions (Papouin et al., 2017; Verkhratsky and Nedergaard, 2017).

Many of the downstream effects of $[Ca^{2+}]_i$-dependent release of transmitters from astrocytes have been assessed with the so-called dominant negative SNARE transgenic mouse line (dn-SNARE mouse). Since SNARE-dependent release from astrocytes has been shown to be the secretion mechanism *in vitro,* an *in vivo* model was developed where this mechanism is inhibited. In the dn-SNARE mouse the complex formation is blocked in astrocytes by transgenic expression of the untethered synaptobrevin recognition motif. The free cytosolic recognition motif forms the SNARE complex in the absence of vesicles and therefore prevents the complex formation with endogenous vesicle-tethered syntaxin (Pascual et al., 2005; Zhang et al., 2004).

With the dn-SNARE mouse it was demonstrated that neuronal transmission is directly affected when vesicular release from astrocytes is blocked. In hippocampal slice experiments from dn-SNARE mice, purinergic signalling from astrocytes tonically supresses synaptic transmission (Pascual et al., 2005). Moreover, astrocytes were identified as a source for extracellular D-serine, an NMDA-receptor co-activator. Blocking release mechanisms from astrocytes results in a decrease in extracellular available D-serine. As a result, less NMDA-receptors could be activated and are available for NMDA-dependent long term potentiation (LTP). This finding is linked to the previously described long-range cholinergic inputs (Papouin et al., 2017).

The involvement of astrocytes in LTP-formation was moreover shown in a recent study using chemogenetic activation of CA1 astrocytes with designer receptors exclusively activated by

designer drugs (DREADDs). DREADD activation showed that astrocytes can trigger *de novo* LTP when stimulated, concluding that astrocyte activity alone is sufficient to trigger LTP in a $[Ca^{2+}]_i$ dependent manner, supposedly by secretion of transmitters (Adamsky et al., 2018).

Taken together, these studies suggest a complex bi-directional communication between astrocytes and neurons. Astrocyte Ca^{2+} activity was shown to have in part opposing effects, as it may dampen or potentiate synaptic transmission (Papouin et al., 2017; Pascual et al., 2005). However, the exact mechanisms how these effects are orchestrated are not known. Nonetheless, these findings outline a model of astrocytes sensing global vigilance states and in response tune synaptic transmission accordingly. Thus, astrocytes increase the dynamic range of activity-induced synaptic plasticity (Bazargani and Attwell, 2016; Poskanzer and Yuste, 2016; Shigetomi et al., 2016).

1.3 Gliotransmission: still an open question

As outlined in the previous chapter, a number of bi-directional signalling pathways between astrocytes and neurons have been described. However, it is an ongoing discussion which signalling pathways are of functional relevance under physiological conditions, since most evidence was obtained either by artificial stimuli or in *in vitro* not reflecting all *in vivo* aspects.

There are several *in vivo* experiments that put some doubts on the postulated gliotransmission. One is the observation that KO-mice of the astrocyte specific IP3 receptor subtype 2 (IP3R2), show normal behaviour including regular learning and memory despite a substantial loss of $[Ca^{2+}]_i$ signals in astrocytes. In brain slice experiments from IP3R2 KO animals, there hippocampal synaptic transmission and LTP was normal (Petravicz et al., 2008, 2014). This puts some doubts on the involvement of astrocyte $[Ca^{2+}]_i$ dependent processes in complex cognitive functions. In line with this finding are the results from another transgenic mouse line targeting astrocytes (Fiacco et al., 2007). This mouse line expresses the spinal cord specific G-protein coupled receptor (GPCR) MrgA1R in astrocytes of the forebrain. The MrgA1R ligand is not present in the forebrain unless provided experimentally. Experimental stimulation of MrgA1R receptors in the forebrain of the transgenic mouse resulted in $[Ca^{2+}]_i$ transients in astrocytes, similar to transients evoked by glutamate in astrocytes of WTs. However, no effect on neuronal activity or synaptic transmission was found. Thus, it is not clear whether *in vitro* observed gliotransmission is of physiological importance (Fiacco and McCarthy, 2018). Likewise, strong stimulation of astrocytes using DREADDs may not reflect the physiological process (Adamsky et al., 2018). Another potential issue in gliotransmission research are manipulations

that may directly influence neurons. Fiacco et al argue, that for example the dn-SNARE mouse, which has been used in multiple studies to provide evidence of gliotransmission, is not strictly astrocyte specific, and the SNARE mechanism is also blocked in neurons (Fiacco and McCarthy, 2018). Therefore, those experimental results have to be reviewed carefully and potential biases or unspecific side-effects of applied methods have to be revisited to avoid misleading conclusions concerning the effects on neuronal signalling based on altered gliotransmission.

Through the described controversy in published results it is obligatory, that tools to investigate astrocytes and the tri-partite synapse have to be carefully selected and that better tools are required to disentangle bi-directional astrocyte – neuronal communication.

1.4 Astrocytes' role in neuronal oscillations

Neuronal ensembles describe subpopulations of neurons acting in synchrony and therefore giving rise to oscillation patterns that correlate with the behavioural performance (Buzsaki and Draguhn, 2004). Oscillations can be measured i.e. *in vivo* in electroencephalograms (EEGs) or in extracellular recordings *in vivo* or in brain slices. Whether astrocyte activity is correlated with neuronal oscillatory activity is still an open question.

1.4.1 Neuronal oscillations

Synchronous oscillatory brain states were first identified in "idling" brain states such as during sleep or anaesthesia (Steriade, 2001). Detailed biophysical studies revealed how single neurons adjust their electrophysiological properties to resonate with different types of oscillations (Buzsaki and Draguhn, 2004). Moreover, it was shown that the same neuronal oscillatory assemblies, active during sleep, were active in the wake phase. Thus, oscillations are thought to link single neuronal activity to global neuronal outputs such as behaviour, memory and learning processes and consciousness (Buzsaki, 2006). Disruption of oscillatory patterns in human EEG measurements have also been linked to neurological disorders such as schizophrenia, indicating oscillations to be necessary for maintaining physiological brain functions (Ahnaou et al., 2017). Different types of oscillations are known and range from 0.05 Hz to 500 Hz and are classified according to their frequency. These oscillations can occur simultaneously in different brain regions (Csicsvari et al., 2003; Steriade, 2001).

The presented study focuses on so called gamma oscillations that have a frequency range of 30 – 100 Hz and can be measured in humans in EEG as well as in rodents in both the cortex as well as the hippocampus. In rodents these oscillations in the hippocampus were linked

to specific behaviours. For example, gamma oscillations occur during exploration and typically coexist with theta oscillations (Bragin et al., 1995).

Gamma activity can be evoked in *in vitro* hippocampal slices through several types of manipulations including electrical or pharmacological manipulation (Bartos et al., 2007). Especially from pharmacological manipulations three prominent neurotransmitter receptors involved in gamma oscillations were identified; mGluRs, muscarinic acetylcholine receptor (mAChRs) and kainate receptors (kainate-R) (Fisahn et al., 1998, 2004; Whittington et al., 1995). For example, the mAChR agonist carbachol (CCH) induces gamma oscillations, which is thought to mimic cholinergic input *in vivo* from the septum to the hippocampus (Fisahn et al., 1998; Shute and Lewis, 1963). Gamma oscillations induced by CCH or mGluR stimulations are abolished by $GABA_A$ blockers, but only CCH-induced gamma oscillation is also blocked with AMPA receptor antagonists (Fellous and Sejnowski, 2000; Hájos et al., 2000). From these findings it can be concluded that the three different induction protocols result in gamma oscillations relying on different pathways. While kainite-R and mGluR induced gamma oscillations require only fast $GABA_A$-mediated inhibitory pathways, thus most likely involving interneurons, the mAChR-dependent gamma oscillations also rely on rapid excitatory signalling. All three forms are most likely relevant *in vivo* since gamma oscillations may occur in different state-dependent manners (Bartos et al., 2007).

From single cell electrophysiological recordings, it is known that principal neurons in CA3 fire action potential phase-related to gamma oscillation, but each neuron only participates in approximately 5% of the cycles (Fisahn et al., 1998).

Another aspect investigated in context of the of gamma oscillations models is the involvement of gap-junctions between neurons. By pharmacological blocking gap-junctions the power of gamma oscillations was decreased. However, gamma oscillations where not entirely abolished (Traub et al., 2001). This was confirmed by the Cx36 deficient mouse line. Cx36 is thought to be mostly expressed in interneurons. Cx36 deficient mice had a significant decrease in gamma power compared with WT controls during wheel running. This suggests that Cx36 interneural gap-junctions selectively contribute to gamma oscillations (Traub et al., 2001).

1.4.2 Astrocyte activity during gamma oscillations

Most of the published literature examined gamma oscillations in organotypic slice preparations. Therefore, astrocytes and other glial cells are also present in these slices and the applied manipulations also affected these cells. This fact however was not taken into consideration in the interpretation of these results. As described above it is well established, that astrocytes express a battery of neurotransmitter receptors (Verkhratsky and Nedergaard, 2017). Therefore,

pharmacological manipulations applied to trigger gamma oscillations could also trigger processes in the astrocytes which may contribute to the development of gamma oscillations *in vitro.*

Very little research has been done in elucidating astrocytes' contribution to oscillatory brain states. It has been shown in one study by Poskanzer et al. that astrocytes-Ca^{2+}-dependent pathways are required for cortical oscillatory state switches *in vivo* (Poskanzer and Yuste, 2016). By combining *in vivo* Ca^{2+} and glutamate imaging they could show that astrocytes release glutamate in a $[Ca^{2+}]_i$ dependent manner. This, in turn triggers a neuronal circuit shift to slow oscillatory states, believed to be important for memory consolidation during slow wave sleep (Ji and Wilson, 2007; Poskanzer and Yuste, 2016).

Another study by Lee *et al.* focused on hippocampal gamma oscillations in slice cultures (Lee et al., 2014). In this study astrocyte $[Ca^{2+}]_i$ activity was measured during CCH-induced gamma-oscillations. When vesicular release from astrocytes was blocked by lenti viral astrocyte-specific expression of the toxic light chain of the tetanus neurotoxin (TeNT) from *Clostridium tetani*, the CCH-induced gamma oscillations were less persistent and did not last as long compared to control slices. This finding was confirmed *in vivo* with a triple transgenic mouse expressing astrocyte specific TeNT. EEG measurements in these mice showed reduced gamma power and behaviour experiments revealed impairments in novel object recognition. In conclusion this study links the lack of astrocyte $[Ca^{2+}]_i$-dependent release of glutamate to learning impairment by decreasing power in gamma oscillations. This study is in accordance with the findings from Poskanzer *et al.* who demonstrated the involvement of astrocytes in the regulation of oscillatory brain states (Poskanzer and Yuste, 2016).

However it still remains unresolved, how astrocyte $[Ca^{2+}]_i$ activity is directly affecting neurons on a cellular level and how this activity can modulate oscillations. It is known that CCH-induced gamma oscillations require both hippocampal excitatory and inhibitory circuits. Thus, the proposed model of glutamate gliotransmission could mean that neurons require the local glutamate signal from astrocytes to orchestrate their rhythmic activity by increasing the likelihood for action potentials of local neurons (Lee et al., 2014). Other modes of interaction where for example astrocyte $[Ca^{2+}]_i$ activity follows neuronal activity are possible as well (Poskanzer and Molofsky, 2018). With the current state of knowledge, however the link between the development of gamma oscillations and the involvement of astrocytes is missing. Identifying the cellular underpinnings of these regulatory mechanisms requires understanding both, the neuronal as well as the astrocyte contributions.

1.5 Retrograde tracer systems

Despite countless investigations regarding the *in vivo* situation of the bi-directional astrocyte-neuron communication, no clear conclusion is emerging. Both cell types are complex and derive from common precursor cells (Freeman, 2010), making any targeted manipulation prone to affect the other celltype, too. Distinguishing true effects from off-target effects is a major issue in this research field and faithful tools to perform this tasks have to be developed and carefully investigated.

In neuronal connectomics studies, retrograde tracer systems are used to dissect distinct neuronal ensembles. One example is the nontoxic heavy chain of the TeNT (TTC) which can bind to neuronal terminals and is readily internalized by the recycling of synaptic vesicles were the light chain exerts its toxic action by blocking the vesicle release (Price et al., 1975). Given that the bacteria are mostly found in soil and animal waste, the toxin usually takes a route from injuries in the periphery through the axon of motor neurons to be transported to the CNS (Lalli et al., 2003). The light chain of TeNT exerts the toxic effects by preventing the release of neurotransmitters from inhibitory neurons into the synaptic cleft. The effect is achieved by proteolysis of the SNARE proteins, required for the vesicular release (Munro et al., 2001). The TeNT heavy chain is non-toxic and facilitates binding and internalization of TeNT into the cytosol (Lalli et al., 2003). TTC binds with low affinity to polysialogangliosides (Herreros et al., 2000a) but protease experiments suggest the existence of another unidentified protein receptor bound by TTC (Herreros et al., 2000b). The uptake mechanism of the TTC is not entirely clear but existing data suggest two different uptake mechanisms a) in the presynapse in the neuromuscular junction, which as aforementioned is the usual first entry point and b) for entry into the axons of the interneurons in the CNS (Roux et al., 2006). The latter is thought to be depolarization and Ca^{2+} dependent (Miana-Mena et al., 2002).

By fusing the TTC fragment to reporter proteins like LacZ or GFP, the TTC fragment was used as a tracer as well as potential transporter for therapeutics (Kissa et al., 2002). Buettner-Ennever et al. successfully transported TTC-coupled therapeutics as well as reporter proteins across the blood brain barrier, proving that the internalization mechanism exploited by TTC is not disturbed when fused to other proteins (Buettner-Ennever et al., 1981). A number of studies assessed neuronal connectivity by coupling to reporter proteins using different approaches, such as delivering the TTC fusion protein by directly injecting the purified protein (Perreault et al., 2006), by transfection of an expression plasmid encoding the TTC-reporter into the peripheral tissue (Coen et al., 1997) or by engrafting eGFP-expressing cultured cells in the CNS (Kissa et al.,

2002). These studies identified, for example, the connection of motor neurons and the brain stem (Coen et al., 1997) and CNS wiring of the striatum to motor cortex (Kissa et al., 2002).

The presented literature exclusively focused on the neuronal tracing properties of the TTC system. Astrocytes are in close contact to neurons as well as in close proximity to synapses. Moreover, they express and use vesicular release mechanisms similar to neurons *in vitro* and putatively *in vivo*. It is unclear however, whether the TTC fragment interacts with astrocytes and whether it is a feasible tool for defining the "connectome" of astrocytes. As mentioned above, tools to investigate astrocyte to neuron interaction suffer from non-specific targeting of applied manipulations. The TTC-tracer might be used to dissect astrocyte-neuron networks which are in direct contact to each other and thus potentially allow examining the minute details of their interaction.

1.6 Objectives

Astrocytes have been shown to respond to neuronal activity by $[Ca^{2+}]_i$ transients, resulting in a number of different effects. However, the undisturbed physiological *in vivo* astrocyte-neuron interactions remain elusive due to limited accessibility.

In the presented study the bidirectional astrocyte-neuron communication was investigated in two different approaches. First, I tested on a histological level whether TTC can be exploited as a tool for specific targeting of astrocyte-neuron ensembles. The question was whether the eGFP-TTC fusion protein if delivered directly into the hippocampus is transferred "transsynaptically" a) from neurons to astrocytes, b) from astrocytes to neurons or c) from astrocytes to astrocytes. Results from these experiments can deliver proof of the existence of gliotransmission, since a "transsynaptic" transfer of the TTC-fragment from neurons to astrocytes, would show that astrocytes use similar release mechanisms as neurons *in vivo*. Moreover, TTC-mediated transfer from and to astrocytes poses a potential new labelling tool for distinct astrocyte-neuron ensembles, which could be used in future applications to elucidate the minute details of their interaction.

Second, I aspired to further investigate the interplay of astrocytes and neurons during gamma oscillations. Lee et al. proposed gliotransmission of glutamate to be a central contribution to gamma oscillations (Lee et al., 2014). The presented thesis aims to complement the findings by measurement of astrocyte $[Ca^{2+}]_i$ transient simultaneously with neuronal $[Ca^{2+}]_i$ transient during CCH-induced gamma. The aim was to characterize astrocyte $[Ca^{2+}]_i$ signalling properties such as frequency and kinetics change during gamma oscillations and to correlate the $[Ca^{2+}]_i$ transients in astrocytes to the neuronal $[Ca^{2+}]_i$ transients. This could answer the question

whether $[Ca^{2+}]_i$-dependent glutamate release from astrocytes results in increased likelihood for neighbouring neurons to exhibit action potentials, which would indicate a mechanism of astrocyte control on gamma oscillation. Likewise, I asked whether the activity of a single astrocyte or an astrocyte population can be used as an indicator for different neuronal oscillatory states.

2. Results

2.1 EGFP-TTC fusion protein: an astrocyte to neuron tracer?

Astrocyte processes are not only in close proximity to synapses but have also been shown to react to neuronal activity and in turn manipulate how neurons react to neuronal activity (Shigetomi et al., 2016). The exact mechanisms how this interaction is fine-tuned remain unknown despite numerous studies (Jourdain et al., 2007; Panatier et al., 2011; Poskanzer and Molofsky, 2018; Volterra and Steinhäuser, 2004). A reason why the details remain elusive is the lack of specific tools to dissect distinct astrocyte-neuron pairs that are in direct contact to each other. In the presented study it was qualitatively tested whether the retrograde tracer molecule TTC coupled to the reporter protein eGFP can be used to identify distinct astrocyte-neuron ensembles. TTC could therefore serve as a tool to allow specific targeting of astrocyte-neuron ensembles. The eGFP-TTC protein was delivered via rAAV vectors allowing genetically targeted expression in neurons or astrocytes. Cell types of eGFP-positive cells were identified using immunohistochemical analysis.

2.1.1 EGFP-TTC expression in neurons does not result in eGFP-TTC signal in astrocytes

Perreault et al. have demonstrated that eGFP-TTC is transsynaptically transported from one neuron to another (Perreault et al., 2006). These studies focused on neurons and their connections to each other and a possible uptake of eGFP-TTC in astrocytes was not evaluated and has potentially been overlooked. In order to elucidate whether astrocytes are capable of eGFP-TTC uptake, it was transduced to neurons under the control of the neuron-specific synapsin promoter (figure 1A). The viral vector was injected unilaterally into the hippocampus of mice and the eGFP-positive cells were analysed three weeks later to determine cell types of eGFP-positive cells in both hemispheres. As expected, the injected hemisphere showed strong signal in the dorsal hippocampus close to the injection site (figure 1B, “IDG”, figure 1C.vi), but the signal was also located in the dentate gyrus (DG) of the ventral hippocampus (figure 1B, “iDG”) the entorhinal cortex (figure 1B, “iEC”) as well as the thalamus (figure 1B, “LD” and “LSr”). This indicates that the eGFP-TTC was transsynaptically transported to these regions, which are known to be connected to neurons in the hippocampus (Witter, 1993). Also, neurons in the contralateral CA region and DG of the hippocampus (both dorsal and ventral) as well as the ventral entorhinal cortex were eGFP-TTC positive (figure 1B,C, “cDG”, “cEC”). The contralateral

signal was weaker, compared to the signal in the ipsilateral hemisphere. The spread and pattern of the signal shows, that the eGFP-TTC is transported across synapses. Hippocampal neurons are known to project via the Schaffer collaterals to the hippocampus of the other hemisphere. Therefore, the eGFP-TTC can access these neurons by retrograde transport along synapses with primarily infected starter neurons in the rAAV-injected hippocampus.

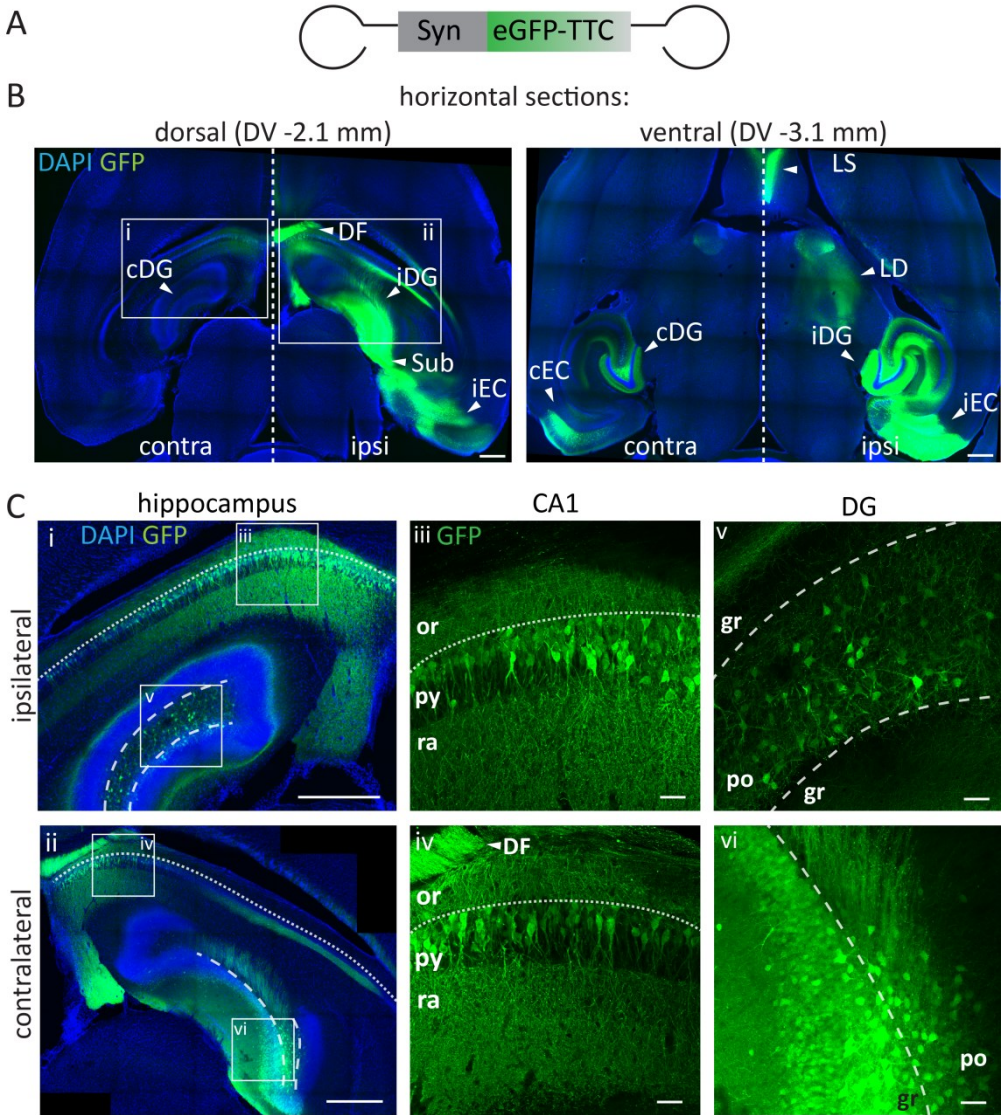

Figure 1: eGFP-TTC expressed in neurons is transmitted across synapses. *A) Schematic representation of injected rAAV construct. B) Representative horizontal dorsal and ventral sections from animals injected with rAAV-syn-eGFP-TTC. Slice coordinates on dorso-ventral axis (DV) indicated. The eGFP-TTC signal is observed in the dorsal hippocampus in both hemispheres. Even in the ventral hippocampus the eGFP-TTC signal was found in ipsi- and contralateral DG (iDG, cDG) as well as in the entorhinal cortex (iEC, cEC). Diffuse eGFP-TTC signal was observed in the lateral septal nucleus (LS) and lateral dorsal nucleus of thalamus (LD). Scale bars 500 µm. C) close-up images of indicated rectangles i-vi. In the CA1 pyramidal layer (py) neurons but no astrocytes were eGFP-TTC positive in both hemispheres. In the injected hemisphere the DG (iDG) was found to have many eGFP-TTC-positive neurons in the granular layer (gr) and the polymorph layer (po), while on the contralateral hemisphere only the polymorph layer eGFP-TTC-positive neurons were observed. Dorsal fornix fibers (DF) only in the injected hemisphere were observed. Neither region showed eGFP-TTC-positive astrocytes. Scale bars 50 µm. Or: stratum oriens py: pyramidal layer, ra: stratum radiatum.*

Notably, the dorsal fornix, the main output fibre bundle from the hippocampus, connecting the two hemispheres, was clearly eGFP-TTC positive in the injected hemisphere (figure 1B, “DF”,

figure 1C.iv). It has to be noted though, that direct infection of axon terminals is another possible access route to these neurons as rAAV1/2 serotype can infect axon terminals, albeit with low efficiency (Tervo et al., 2016). The observation of eGFP-TTC signal in the contralateral entorhinal cortex, however is a clear indication, that the eGFP-TTC must have crossed at least one or more synapses. High magnification imaging identified the eGFP-TTC-positive cells in both hemispheres to be neurons (figure 1C). It has to be noted that the location of eGFP-TTC positive neurons in the contralateral DG compared to the ipsilateral DG differ as shown in figure 1C.v and C.vi. While in the injected hemisphere eGFP-TTC neurons were located in the granular layer as well as in the polymorph layer of the DG, in the contralateral hemisphere the granular layer was void of eGFP-TTC-positive cells.

In both hemispheres no eGFP-positive astrocytes were observed. This suggests that the transport of the eGFP-TTC signal from one starter neuron to the next neuron, travelling comparably large distances to regions outside the injected hippocampus, occurs completely without any astrocyte involvement. This means that despite considering astrocytes to be active partners at the synapse, they are not involved in those aspects of synaptic transmission that the TTC fragment exploits for retrograde transsynaptic transport.

2.1.2 EGFP-TTC expression in astrocytes

Although eGFP-TTC protein expression in neurons does not result in eGFP-positive astrocytes, the question remains whether eGFP-TTC when expressed in astrocytes is transferred to other cells and if so, to which cell types. To investigate this, the eGFP-TTC construct was expressed under the control of the astrocyte-specific glial fibrillary acidic protein (GFAP) promoter (figure 2A). The immunofluorescence analysis of rAAV-GFAP-eGFP-TTC injections showed strong eGFP-TTC signals in astrocytes and comparably weaker signals in pyramidal neurons in the CA1 cell layer of the injected hippocampus (figure 2B, C). Moreover, there was diffuse eGFP-TTC signal in regions outside of the hippocampus in the retrosplenial cortex as well as the thalamus (figure 2B “LD”, “RSP”). Interestingly, there were eGFP-TTC-positive neurons in the pyramidal cell layer of the contralateral hemisphere (figure 2C) and the dorsal fornix of the ipsilateral hemisphere was eGFP-TTC positive (figure 2B, “DF”), similar to the previous observation with eGFP-TTC expression in neurons.

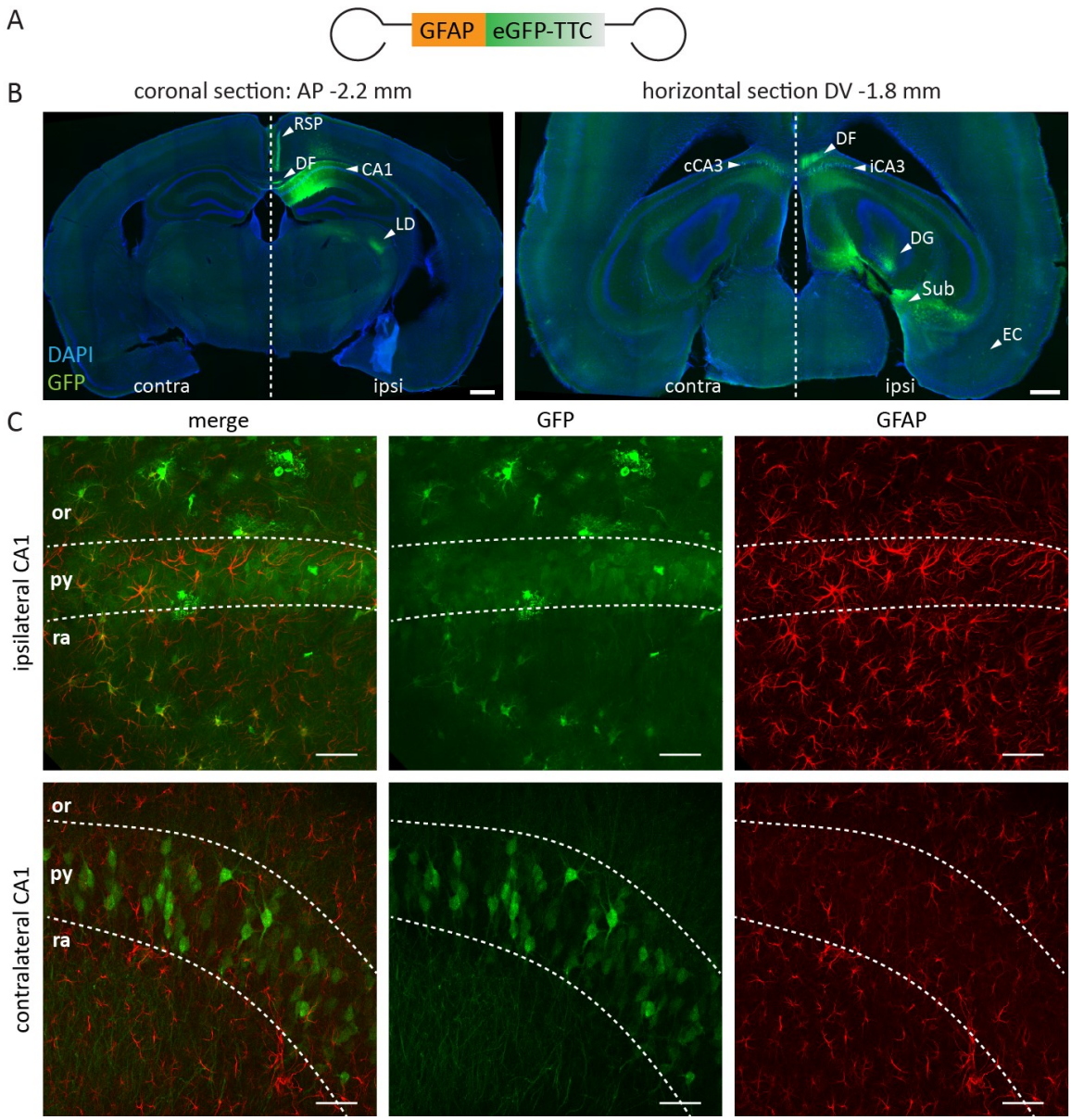

Figure 2: eGFP-TTC-expressed in astrocytes results in eGFP-TTC-positive neurons. *A) Schematic representation of rAAV construct. B) Representative coronal and horizontal sections from animals injected with rAAV-GFAP-eGFP-TTC. Slice coordinates on anterior-posterior (AP) and dorso-ventral (DV) axis indicated, respectively. The eGFP-TTC signal was observed in astrocytes and neurons the hippocampus of the injected hemisphere (CA1, iCA3, DG). eGFP-TTC-positive astrocytes were also observed in the ipsilateral cortex together with non-cellular eGFP-TTC-positive structures spreading along the retrosplenial cortex (RSP) and lateral dorsal nucleus of the thalamus (LD) and the entorhinal cortex (EC). eGFP-TTC-positive neurons but not astrocytes were observed in the hippocampus contralateral to the injection site (cCA3) and eGFP-TTC signal was observed in the dorsal fornix (DF), both indicating the presence of eGFP-positive neurons projecting to the contralateral hemisphere. Scale bars 500 µm. C) High magnification images of the ipsi- and contralateral hemisphere showed eGFP-TTC-positive CA1 pyramidal neurons and astrocytes in the ipsilateral hemisphere. In the contralateral hemisphere only eGFP-TTC-positive neurons were observed. Scale bar 50 µm. "Or": stratum oriens "py": pyramidal layer, "ra": stratum radiatum.*

Immunofluorescence labelling against the astrocyte specific GFAP protein as well as the morphology clearly identified neurons in the contralateral CA regions, indicating that eGFP-TTC was transported to these cells, by transsynaptic transport. In control experiments animals were injected with rAAV-expressing only the uncoupled eGFP reporter (rAAV-GFAP-eGFP, figure 3A).

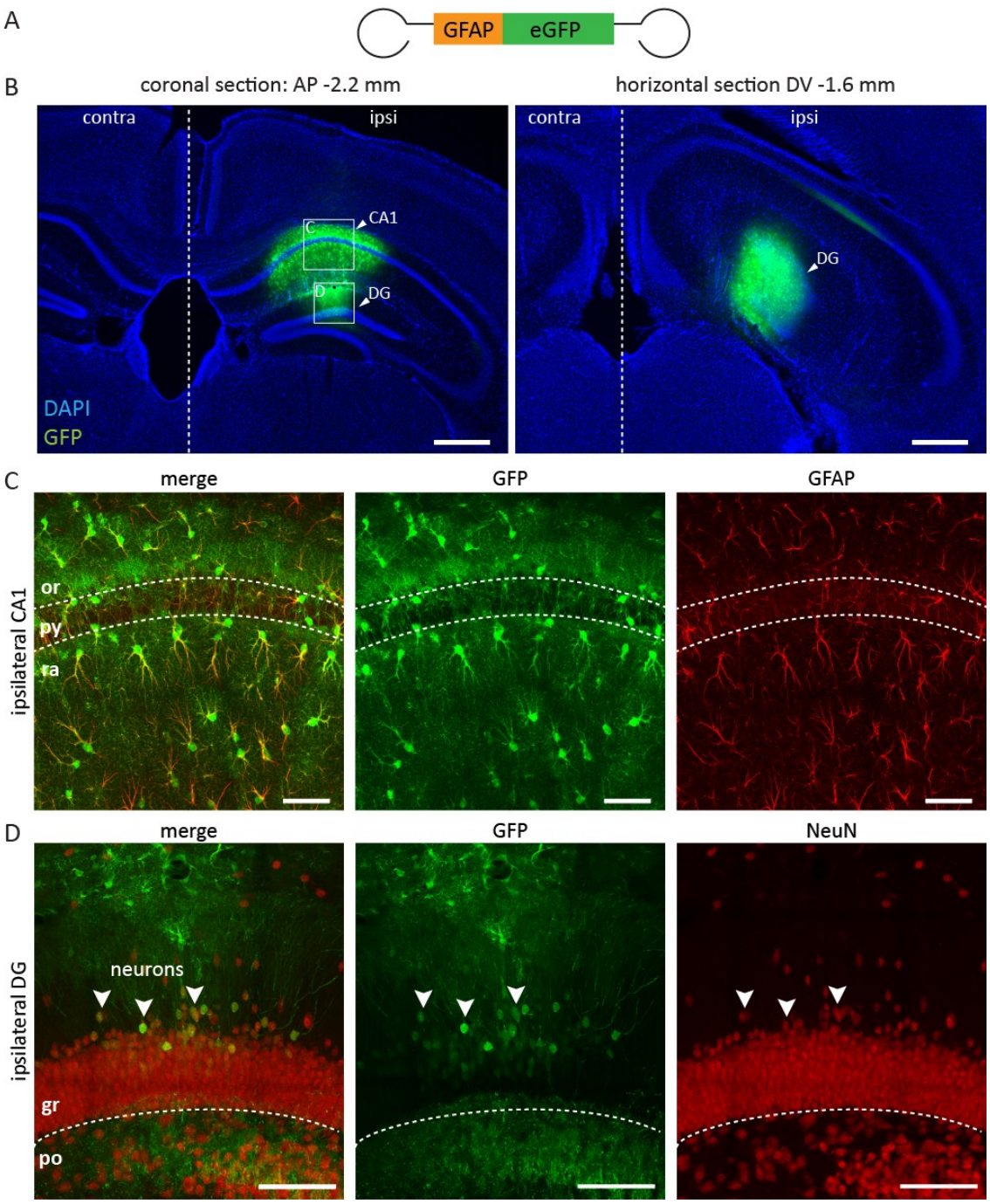

Figure 3: eGFP expression in astrocytes is restricted to the hippocampus but shows non-specific expression in DG neurons. *A) Schematic representation of rAAV construct. B) Representative coronal and horizontal sections from animals injected with rAAV-GFAP-eGFP. Slice coordinates on anterior-posterior (AP) and dorso-ventral (DV) axis indicated, respectively. The eGFP signal was observed in astrocytes only in the hippocampus (CA1, DG) of the injected hemisphere but not outside of the hippocampus or in the contralateral hemisphere. Scale bars 500 µm. C) High magnification images of the ipsilateral CA1 pyramidal cell layer (indicated by dotted line) showed that there were not eGFP-positive neurons. Scale bar 50 µm. Or: stratum oriens, py: pyramidal layer, ra: stratum radiatum. D) High magnification images of the ipsilateral granular cell layer of the DG (dotted line indicates border between polymorph layer (po) and granular layer(gr)) showed that some neurons express the eGFP protein (examples indicated with arrowheads). Scale bar 100 µm.*

In these brains the CA region of the injected hemisphere and the contralateral hemisphere are completely devoid of eGFP-positive signals as shown in figure 3B and C. Immunofluorescence labelling of GFAP, identified all eGFP-positive cells as astrocytes as shown in the high

magnification images in figure 3B. Another striking difference is the overall spread of the eGFP signal. In case of the rAAV-eGFP virus the signal is confined to the injection site in the hippocampus (figure 3 B), whereas the eGFP-TTC fluorescence besides the labelling of the contralateral neurons, is more spread out towards the subiculum of the injected hippocampus (figure 2B, "Sub"), which is connected to the CA1 region as well as the entorhinal cortex (Witter, 1993).

While on the first sight this observation could mean that eGFP-TTC expressed in astrocytes is not confined to starter cells (cells expressing the rAAV construct), a closer analysis of the granular cell layer of the DG gives another explanation. The granular layer of the DG in the control mouse showed eGFP positive cells, which were identified as neurons by immunofluorescence labelling for NeuN (figure 3D, arrowheads). This observation challenges the conjecture of the strictly astrocyte-specific expression of the constructs in this region. The eGFP-TTC-positive cells in brains injected with the rAAV-eGFP-TTC could therefore occur due to nonspecific expression in neurons in the DG. Since eGFP-TTC is known to cross synapses from one neuron to another (see figure 1 or Perreault et al., 2006), the signal may travel from the DG via interneurons to the other brain regions, which explains the wide distribution of eGFP-TTC-positive cells in different brain areas as observed when eGFP-TTC is expressed with the GFAP promotor (figure 2).

2.1.3 Specific eGFP-TTC expression in astrocytes of ALDH1/1-CreERT2 mice

In order to avoid non-specific expression of the eGFP-TTC fusion protein as observed in the previous experiments, the ALDH1/1-CreERT2 inducible transgenic mouse line was employed. This mouse line expresses the tamoxifen inducible cre-recombinase (CreERT2) exclusively in astrocytes (Srinivasan et al., 2016). A new rAAV vector was constructed where the eGFP-TTC gene is flanked by two cre-recombinase recognitions sites (loxP, lox2272) in a double-inverted orientation (rAAV-GFAP-eGFP-TTC-DIO) (figure 4A). The rAAV-GFAP-eGFP-TTC-DIO was injected in the hippocampus at the same coordinates as in the previous experiments (figure 4B). One week after injection the cre activity of CreERT2 was activated by tamoxifen administration and three weeks later brains were analysed.

As expected the immunohistological staining of brain sections showed a high number of eGFP-positive astrocytes but in cotrast to rAAV-GFAP-eGFP-TTC injected wild-type mice (figure 2) no neurons were EGFP-TTC positive(figure 4B). Immunofluorescence labelling of the GFAP protein showed that all eGFP-TTC positive cells are also GFAP positive (figure 4B, close-ups). There was no signal in the pyramidal cell layer of the CA-regions in neither hemisphere and

neuronal cell bodies are clearly omitted. It has to be noted, however that despite the absence of cre-recombinase in control

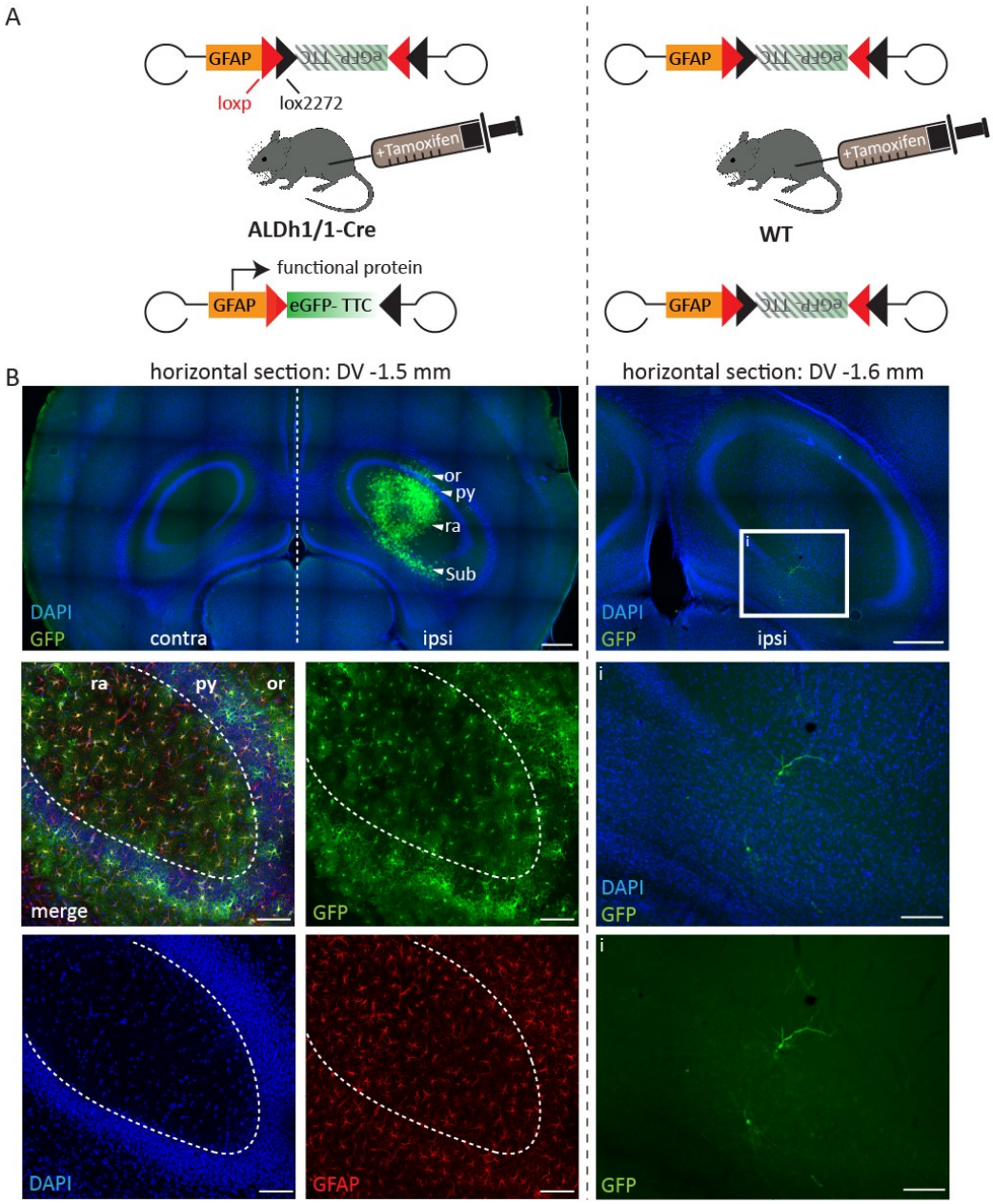

Figure 4: Only eGFP-TTC-positive astrocytes but not neurons were observed in rAAV-eGFP-TTC-DIO- injected brain of ALDH1/1-CreERT2 mouse. *A) Schematic representation of injected virus GFAP-eGFP-TTC-DIO induction. B) Top images show overviews of horizontal sections. Slice coordinates indicated on dorso-ventral (DV) axis. Scale bar 500 µm. While many eGFP-TTC-positive cells were observed in the CA region of ALDH1/1-cre mouse and very few eGFP-TTC positive cells in WT mouse. This indicates a low level of non-specific expression of the injected rAAV-eGFP-TTC-DIO. No eGFP-TTC signal was observed in the contralateral hemisphere. Co-localization with immunofluorescence signals for GFAP identifies only astrocytes in the ALDH1/1-cre to be positive for eGFP-TTC. Cell types of the non-specific eGFP-TTC expressing cells in WT animals could not be identified. Scale bar bottom two rows 100 µm. Or: stratum oriens, py: pyramidal layer, ra: stratum radiatum.*

experiments with the rAAV-eGFP-TTC-DIO in a WT mouse without cre-recombinase (figure 4B and C) showed two eGFP-TTC-positive cells, indicating a low level of non-specific expression. The cell type of these cells could not be determined, as these cells were not positive for any

established immunolabelling assay, nor matched the morphology of a certain cell type. Compared to the amount of signal observed in the tamoxifen induced ALDH1/1-Cre-ERT2 mouse the non-specific expression was very low and since there were no eGFP-TTC-positive neurons in the ALDH1/1-Cre-ERT2 mouse, this low-level non-specific expression of the eGFP-TTC-DIO construct does not result in false-positive neurons.

It can be concluded from these experiments that the eGFP-TTC does not jump from astrocytes to neurons. The previous results were most likely the effect of non-specific expression of the rAAV construct in granular cells of the DG.

2.1.4 Labelling starter cells with "2A-KusO"

The previous experiments have shown that eGFP-TTC expressed in astrocytes is not transmitted to neurons and *vice versa*, expression in neurons does not result in eGFP-TTC labelled astrocytes. However, eGFP-TTC expressed in astrocytes shows a remarkable spread of the signal in the ALDH1/1-Cre-ERT2 mice. The question remains whether all eGFP positive astrocytes express the construct or if some of them received it by intercellular transport mechanisms.

In order to distinguish rAAV-expressing starter cells, from those cells receiving the eGFP-TTC fusion protein, another construct was cloned including a second immobile reporter. This reporter is the kusabira orange (KusO) fluorophore which is concatenated to the eGFP-TTC construct with the transscriptional-skipping T2A-peptide sequence (Wang et al., 2015). Since the two proteins are separately translated by ribosomal skipping the eGFP-TTC is free for transport into another cell, while the KusO-reporter stays behind in the starter cell. This allows distinction of cells expressing the rAAV construct, positive for both eGFP and the KusO reporter, from cells receiving the eGFP-TTC fusion protein via transsynaptic transport, which are only eGFP positive. This approach not only allows identification of those astrocytes which receive the eGFP signal from neighbouring astrocytes (figure 5) but may also confirm the previously observed leak expression in neurons.

The eGFP-TTC-2A-KusO virus was injected in hippocampi of adult mice and brains were dissected and sliced 2 – 3 weeks after injection (figure 5). It was observed that similarly to the ALDH1/1-cre-ERT2 experiment, the eGFP-TTC signal was only observed in the injected hemisphere with a tendency to spread towards the subiculum (figure 5B, "Sub"). A number of clearly double-labelled astrocytes as well as neurons in close proximity to the injection site were observed (figure 5C arrowheads, asterisk). In contrast to the injections with rAAV-GFAP-eGFP-TTC (figure 2), the injection site appears damaged and surprisingly the KusO-reporter is located extracellularly and in the absence of eGFP signal (figure 5C, arrows). This suggests toxic effects of the KusO-reporter and that cells expressing the construct had died during the incubation period

which is a problem often observed with red-shifted fluorescent reporters (Shemiakina et al., 2012). While the double-labelled neurons (figure 5C, asterisk) indicate again that the construct is non-specifically expressed as seen with the rAAV-GFAP-eGFP-TTC (figure 3), the general tissue damage makes interpretation of these results difficult.

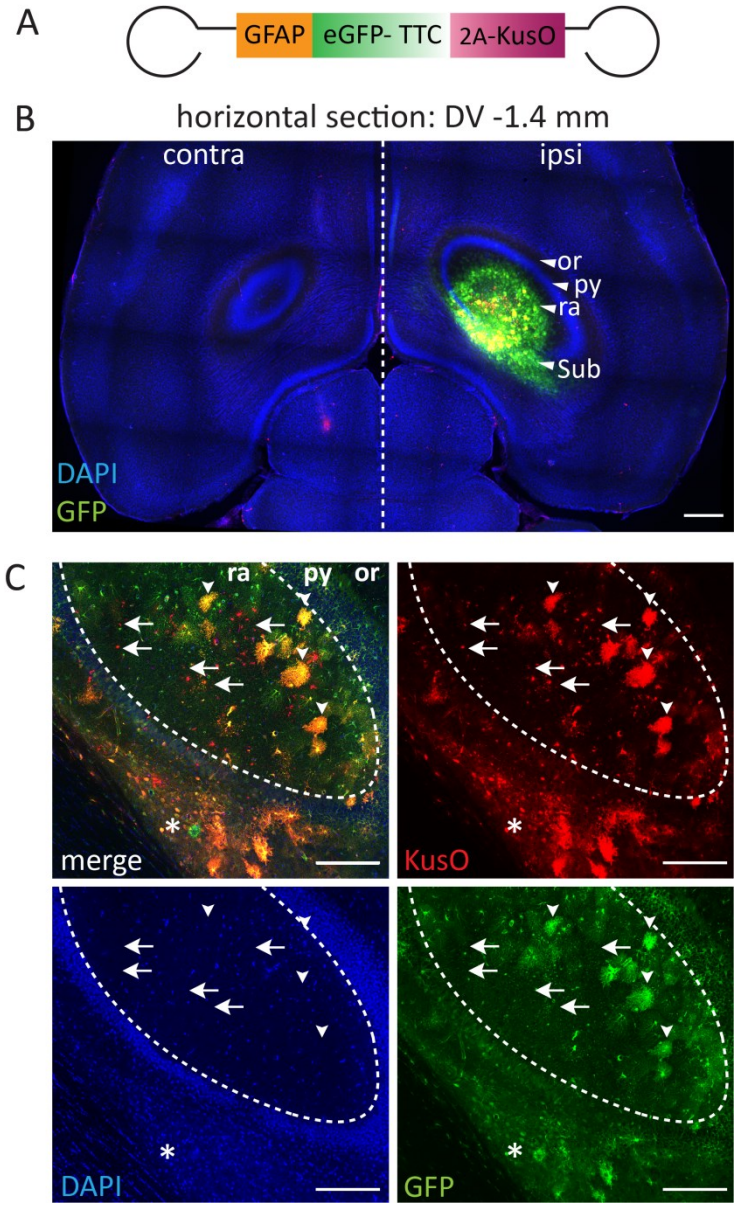

Figure 5: Fluorescence images of brain injected with rAAV-eGFP-TTC-2A-KusO. *A) Schematic representation of injected virus GFAP-eGFP-TTC-2A-KusO. B) Overview of horizontal section at coordinates on dorso-ventral (DV) axis as indicated. EGFP-TTC and 2A signal is located in the injected hemisphere close to the injection site and in the subiculum (Sub). Scale bar 500 µm. C) High magnification images of the injections site show beside double positive astrocytes (arrowheads) and double positive neurons (asterisk) extracellular red fluorescent particles (arrows), indicating cell death of KusO expressing cells. Scale bar 200 µm. Or: stratum oriens, py: pyramidal layer, ra: stratum radiatum.*

Extracellularly located fluorophore proteins could be picked up by surrounding cells and give rise to false positive cells. The same is true for the surrounding astrocytes making it impossible to distinct starter astrocytes and astrocytes which received eGFP-TTC by cell-to -cell contact. Almost all astrocytes in close proximity to the injection site were weakly labelled with the red-

fluorophore. On the one hand this could mean that only cells with low expression level survived the incubation time. On the other hand, as aforementioned endocytosis of fluorophore proteins from the extracellular space could also result in a weak labelling of these cells. It is however worth to mention that the eGFP-signal spreads much further along the subiculum compared to the KusO signal (figure 5B, "Sub"). Cells in these more distal areas are exclusively non-neuronal, suggesting that the eGFP-TTC signal spreads from starter cells, whichever they are, to these astrocytes. Nonetheless, the fluorophore-triggered cell death alters the cell physiology compared to previous injections and these results do not reflect the undisturbed *in vivo* situation. Therefore, this construct does not allow the clear distinction between starter cells and target cells.

2.1.5 Combined fluorescence *in situ* hybridisation-immunofluorescence

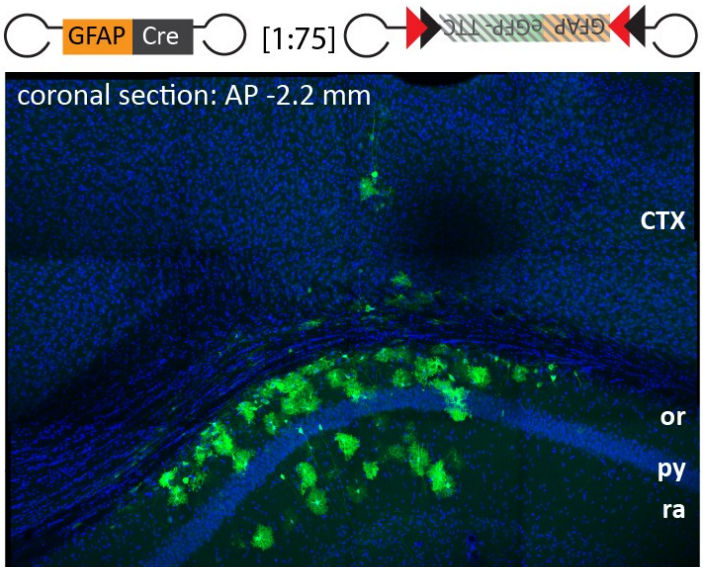

Figure 6: 75:1 ratio of rAAV-GFAP-eGFP-TTC-DIO and rAAV-GFAP-Cre-recombinase results in sparse but intense eGFP-TTC expression. *Representative coronal section (slice coordinates on anterior-posterior (AP) axis as indicated) with EGFP-positive cells, sparsely distributed in the injected hippocampus. CTX: cortex, or: stratum oriens, py: pyramidal layer, ra: stratum radiatum. Scale bar 200 µm*

Since distinction of rAAV-expressing cells and potential eGFP-TTC-targeted cells proved to be difficult another approach was applied. To solve the question whether transport of eGFP-TTC from astrocytes to other cells takes place, a combination of eGFP immunofluorescence labelling and fluorescent labelling of the eGFP mRNA by *in situ* hybridization (FISH-IF) was established using the RNAscope® FISH assay. In contrast to tracer studies dissecting strictly neuronal connections, the target cells of astrocytes are potentially in close proximity to the starter astrocyte cell. In the previous experiments the injection site showed a great number of eGFP positive cells, making identification of single cells even with confocal microscopy difficult. To allow better read-out of the combined FISH-IF assay a sparse expression of the eGFP-TTC is desirable. Therefore, a modified eGFP-TTC expression system was used for the FISH-IF assay. This system is a combination of the cre-dependent rAAV-eGFP-TTC-DIO (see results 2.3.1) and another much more diluted rAAV expressing cre-recombinase (rAAV-GFAP-CRE) (figure 6A). The ratio of the two viral titres was experimentally

tested and matched to allow expression of eGFP-TTC in only very few cells. Since the rAAV-eGFP-TTC-DIO is not diluted, these the rAAV-eGFP-TTC-DIO cells have a high copy number of eGFP-TTC-DIO and are expected to have high eGFP-TTC expression when activated by Cre. Cre-recombinase was delivered via rAAV expression under control of the GFAP promotor, therefore an additional level of expression control is added to the system as well. Different ratios of the cre-expressing and the cre-dependent virus were tested (1:25, 1:75, 1:100, 1:400) and a ratio of 1 part cre-expressing virus to 75 parts cre-dependent virus resulted in a sparse but intense labelling of cells as shown in figure 6B. For the following FISH-IF experiments the two viruses were used with this ratio.

The FISH-IF assay was performed according to the manufacturer's instruction with modified incubation steps as described in material and methods (chapter 4.3.2), using the eGFP probe. Since rAAVs infect cells in an unspecific manner the viral DNA is abundant in all cells in the injection site. Therefore, a DNase step was included before the FISH assay was performed. Additionally, an eGFP-sense probe was used as negative control. The sense probe is identical to the mRNA and can therefore only detect eGFP-encoding DNA. Any signal obtained with the sense probe is therefore false positive DNA detection and these experiments served to estimate the background FISH signal from DNA-contamination. As shown in figure 7B the RNAscope® signal with the RNA-detecting eGFP-probe was observed in the CA1 region of the injected hippocampus. The eGFP antisense probe was co-localized with cell bodies positive for eGFP immunofluorescence signal (figure 7B, arrowheads). However, essentially all cells in the pyramidal cell layer were positive for the FISH-eGFP signal while showing no immunofluorescence signal, indicating false positive detection with the RNAscope® assay. Indeed, the negative control with the eGFP-sense probe showed similarly strong signal in the CA1 region, providing strong evidence that the RNAscope® assay was not restricted to RNA detection but also detects the high copy numbers of eGFP-encoding rAAV genomes that were delivered to astrocytes and neurons (figure 7C). This is surprising since the DNase treatment should have avoided this false positive detection. This means that it is not possible to distinguish FISH-eGFP-positive cells containing mRNA from those giving a false positive signal due to high rAAV genome load. Therefore, the combined FISH-IF approach could not clarify which cells express the viral DNA and which receive eGFP signal transsynaptically.

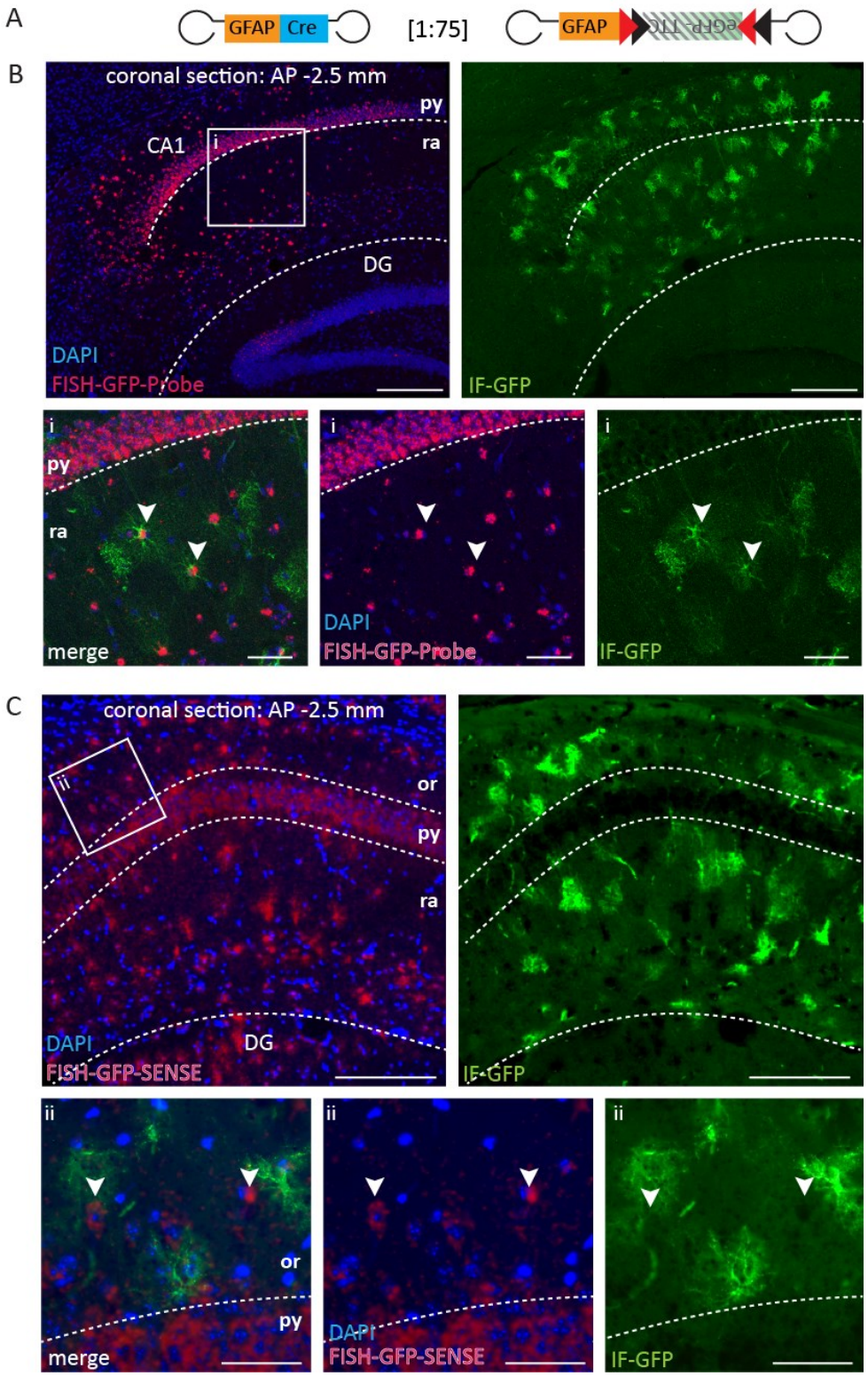

Figure 7: Combined FISH-eGFP signal and IF-GFP signal does not co-localize. *A) Schematic representation of injected virus rAAV-GFAP-Cre and rAAV-GFAP-eGFP-TTC-DIO in a 75:1 ratio. B) All cells within the injected area had FISH –signal with the antisense eGFP probe (B). While all IF-positive cells co-localize with FISH-signal (B arrowheads in close-up), FISH signal is observed also in cells with no IF signal e.g. in the pyramidal cell layer, indicating false positive FISH detection (B, "py"). Control experiments with the DNA detecting sense probe (C) confirm strong false positive background from DNA signal contamination (C arrowheads in close-up). Scale bars B,C top: 200 µm, close-ups 50 µm. Or: stratum oriens, py: pyramidal layer, ra: stratum radiatum. Slice coordinates indicated on anterior-posterior (AP) axis.*

2.2 $[Ca^{2+}]_i$ signals during gamma oscillations

Gamma oscillations are concerted neuronal activity patterns, which can be measured in *in vivo* as well as *in vitro*. While the exact mechanisms of their generation are is still not resolved, it has been shown, that hippocampal gamma oscillations play an important role in memory and learning processes (Buzsaki and Draguhn, 2004). Since astrocytes are regarded as an active partner in synaptic transmission, and are linked to brain state switches, the possibility of a direct correlation of the astrocytic $[Ca^{2+}]_i$ transients and gamma oscillations was investigated. While Lee et al already showed on a single cell level that astrocytic $[Ca^{2+}]_i$ transients precede the occurrence of gamma oscillations (Lee et al., 2014), I investigated in hippocampal slice cultures how the whole astrocyte population behaves during CCH-induced gamma oscillation (CCH-GM). Moreover, I investigated whether astrocyte $[Ca^{2+}]_i$ transients correlate with neuronal $[Ca^{2+}]_i$ transients. To achieve this, the virus encoded Ca^{2+} indicators GCaMP6f and jRGeco1a were delivered to astrocytes and neurons, respectively, in hippocampal organotypic cultures by co-infection with rAAV-GFAP-GCaMP6f and rAAV-Syn-jRGeco1a (figure 8A). After 14-21 days the astrocytic $[Ca^{2+}]_i$ and neuronal $[Ca^{2+}]_i$ activity was monitored while measuring the local field potential (LFP) during CCH-GM (figure 8,B).

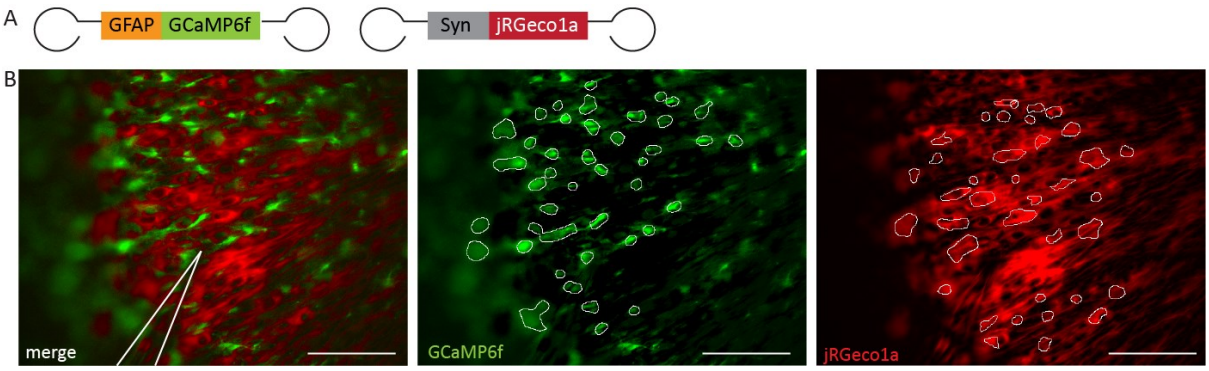

Figure 8: Parallel recording of $[Ca^{2+}]_i$ transients in astrocytes and neurons. *A) Schematic representation of rAAV-GFAP-GCaMP6f and rAAV-Syn-jRGeco1a used for cell specific expression of the colour shifted Ca^{2+} indicators. B) Maximum intensity projection of both imaging channels from a representative recording with the detected ROIs indicated (white outlines) shows the two non-overlapping cell populations. Position of the field electrode is indicated in merge image. Scale bar: 50 µm.*

Recordings were performed in a submerged imaging chamber for 6.5 minutes during which CCH was washed into the chamber for gamma oscillation induction and was continued to be washed in until the end of the recording. Figure 9 illustrates schematically the simultaneous measurements and the wash in of CCH. The field electrode was placed in the CA3 region of the slices as gamma oscillations are thought to be generated in this region (figure 8B). In order to analyse the Ca^{2+} signals of both astrocytes and neurons, the Ca^{2+} imaging data were pre-processed with MATLAB using the customized constrained non-negative matrix factorization method (CNMF) described by Pnevmatikakis et al., 2016. The processing step defines ROIs and

extracts their respective relative fluorescence over time. This method also includes image normalization and demixing of signals from overlapping ROIs. Spatial segmentation results are shown for the example in figure 8B with white outlines around the respective ROIS.

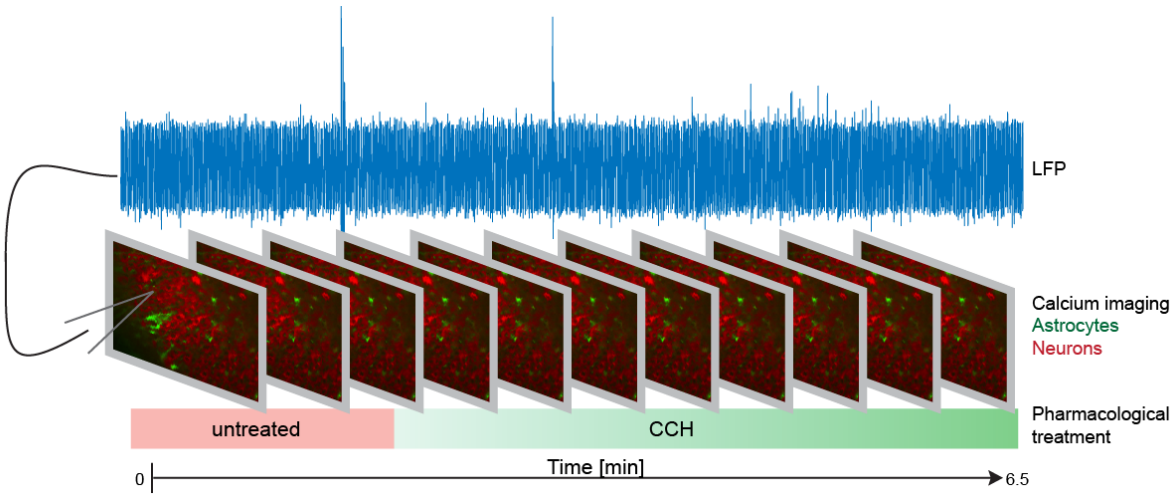

Figure 9: Experimental set up. *Local field potential (depicted as blue trace on top) is recorded simultaneously with Ca^{2+} transients from astrocytes and neurons. At the beginning of the 6.5 minute experimental session the slice is untreated. After approximately 1 minute CCH is washed in.*

ROIs are mostly round regions with different diameters between approximately 2-15 µm for astrocytic ROIs and 2 – 30 µm for neuronal ROIs. Based on size and morphology one can conclude that the astrocytic ROIs are mostly microdomains of astrocyte processes, which is in line with accounts of astrocytic $[Ca^{2+}]_i$ transients in the literature (Tang et al., 2015). In case of the neuronal ROIs, sizes and shapes vary greatly and judging from morphological features, some ROIs appear not plausible as there are no neuronal cell bodies but only neuropil present. Therefore, an additional manual validation step was included in the image processing to exclude ROIs which are clearly not of somatic origin. Another observation is that due to the lack of Ca^{2+} indicator in the neuron's nuclei, the segmentation in some cases detects only half the neuronal cell body. While this should not affect the $[Ca^{2+}]_i$ read out, ROI sizes were not evaluated, since splitting of ROIs renders the read-out unreliable.

2.2.1 Astrocytic and neuronal population stability differs over two recordings

Depending on the experiment type and the state of the respective slice, some slices were imaged twice for 6.5 minutes. The ROI extraction was performed for each recording independently regardless of whether or not the slice had been recorded twice in a row. Thus, it

was possible to compare the ROI detection results for those slices that have been recorded twice. It was determined, whether the same astrocytic ROIs and neuronal ROIs that are active in the first recording, are also active in the following imaging interval, or whether the population of active ROIs differs.

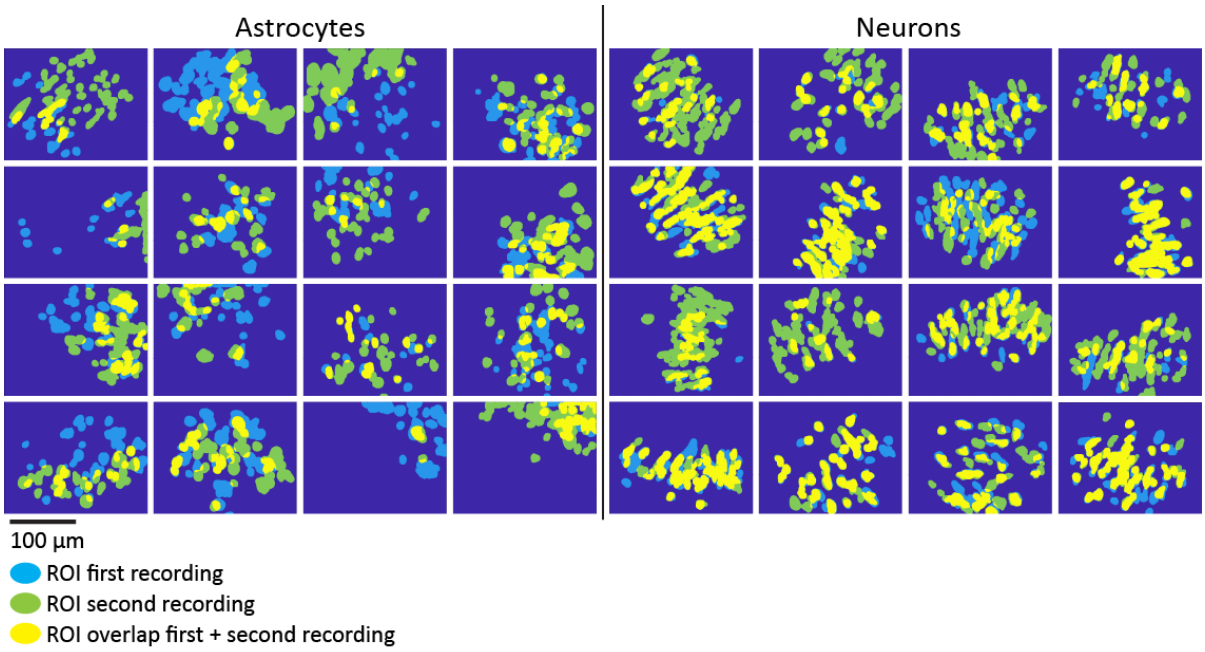

Figure 11: Overlaps of detected astrocytic and neuronal ROIs of 16 slices recorded twice consecutively. *Astrocytic ROIs were found to vary more over the course of two recordings whereas neuronal ROIs are more stable and are mostly detected in similar locations in both recordings.*

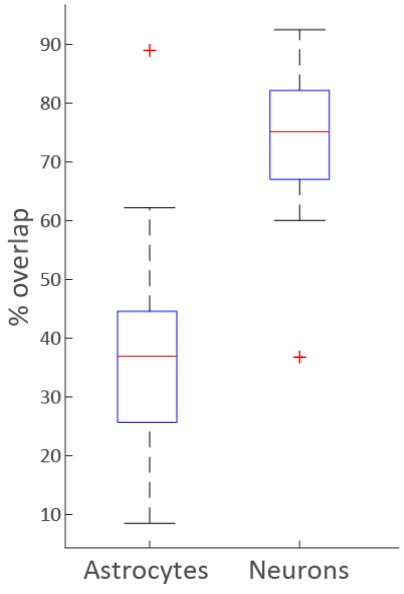

Figure 10: Astrocytic ROIs of two subsequent imaging sessions were less overlapping than neuronal ROIs. *Red line depicts the median overlap, blue box is the 25th and the 75th percentile, whiskers depict most extreme values, not considered outliers. Outliers labelled as red cross.*

While the overlap of astrocytic ROIs was comparably low, the neuronal ROIs appeared much more stable as shown in the 16 pictographs (figure 11) indicating the ROIs position in the fields of view in the first imaging session (blue), the second (green) and their overlap (yellow). The median overlap of the neuronal ROIs between first and second recording from 16 pairs of experiments was 75.14% (+- 13%) while the astrocytic ROIs only had a median overlap of 36.9% (+- 19%)(figure 10). The observation that most neuronal ROIs were detected in two independent measurements and processing rounds, means that the population of active neurons is stable, and cycles of activity are shorter than the recording time. The population of active astrocytic ROIs is much more inconsistent in the first and second recording. This could mean that the cycle for

recurrent activity of one particular ROI is longer than the imaging period, or that ROIs which are active at some point cease their activity altogether, while new ROIs become active. It must also be taken into consideration, that the two recordings were completed under different conditions, with different pharmacological agents. Nonetheless, this finding indicates that in contrast to the neuronal population the astrocyte population is more instable and reacts differently to the applied conditions.

2.2.2 Changes in $[Ca^{2+}]_i$ activity over time in astrocytes and neurons

Besides the spatial distribution the temporal distribution of astrocytic $[Ca^{2+}]_i$ signals in respect to CCH-GM was analysed. To this end, the astrocytic as well as the neuronal $[Ca^{2+}]_i$ signals of each ROI over time were analysed.Figure 12A and B top panels show the colour coded relative fluorescence intensity over time of each ROI depicted in figure 8B for astrocytic and neuronal ROIs, respectively. Peaks in the relative intensity were extracted for each ROI with a custom-made MATLAB script and pooled in a binarized "spike-matrix" (figure 12A, B lower panel).

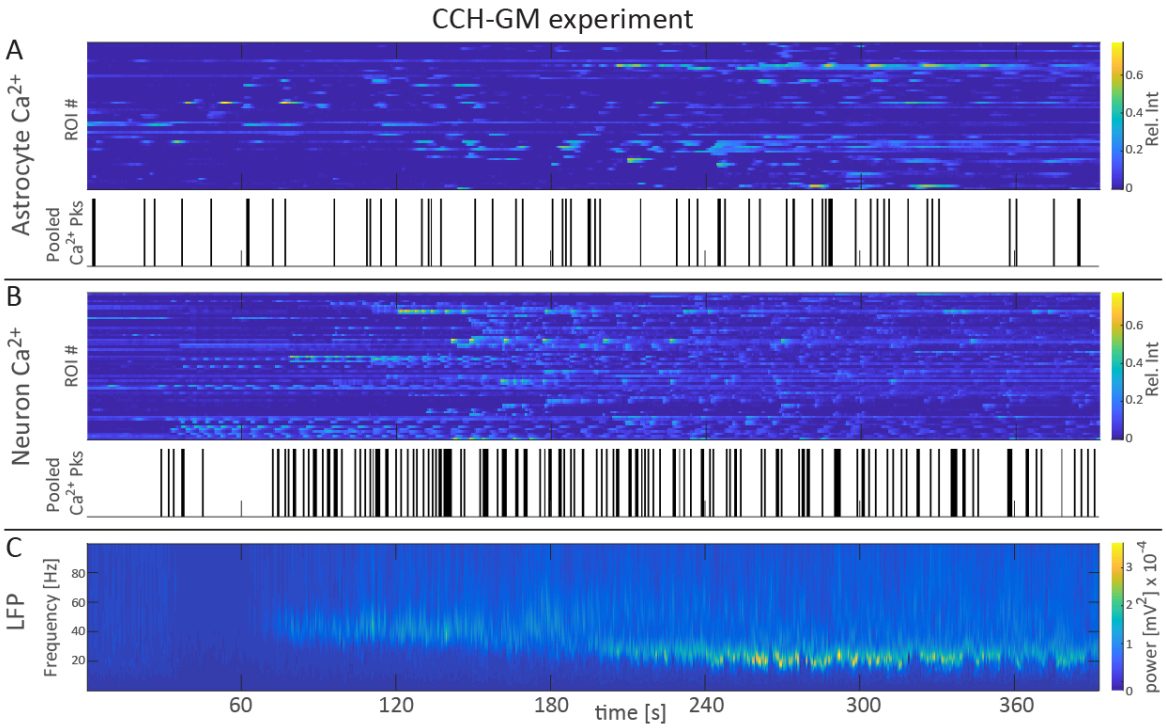

Figure 12: Relative intensity over time and LFP during CCH-GM. *A and B show the relative intensity over time for astrocytic ROIs (A) and neuronal ROIs (B) Top panel: each row represents a single ROI. Lower panel indicate where peaks are detected in the relative intensity over time pooled for all ROIs, respectively. C) Power spectrum density of the LFP with a clear 30 Hz band between 200 and 360 s occurring after CCH application.A total of 11 experiments were performed with this condition.*

The LFP recordings were low pass filtered and the power spectrum density was calculated, which is shown for this example infigure 12C. In this representative experiment the first 30 s were the pre-treatment time window. At 30 s CCH was washed in. The acute wash in phase first resulted in a state with no prominent oscillatory pattern, visible in the power spectrum with low values

between 30s and 60s. Usually a large number of astrocytes and neurons reacted with a brief increase in $[Ca^{2+}]_i$ activity in this phase. The development of gamma oscillations was observed at approximately 60 s where the 40 Hz frequency band showed a higher power density. This shifts towards 30 Hz through the course of the recording and becomes strongest between 200 and 360s. For the further analysis time windows were defined according to the oscillatory states of the respective slice. The time windows with no treatment were defined as “pre-treatment”. In this group two experiments with no pharmacological treatment throughout the recording were included. For analysis of CCH-GM only those time windows with stable 30 Hz gamma oscillations were used, as is the case between 200 – 360s in this example, while the acute wash-in phase was not included in the analysis. For each experimental condition the total number of peaks per time was normalized to the number of ROIs (further referred to as pks/s).

Astrocytes are known to express a number of neurotransmitter receptors which in turn can trigger Ca^{2+} transients, which means that the wash in of CCH itself can result in $[Ca^{2+}]_i$ transients (Shelton and Mccarthy, 2000). In order to discriminate the direct effects of CCH on astrocytes, in control experiments TTX, a blocker of voltage gated sodium channels (Lee and Ruben, 2008), was washed in before the CCH was applied (further referred to as TTX condition).

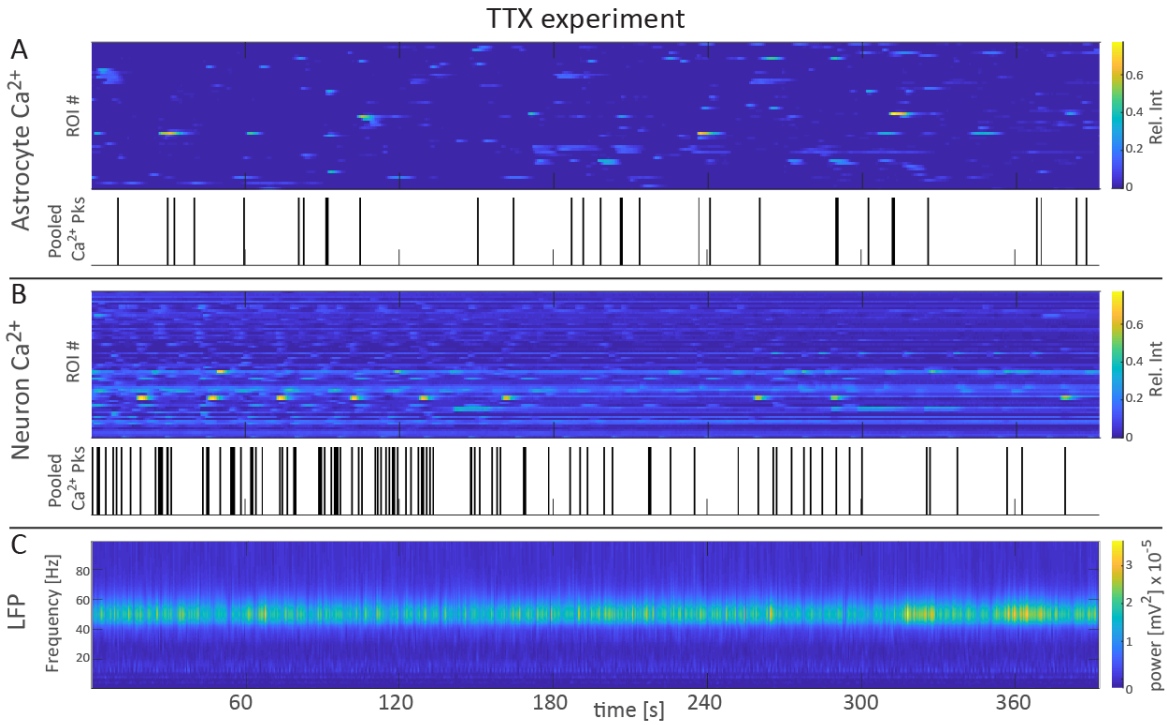

Figure 13: Relative intensity over time and LFP during TTX. *A and B show the relative intensity over time for astrocytic ROIs (A) and neuronal ROIs (B) Top panel: each row represents a single ROI. Lower panel indicate where peaks are detected in the relative intensity over time pooled for all ROIs, respectively. C) Power spectrum density of the LFP has only a band at 50 Hz with comparably weak power, indicating that only 50 Hz noise oscillations were present. A total of 4 experiments were performed with this condition.*

Thus, neuronal signal transduction and the development of gamma oscillations is supressed. The relative fluorescence of astrocytes and neurons as well as the power spectrum density of the LFP were analysed for TTX experiments similarly as the CCH-GM experiments. A representative TTX experiment is shown in figure 13. As expected the power spectrum density of the LFP did not show a prominent oscillatory pattern except for the comparably weak 50 Hz band that occurs due to noise in the recording.

Moreover, as another control experiment the $GABA_AR$ antagonist gabazine (GBZ) was used. GBZ is known to trigger epileptiform activity in organotypic slices by disinhibiting the slice (Glykys and Mody, 2007). In this model for synchronized neuronal activity, neurons fire together in a highly synchronized burst like manner. This was measured similarly to the CCH-GM and TTX experiments. The relative fluorescence of the neuronal ROIs was observed to coincide with the epileptiform activity bursts in the LFP measurement (figure 14).

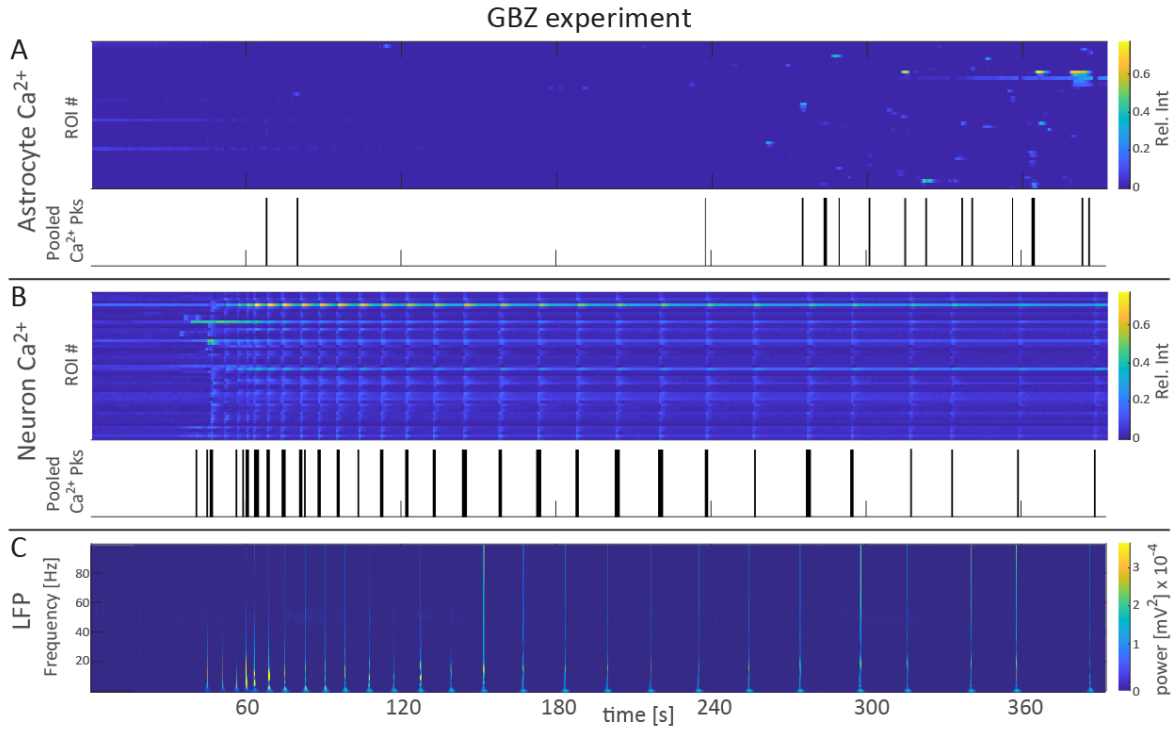

Figure 14: Relative intensity over time and LFP during GBZ. *A and B show the relative intensity over time for astrocytic ROIs (A) and neuronal ROIs (B) Top panel: each row represents a single ROI. Lower panel indicate where peaks are detected in the relative intensity over time pooled for all ROIs, respectively. C) Power spectrum density of the LFP shows recurring synchronous events upon GBZ wash-in which are synchronized with the neuronal peaks in the relative intensity. A total of 3 experiments were performed with this condition.*

For all four conditions; pre-treatment, CCH-GM, TTX and GBZ, the mean number of $[Ca^{2+}]_i$ pks/s was calculated for astrocytic and neuronal ROIs, respectively (figure 15). The number of $[Ca^{2+}]_i$ pks/s of astrocytic ROIs during the pre-treatment ($0.21 \pm 0.11 \times 10^{-3}$ pks/s) did not significantly differ from the number of $[Ca^{2+}]_i$ pks/s during CCH-GM ($0.63 \pm 0.18 \times 10^{-3}$ pks/s).

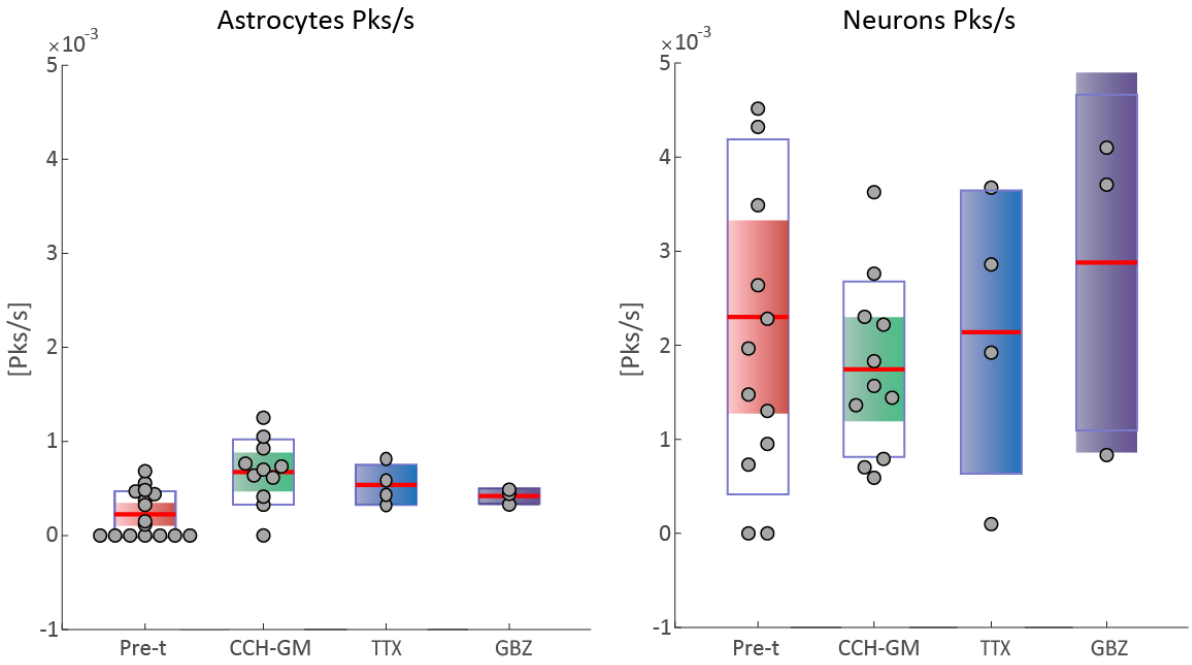

Figure 15: Number of peaks in the relative fluorescence intensity per time and per ROI of astrocytes and neurons does not differ in all four conditions. *Boxplots overlaid with data points from each experiment.(Red line depicts the mean, coloured box is the 1.96 SEM, blue frame is the 1xSD) shows no significant differences in the number of pks/s in the pre-treatment (Pre-, n=20), during CCH-induced gamma oscillation (CCH-GM, n = 11 slices), TTX (n = 4 slices) and GBZ (n = 3 slices).*

However, there was a trend of increased astrocytic activity (figure 15). In the TTX experiments, there was no significant change in the overall number of astrocytic pks/s compared to the pre-treatment time windows, but a trend towards a slight increase in the activity (0.54 ± 0.21 x10^{-3} pks/s) was observed, similar to the CCH-GM condition. This means that the trend observed in CCH-GM experiments can be explained by direct stimulation of AChRs on astrocytes and that it is not the gamma oscillation itself resulting in the increase trend of $[Ca^{2+}]_i$ pks/s seen in CCH-GM. In the gabazine condition again, the number of astrocytic $[Ca^{2+}]_i$ pks/s (0.42 ± 0.09 x10^{-3} pks/s) was not significantly in- or decreased compared to the pre-treatment.

The same analysis was done for the neuronal Ca^{2+} signals. In contrast to the astrocytic $[Ca^{2+}]_i$ signals, the number of neuronal $[Ca^{2+}]_i$ pks/s had a larger variance in all four conditions (figure 15): Pre-treatment (2.24 ± 1.10 x10^{-3} pks/s), CCH-GM (1.71 ± 0.63 x10^{-3} pks/s) , TTX (2.14 ± 1.54 x10^{-3} pks/s) and GBZ (2.88 ± 1.78 x10^{-3} pks/s) ranging from 0 - 4.8 pks/s x10^{-3}. Because of this large variance there was no significant difference in the mean number of $[Ca^{2+}]_i$ pks/s in the pre-treatment time window compared to the CCH-GM condition or the other two conditions. This is unexpected since the acute wash-in of CCH, as aforementioned increases the $[Ca^{2+}]_i$ activity in neurons. This effect however, was not found to last throughout the continued CCH wash-in and the onset of gamma oscillations, which was the time window that was included in this analysis. Likewise, it is surprising that the application of TTX did not significantly decrease

the neuronal $[Ca^{2+}]_i$ activity. It has to be noted however, that the number of experiments with TTX and GBZ were lower (n = 4 and n = 3, respectively) compared to the number of CCH-GM experiments (n = 11), which has to be taken into consideration.

As the variance of the peak frequency especially in the neuronal $[Ca^{2+}]_i$ peaks is rather large, the question arises whether the baseline $[Ca^{2+}]_i$ activity in different experiments varies as well. Therefore, the difference in the number of pks/s before and after each treatment for each slice was analysed and is shown in figure 16. In all three conditions the treatment resulted in an increase in the number of astrocytic $[Ca^{2+}]_i$ pks/s (figure 16 CCH-GM, TTX, GBZ). The same is true for the neuronal activity in TTX and GBZ treated slices, but not for the CCH-GM condition (figure 16, CCH-GM).

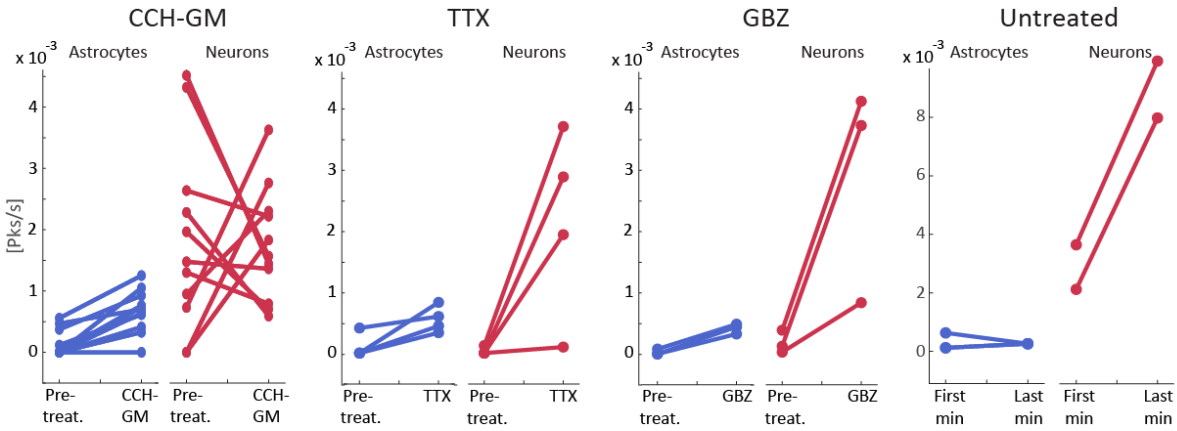

Figure 16: Changes in the number of $[Ca^{2+}]_i$ peaks over time and ROI before and after treatment for each slice. *For each pharmacological manipulation the number of peaks before the manipulation (Pre-treat.) and during the respective manipulation is shown for astrocytes (blue) and neurons (red). In the "Untreated" panel the first and the last minute of recordings without treatment are compared to each other.*

In 4 out of 11 experiments the number of $[Ca^{2+}]_i$ pks/s increased during CCH-GM compared to the pre-treatment window, while in 7 experiments the number decreased. This is an interesting finding, since the CCH-GM seems to have no uniform effect on neuronal $[Ca^{2+}]_i$ pks/s in different slices in contrast to the astrocytic $[Ca^{2+}]_i$ which show remarkable uniformity in all conditions. It has to be noted though, that in those 7 experiments with decreased number of neuronal $[Ca^{2+}]_i$ pks/s the activity was already much higher in the pre-treatment window compared to the activity pre-treatment with TTX and GBZ. This indicates that other methodological factors may account for variability in the number of neuronal $[Ca^{2+}]_i$ pks/s.

Since astrocytic $[Ca^{2+}]_i$ pks/s increased very similarly in all four conditions, potentially the time the slices are in the imaging chamber itself could be the reason for this increase. In order to control for this, the $[Ca^{2+}]_i$ pks/s of the first and the last minute of experiments with no treatment throughout the recording were compared. Results do not allow a clear conclusion since only two recordings without treatment were done. The number of astrocytic $[Ca^{2+}]_i$ pks/s increased when comparing the first to the last minute of recording in one case, while in the

second case the number decreased. The range of these in- and decreasing numbers is similar to the range seen in all the treated conditions. In case of the neuronal $[Ca^{2+}]_i$ pks/s in both untreated experiments the number increased and notably even the number of $[Ca^{2+}]_i$ pks/s in the first minute was higher compared to the number of $[Ca^{2+}]_i$ pks/s in all three treated conditions. Therefore, it can be concluded that the trends observed in the treated experiments are well within the range of the activity in the untreated conditions and are most likely not an effect of the pharmacological manipulations but are due to experimental variability.

2.2.3 Changes in $[Ca^{2+}]_i$ kinetics in astrocytes and neurons

Even though the overall frequency of $[Ca^{2+}]_i$ transients did not differ significantly, it is possible that $[Ca^{2+}]_i$ kinetics in astrocytes or neurons are changed during oscillations. Therefore the $[Ca^{2+}]_i$ peak kinetics were analysed for the same conditions; pre-treatment, CCH-GM, TTX and GBZ. The slope ratio for each $[Ca^{2+}]_i$ peak was calculated by dividing the absolute slope of the down stroke by the slope of the up stroke. Thus, a slope ratio close to 1 describes a symmetric peak, whereas values larger 1 indicate a slower decay time. Figure 17 shows a boxplot of all astrocyte and neuron slope ratios for the four conditions. The median value for astrocytes in the pre-treatment condition was 1.9 and was almost the same as the CCH-GM condition (1.8), indicating in both cases that the rise of the $[Ca^{2+}]_i$ signal was twice as fast as the decay and that this was independent from the CCH or CCH-GM treatment of the organotypic slice. The neuronal slope

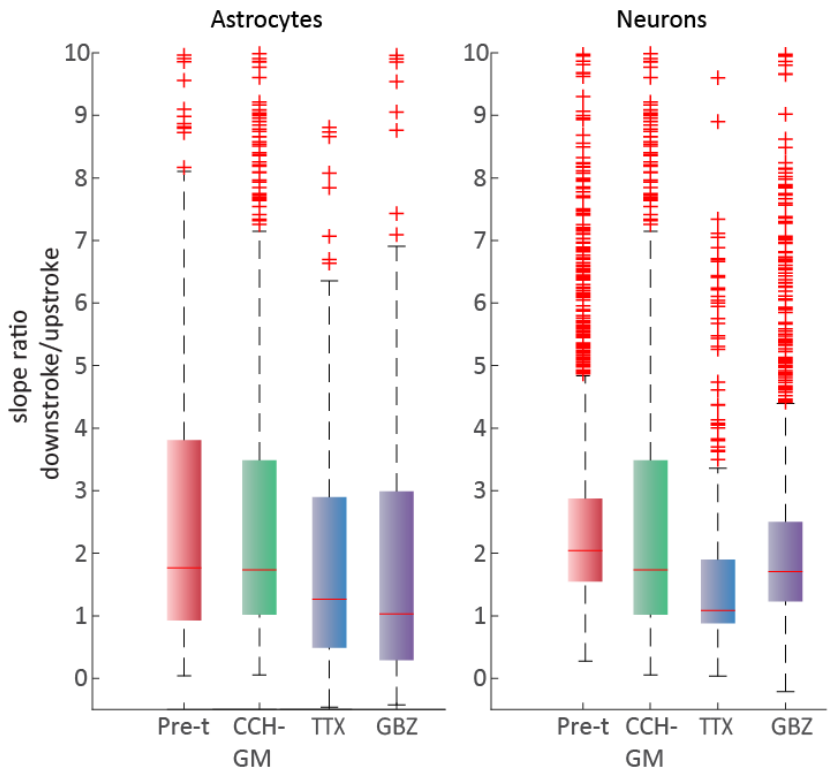

Figure 17: $[Ca^{2+}]_i$ peaks shapes do not change during CCH-GM. *Ratios were calculated by dividing the absolute value of the down stroke by the absolute value of the upstroke. Neither in astrocytic ROIs nor in neuronal ROIs the peak shape changed significantly in the four conditions: pre-treatment (Pre-t), CCH-GM, TTX and GBZ. Red line depicts the mean, coloured box is the 25th and the 75th percentile, whiskers depict most extreme values, not considered outliers. Outliers labelled as red cross.*

ratios were quite similar to the astrocyte slope ratios with median values close to 2. Thus neither CCH nor CCH-GM had an impact on the $[Ca^{2+}]_i$ kinetics in the astrocytes an neurons. Interestingly, both the astrocyte and the neuron slope ratio in the TTX experiments showed a trend towards a more symmetric peak shape (1.3 and 1.1, respectively) as well as in the astrocyte peaks in the GBZ condition. In all conditions the variance was very high and many peaks' slope ratios are outliers resulting in large standard deviations (figure 17), which does not allow a clear conclusion from the peak analysis. Therefore it can be concluded, that the activity of the astrocyte population cannot be used as an indicator for different neuronal oscillatory states.

2.2.4 Cross correlation of astrocytic and neuronal $[Ca^{2+}]_i$ signals

During gamma oscillations a single neuron was shown to participate in only about 5% of the cycles (Bartos et al., 2007). How neurons coordinate their participation in a cycle is not understood. Since the overall astrocytic $[Ca^{2+}]_i$ activity does not globally increase or decrease during CCH-GM as shown above, the astrocytic $[Ca^{2+}]_i$ transients potentially correlate temporally to the activity of single neurons on a local level, triggering or hampering selectively a neurons participation in the gamma oscillation. Therefore, the $[Ca^{2+}]_i$ activity of both cell types was compared to each other in order to find patterns in the correlation between astrocytes and neurons. One measure of similarity of two time series is the normalized cross-correlation coefficient which is calculated as a function of the displacement or lag of two time series relative to each other. For each pair of astrocytic ROI and neuronal ROI in one recording the best correlation coefficient was determined for the lags of ± 100 frameshifts, which translates to ± 15.7 s. The window size was selected large enough to theoretically fit 10 of the largest $[Ca^{2+}]_i$ transients such as seen during GBZ wash in, but small enough to be biologically relevant, as it is unlikely that in *in vitro* preparations $[Ca^{2+}]_i$ events that last maximum 2 s will have a plausible correlation to signals occurring minutes later.

Figure 18 shows the histogram of lags scoring the highest correlation coefficient of each astrocytic/neuronal ROI pair for the four conditions. If there was a tendency for astrocytic $[Ca^{2+}]_i$ transients to occur after neuronal $[Ca^{2+}]_i$ signals or just before neuronal $[Ca^{2+}]_i$ signals, the distribution of the lags would have a peak or an accumulation in the number of counts at the respective position. Except for the GBZ condition the lag distributions were quite similar and evenly distributed in all conditions. It has to be noted though, that the interpretation of the results from the untreated condition is difficult, since the number of untreated experiments is low compared to the other experiments. This is also problematic for comparison of the distribution of the cross correlation coefficients, since the histogram is comparably sparse.

For CCH-GM as well as TTX condition the lag was evenly distributed in the analysed time window, except for the 0-frame shift lag. While in the CCH-GM condition the 0-frame shift lag clearly stood out, this was not as prominent in the TTX condition, but it was still the most frequently observed lag.

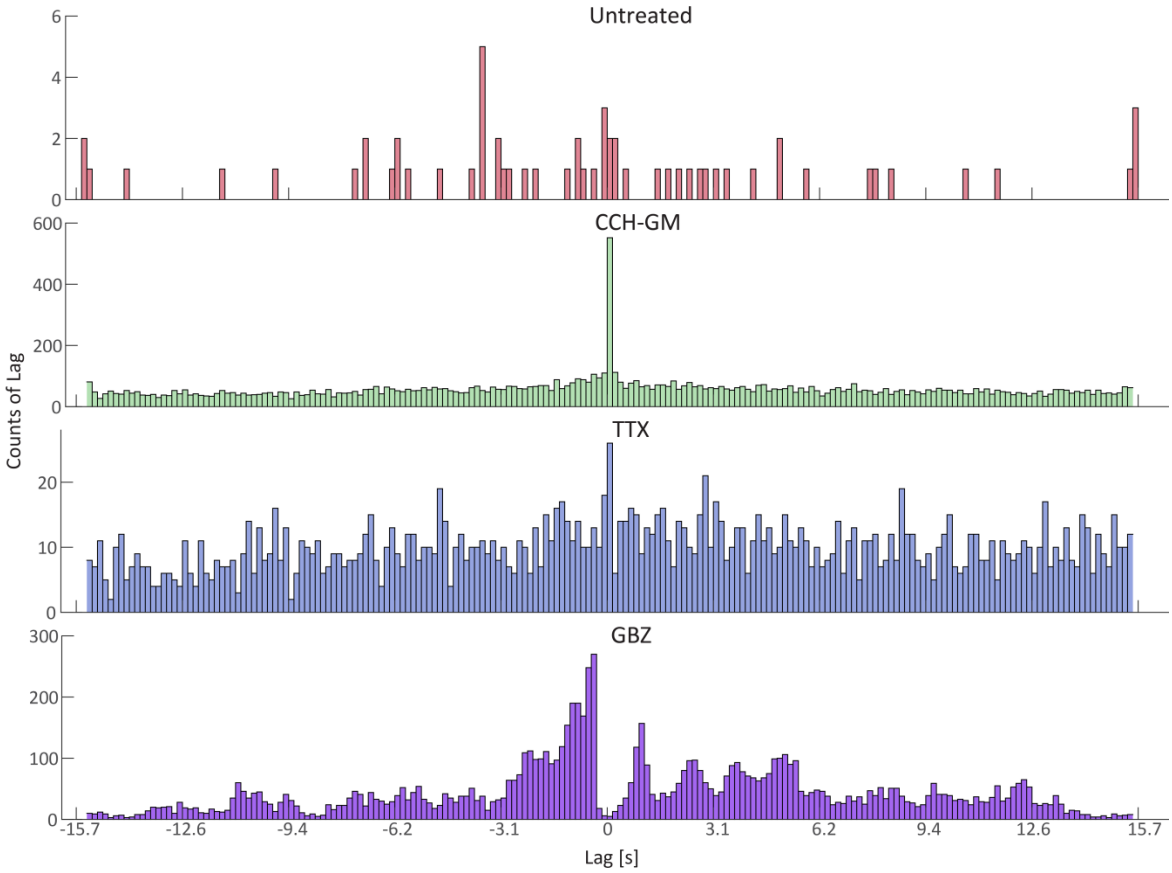

Figure 18: Maximum correlation coefficients of each astrocytic and neuronal ROI pair occur with evenly distributed lags during CCH-GM, and TTX treatment but show a pattern in GBZ experiments. *The evenly distributed lags indicate that the best correlation coefficients occur randomly. Only in the GBZ experiments, a preference for certain periodical lags indicating temporal correlation of the astrocytic and neuronal ROIs.*

This observed lag distribution means that there was no uniform or preferred sequence of the occurrence of $[Ca^{2+}]_i$ transients in astrocytic and neuronal ROIs. The comparably high number of counts in the 0-frame shift lag occurs due to signal sparsity and noise. In fluorescence traces with few peaks and some background noise, which affects astrocytic and neuronal traces (such as bleaching effects), the noise impacts the correlation coefficient stronger than the peak. Therefore, traces with few peaks will show the best correlation coefficient with 0 frame shifts to each other. This does not necessarily mean that astrocytes and neurons achieve a high correlation coefficient with 0 frame shifts, but that this was the best correlation coefficient the respective traces achieved. This becomes clear in the distribution of the cross-correlation coefficients (figure 19) which shows that the majority of coefficients in the TTX and the CCH-GM condition were below 0.5, indicating mostly low correlation in the investigated time window.

In the GBZ experiments the lag-distribution was not evenly distributed but had peaks at a few different lags (figure 18). These clusters appear somewhat periodically for lags of +5 frames (0.8 s), +15 frames (2.3 s) and +25 frames (3.9 s) and not quite as prominent at + 35 frames (5.5 s) as well as one large peak at -3 frames (0.47 s). In the GBZ experiments, as aforementioned the neuronal activity becomes synchronized and all the neurons fire together at the exact same time resulting in large peaks in the neuronal $[Ca^{2+}]_i$ traces as shown in figure 14. These peaks last for about 1.57 s, which coincides with some of the intervals of the peaks in the lag distribution.

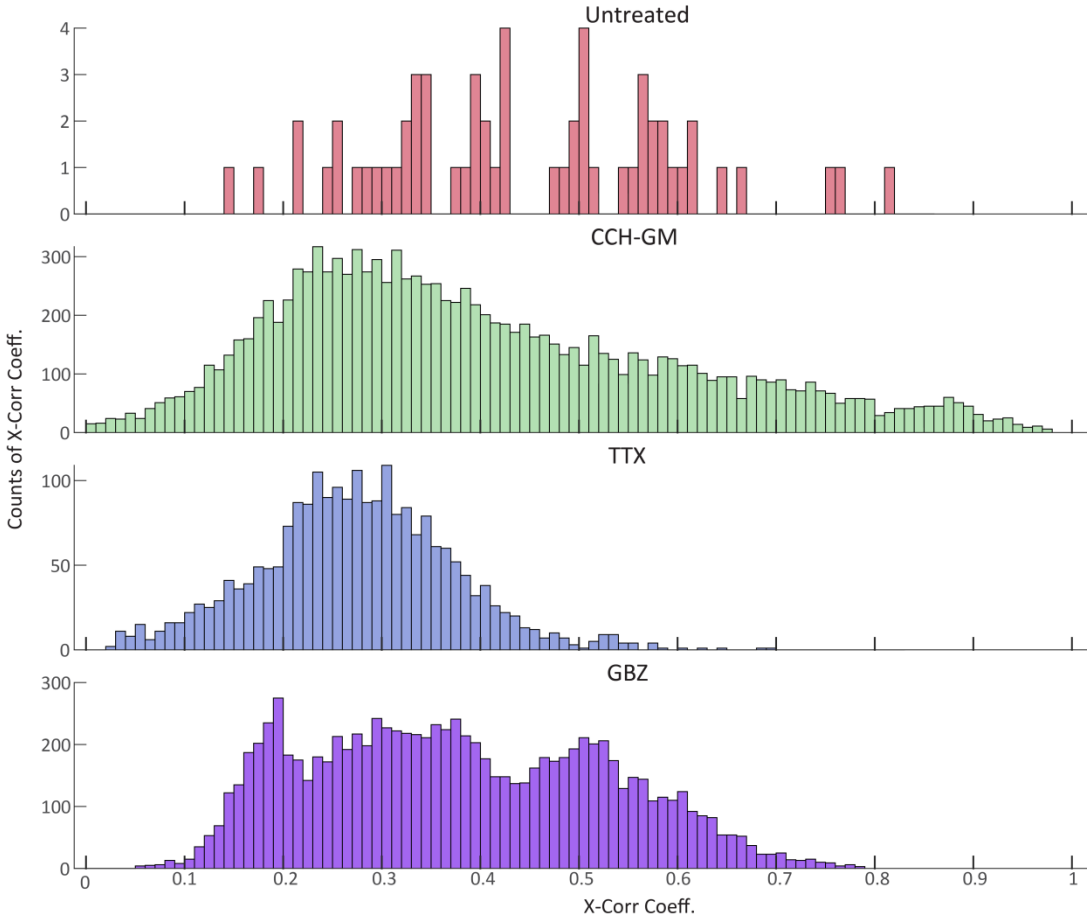

Figure 19: Most correlation coefficients are found between 0.1 and 0.5, indicating low temporal correlation in each condition*. Maximum of the correlation coefficients of each astrocytic ROI with each neuronal ROI for ± 100 frame shifts were calculated and showed overall low correlation coefficients. The distribution in CCH-GM showed a tail towards higher correlation coefficients. Also the GBZ correlation coefficient distribution shows a broad peak around 0.5.*

Since the correlation coefficient is calculated as the scalar product of the (frame shifted) traces, the large neuronal peaks will result in high correlation coefficients whenever an astrocytic $[Ca^{2+}]_i$ peak is shifted through them. Since all the neuron ROIs have the same peak at the same time, all astrocytic ROIs correlated to these synchronized neuronal ROIs will achieve a high correlation coefficient with exactly the same lag, resulting in the observed peaks in the lag distribution.

Thus, the patterns observed in the GBZ lag distribution occur due to the highly synchronous neuronal $[Ca^{2+}]_i$ activity.

This also affects the distribution of the correlation coefficients in the GBZ experiments. While the distribution was similar to TTX and CCH-GM in the range of 0 – 0.4, it had a small peak between 0.4 – 0.6 (figure 19), suggesting that GBZ increases the correlation between astrocytic and neuronal $[Ca^{2+}]_i$ signals.

Most of the correlation coefficients in the untreated, CCH-GM and TTX were in the range of 0.2 – 0.4, which can be considered to be no or low correlation. In both the CCH-GM and TTX condition there was a small and broad peak in this range. CCH-GM however, also had a tail towards the higher correlation coefficients and even a small accumulation at 0.9, which was not the case in the TTX. This could mean that in the CCH-GM condition, more astrocytic/neuronal ROI pairs correlate over time compared to the TTX condition, when neuronal signal transduction is inhibited. While this is an interesting observation it could be owed to the fact, that CCH-GM includes more experiments than TTX and a larger number of TTX potentially would have resulted in the same tail.

In order to check whether the observed distribution was the product of coincidence, the Ca^{2+} traces were shuffled. This way their temporal properties were disrupted. The correlation coefficient was calculated for the shuffled traces, again for a window of ± 15.7 s lag. In contrast to the real data, the distribution of correlation coefficients of the shuffled data is shifted closer to zero, indicating that the temporal disruption decreases the overall correlation (figure 20).

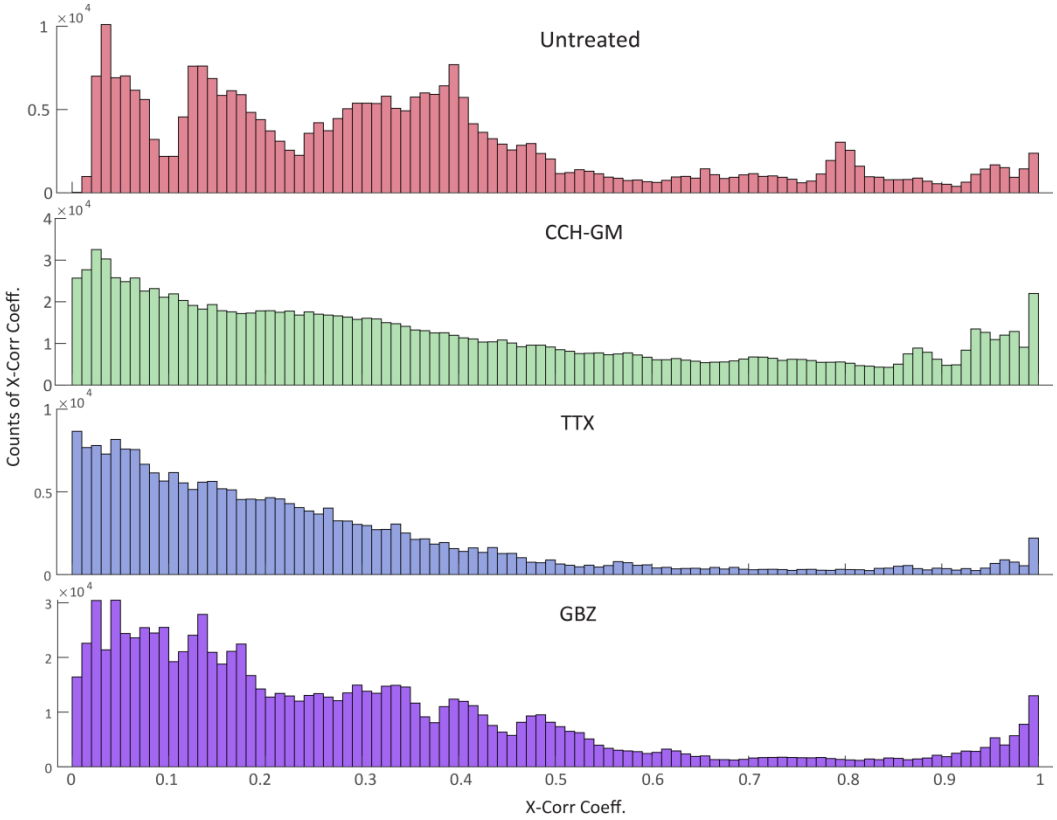

Figure 20: Distribution of correlation coefficients in shuffled datasets for each condition is similar to real data. *Each astrocytic and neuronal ROI was shuffled 1000 times and the cross correlation coefficient was calculated as before. The resulting distribution reflects the original data set, indicating that the results can be the product of coincidence.*

Concluding from this, astrocytic and neuronal ROIs indeed have mild temporal correlation that differs from the correlation coefficients that is achieved by coincidence. Nonetheless, the distribution of the real data lies well within the range of the randomized distribution and was therefore not significantly different. This was most apparent for the aforementioned tailed distribution of CCH-GMs coefficient, with an accumulation at around 0.9, which was reproduced in the shuffled data set. This indicates that the CCH-GM data by chance scored these coefficients, independently from their temporal properties. Similarly, the distribution of the GBZ coefficients was reproduced in the shuffled data set. For the untreated condition the comparison between the real data and the shuffled data set was difficult since the shuffled data set, in contrast to the other conditions, is generated from only a single experiment, which most likely was the reason for the uneven distribution.

Taken together, comparing astrocytic to neuronal ROI traces does not reveal a temporal sequence for the $[Ca^{2+}]_i$ transients when the slice was untreated, during gamma oscillations or with inhibited neuronal signal transduction. Only when neurons were pushed towards a highly synchronous state as seen in the GBZ experiments, patterns in the lag coinciding with the global neuronal activity occurred. Overall, the correlation was low, and the observed higher

correlations coefficients occurred by coincidence as seen in the comparison to the shuffled data set.

3. Discussion

3.1 Identification of astrocyte-neuron ensembles with eGFP-TTC

In the presented study the eGFP-TTC tracer system was evaluated regarding its properties of "retrograde" uptake or its release from astrocytes. This is the first time eGFP-TTC fusion protein was expressed in astrocytes. The results have important implications regarding the controversially debated gliotransmission and reveal whether the virus transduced TTC-tracer system could be used as a tool to specifically target ensembles of astrocytes and neurons, as discussed below.

3.1.1 Technical issues with virally delivered eGFP-TTC

Using an inducible transgenic mouse line (ALDH1/1-creERT2) exerting strict astrocytic expression, I showed that eGFP-TTC is not transferred from astrocytes to neurons. It was not possible to confirm this result with the two other approaches, the eGFP-TTC2A-KusO-construct as well as the combined eGFP-TTC mRNA and eGFP-TTC protein detection by FISH-IF assay due the KusO toxicity and the genomic DNA detection of the eGFP-TTC mRNA probe. For future experiments the 2A-KusO construct can be modified by using a different second reporter to avoid the observed toxicity. Another red-shifted reporter mScarlett has been reported to be non-toxic (Albakri et al., 2018) and might reliably label viable starter cells. Another potential problem in this approach is the gene configuration in the vector. In this study the KusO was linked via the 2A fragment at the 3' end of the TTC sequence. After the cleavage of the 2A fragment during translation a residue stays behind at the C-terminus which may affect the synaptic translocation of the TTC fusion protein. Therefore, cleavage of the TTC and another stationary reporter should be analysed in western blot analysis or the TTC fusion should be placed in the 3' postion of the polycistonic transcript.

In the FISH analysis the high copy number of rAAV infected genomes in the nucleus of the infected cells appeared as a major issue. Even strong DNAse treatment could not erase the viral DNA in the RNAscope® experiment. For neuronal rAAV tracer studies, where target cells lay in very distal brain regions, RNAscope® was applied successfully to distinguish neurons infected with rAAVs at their axon terminals (Reinert et.al 2019) from those being eGFP-positive through transsynaptical targeting by the eGFP-TTC protein. To analyse local transsynaptic tracing, a 5' intron should be included in the rAAV encoded expression unit. This would allow to use a mRNA

specific expression probe which is composed of two neighbouring exonic sequence and thus is not able to bind efficiently to the genomic rAAV DNA. Alternatively, a lentiviral gene transfer system can be used, since lentivirus integrates with one or few copy in the host genome (Durand and Cimarelli, 2011).

A general problem observed in all TTC experiments is the unspecific expression of rAAV delivered expression, using the "astrocyte specific" promoter GFAP. In case of the rAAV-GFAP-eGFP, and therefore most likely for the rAAV-GFAP-eGFP-TTC, the unspecific expression of the vector was restricted to a subpopulation of neurons in the DG. One possible explanation for this phenomenon is neuronal progenitor cells (NPC) located in the DG. These cells are not yet fully differentiated and it is possible that these cells have a low baseline expression of GFAP driven constructs (Freeman, 2010). This issue is specific to this region and is not observed in the pyramidal cell layer of the CA region. Results from rAAV approaches in the DG therefore have to be interpreted accordingly. Interestingly, the same promoter was used in the construct expressing Ca^{2+} indicator GCaMP for Ca^{2+} imaging experiments and no non-specific expression in hippocampal neurons was observed in this case (data not shown). However, these studies focussed on the CA region and potential weak expression in the DG may have been overlooked.

The leaky expression of the cre-dependent rAAV-GFAP-eGFP-TTC-DIO construct was very sparse and restricted to an undefined cell type outside of the DG. It remains to be resolved why these cells express the construct without prior to cre-recombinase activation. In the available literature, a cre-independent, leaky expression of the eGFP-TTC-DIO expression unit was not yet described. Depending on the application, the cre-independent expression of the construct can be neglected in many experiments. However, in the presented experiments the non-specific expression of the eGFP-TTC in neurons can lead to false positive results due to the putative translocation of eGFP-TTC to synaptically linked neurons. Interestingly, that was not the case in the ALDH1/1 mice experiment. This suggests that the cells, expressing the DIO construct in the absence of cre-recombinase, are not neurons. Nonetheless, the cre-independent expression of rAAV-GFAP-eGFP-TTC-DIO is as aforementioned not reported in the literature and has to be considered in experimental designs and the interpretation of results.

3.1.2 Transport from and to astrocytes

The comparison of the eGFP positive hippocampal area in ALDH1-Cre-ERT2/rAAV-GFAP-eGFP-TTC-DIO and rAAV-GFAP-eGFP-TCC, suggested that eGFP-TTC could be transported from one astrocyte to another. One possible explanation could be that the TTC fragment facilitates

transport from ALDH1 positive astrocyte to other astrocytes possibly at locations where only astrocytes form a sort of interface where there is no accessible neuronal process close by. As described astrocytes form gap-junctions with each other. While the gap-junction channels are too small for transport of large proteins such as eGFP-TTC, the formation of them results in effectively clamping the cell membranes of two cells together, with a tight gap of 2 – 4 nm between them (Fushiki et al., 2010). One could hypothesise, that the TTC retrograde transport requires close proximity of two cell membranes to manage the intercellular leap. In case of neurons, the synaptic cleft is exploited and in case of astrocytes potentially gap-junctions could facilitate this requirement.

Other possible explanation for the differential spread of the eGFP-TTC protein, could be the viral particles themselves. The spread of rAAV particles has been previously investigated and rAAV are known to travel distances of up to 1 mm (Reinert 2012). Other reports even claim anterograde transport of virus particles along axonal fibres (Zingg et al., 2017). How and why exactly rAAVs are transported is not conclusively explained and again the question arises, why eGFP does not spread as far as eGFP-TTC, since both reporters are rAAV delivered and should therefore be transported in similar ways. Another factor could be experimental variability of the injection process, such as injection speed and variations in the injected volume. Therefore, it remains to be elucidated if the spread is a TTC-dependent effect or a rAAV and/or methodological effect.

3.1.3 Implications on gliotransmission

The TTC tracer experiment suggests, that despite astrocytes being the third partner at the tripartite synapse, the molecular structures exploited by TTC to leave and re-enter cells retrogradely, are not present on astrocytes. Due to the discussed methodological issues the potential transfer between astrocytes could not be experimentally investigated. However, since experiments with neuronal eGFP-TTC expression do not show any eGFP positive astrocytes it is questionable if eGFP-TTC can enter these cells. This is surprising given the undisputed presence of astrocytic processes in close proximity to synapses (Araque et al., 1999). Therefore, one would expect that astrocytes could receive the TTC as off-target effect. However, this is not the case and suggests that the target structures for TTC are not present on the cell membrane of astrocytes. While this has to be confirmed in more detail, it has implications regarding the gliotransmission controversy. Vesicular release from astrocytes (Schwarz et al., 2017) similar to neurotransmitter release utilizing similar molecular machinery has been described and is one of the main arguments for the existence of gliotransmission. If TTC was able to also enter

astrocytes when it is expressed in neurons, this would have been a strong indication for the existence of gliotransmission. The finding that eGFP-TTC does not enter astrocytes, however does not lead to the conclusion that gliotransmission does not exist, as there are many possible explanations as to why the transfer does not take place. The full target structures recognized by TTC are not known, but it is possible that they do not exist in astrocytes. Another issue could be the spatial proximity. Despite astrocytic processes being positioned close to synapses, the synaptic cleft spanning 20 nm is a very tight construct and bridged by interactions of membrane proteins in the pre- and postsynapse, like neurolegins and neuroexins (Craig and Kang, 2007). As suggested before close proximity of two adjacent cell membranes could be a possible requirement for the TTC transport. As consequence eGFP-TTC cannot be used as tool to identify astrocyte-neuron interactions. However, other retrograde tracers may still yield the potential to achieve this goal. One example is the rabies tracer system, which exploits the retrograde properties of the rabies virus particles itself (Schnell et al., 2010). Similar to TeNT it infects axon terminals in the periphery and is then transported retrogradely into the central nervous system. It replicates in cell bodies and is then transferred via synapses into higher order neurons. To use rabies as a monosynaptic tracer tool it has been modified by deleting the gene essential for packing and transsynaptically spreading of the virus particles (Mazarakis et al., 2001). This traps the virus in its primary infected cell. By providing the rabies glycoprotein specifically in the cells of the “starter region” the otherwise glycoprotein deficient rabies vector is packaged and can “jump” across one synapse into the next higher order neurons.The virus is then trapped in the target cell because the target cell cannot provide the rabies glycoprotein (Wickersham et al., 2009). This system equipped with fluorescent reporters was exploited for many tracer studies elucidating the neuronal connectome (Callaway, 2005; Haberl et al., 2015; Osakda et al., 2012; Rancz et al., 2011; Schwarz et al., 2015). The exact mechanism of retrograde infection is also not fully understood (Ginger et al., 2013). Nonetheless, several neuronal tracer experiments “unexpectedly resulted in the labelling of astrocytes” (Deshpande et al., 2013). Thus in contrast to TTC, the uptake mechanism of the rabies virus seems to work to a certain degree to visualize astrocyte – neuron interactions and might potentially be used for selective labelling of astrocyte-neuron ensembles.

3.2 $[Ca^{2+}]_i$ activity during gamma oscillations

Besides elucidating the astrocyte to neuron connectivity with the genetically encoded tracer system, the second part of the presented study investigated the physiological interactions of hippocampal astrocytes and neurons. The astrocytic as well as neuronal $[Ca^{2+}]_i$ activity during

gamma oscillations and how the two cell populations' activities correlate to each other was analysed in organotypic cultures. Results clearly show, that astrocytic and neuronal $[Ca^{2+}]_i$ activity is not significantly altered by CCH-GM. Moreover, astrocytes and neurons do not show any specific activity pattern during gamma oscillations indicating that neither in astrocytes nor in neurons can the $[Ca^{2+}]_i$ activity pattern be used to predict the oscillatory activity and thus basal state of a brain.

3.2.1 Spatial Characteristics: Population stability

While the temporal aspects of $[Ca^{2+}]_i$ activity were the main focus of this study, the $[Ca^{2+}]_i$-ROIs spatial distribution between consecutive recordings was compared. By comparing the $[Ca^{2+}]_i$ activity of two different but subsequent recordings from the same hippocampal organotypic slice, I found that astrocytic ROIs were less stable from one recording to the other compared to neuronal ROIs.

One important aspect in this analysis is the ROI detection. Since this is the first step in the analysis, false detection or missing of ROIs impacts the following analysis results. The applied CNMF method is one out of numerous automated segmentation approaches (Agarwal et al., 2017; Poskanzer and Molofsky, 2018; Srinivasan et al., 2015). The selected method delivered results in accordance to manual test selection of ROIs, however tended to false positively detect ROIs. To take account for this, a manual validation step was included. Therefore, the presented image processing results have been controlled to the best of knowledge, but it is nonetheless possible that different approaches would have delivered different ROIs. Especially, for the spatial analysis this is a potential source for biased results. However, it was possible in case of the neuronal ROIs to detected them a second time in the second recording. Therefore, the reason that the majority of astrocytes could not be re-detected does not lie in the ROI detection and the population stability experiments can be regarded as an internal control for the automated segmentation.

Another aspect to consider in the interpretation of spatial distribution results is that in the respective two consecutive recordings, different pharmacological manipulations were applied. Since the spatial comparison of ROIs was not the focus of the presented study, the n-numbers of the applied pharmancons are too low for statistical analysis. No similar analysis has been done before, thus it would be interesting to further investigate whether different pharmacological agents have different impacts on the ROI stability. From the presented results it can be concluded already that the two cell populations react differently. While the active neuron population remains stable the astrocyte population appears unstable. The astrocytic population

instability is most likely a property inherent to astrocytes that occurs independently from external manipulations. This conclusion is accordance to the other results in this work, that indicate that astrocytic $[Ca^{2+}]_i$ transient properties, such as frequency and peak shape, are not affected by external manipulations, gamma oscillations or neuronal $[Ca^{2+}]_i$ transients.

3.2.2 Temporal characteristics: $[Ca^{2+}]_i$ peaks

The analysis of the number of peaks in the relative fluorescence intensity showed in all conditions for astrocytes comparably low numbers ranging between 0 and 0.002 pks/s per ROI. To put this number into perspective, the maximum pks/s observed in astrocytes is 0.002 pks/s which means if there was only a single ROI in this respective recording, it would show a peak every 500s (approximately 8.3 min). This is not an unusual finding as spontaneous astrocytic $[Ca^{2+}]_i$ activity has been reported to be sparse *in vivo* and *in vitro* if not externally stimulated (Tang et al. 2015). It has to be noted however, that definition of a peak in the relative fluorescence intensity depends on applying a threshold. In this study the threshold for peak detection allowed the detection of only high and prominent peaks. Applying, a less stringent threshold would potentially increase the number of peaks at the cost of false positive detection. Peak detection in noisy data is a problem found throughout literature (Prada et al., 2018) and different methods exist to solve this issue but result in different biases. This has to be considered in the interpretation of the data. In the presented study only high and prominent peaks were considered and these did not show a change in frequency upon CCH-GM, TTX or GBZ. I cannot conclude that smaller peaks, that potentially come from smaller $[Ca^{2+}]_i$ transients behave in a similar way, since the applied method did not detect the smaller $[Ca^{2+}]_i$ transients.

The same is true for the analysed slope ratio. Results of the slope ratios, similarly to the peak frequency, show no significant change in the astrocytic and the neuronal $[Ca^{2+}]_i$ transients. In all four conditions the variability of the slope ratios is quite high. Nonetheless, the slope ratios of astrocytic $[Ca^{2+}]_i$ transients measured in the TTX and GBZ experiments trend towards a more symmetric peak shape. This is interesting since the two drugs have different targets and opposing effects. In case of TTX this means that hampering neurotransmission could have an impact on astrocytic $[Ca^{2+}]_i$, namely rendering astrocytic $[Ca^{2+}]_i$ transients decay time shorter. Since astrocytes do not express the voltage dependent sodium channels targeted by TTX (Verkhratsky and Nedergaard, 2017), this effect can only occur due to the lack of neuronal input. In case of the GBZ experiments neurotransmission is effectively increasing as inhibitory input is blocked. However, astrocytes are known to express $GABA_A$ receptors, thus a direct effect of GBZ on astrocytes cannot be excluded (Bekar and Walz, 1999).

In conclusion, the analysed properties of the peaks in the relative fluorescence of the Ca^{2+} indicators are independent from the pharmacological manipulations as well as from CCH-GM.

3.2.3 Interactions of astrocytes and neurons during gamma oscillations

It is known that gamma oscillations in the brain are important for cognitive processes as well as memory and learning (Bartos et al., 2007; Buzsaki and Draguhn, 2004). Despite numerous studies elucidating the cellular underpinnings of these oscillations it is unknown how exactly they occur *in vivo* as well as in slice preparations. Most studies investigating this however, never considered that astrocytes potentially contribute to this process and the models development for the gamma oscillations circuit are solely based on neuronal signalling.

Lee et al. investigated for the first time how astrocytic $[Ca^{2+}]_i$ elevations are linked to gamma oscillations and found that they precede the onset of the oscillations (Lee et al., 2014). The here presented study cannot confirm this result, since the acute wash-in phase of CCH was not included in the analysis. These time windows were excluded as it is known that CCH induces immediate response $[Ca^{2+}]_i$ transients in astrocytes. These occur due to direct stimulation of AChRs expressed by astrocytes (Shelton and Mccarthy, 2000), which is why in the presented study also TTX was washed in together with CCH as control condition. Indeed, in the initial phase of the CCH wash-in, an immediate astrocytic $[Ca^{2+}]_i$ increased was observed for a very short time. Since Lee et al., used the chemical Ca^{2+} indicator fura-2, a Ca^{2+} indicator with much lower signal rise and decay time, potentially the direct CCH effect on astrocytes was misinterpreted as an astrocytic $[Ca^{2+}]_i$ elevations preceding the onset of gamma oscillations (Lee et al., 2014).

Nonetheless, Lee et al. could show, that $[Ca^{2+}]_i$ dependent vesicular release of transmitters is required for the maintenance of CCH-GM, since genetically blocking vesicular release from astrocytes decreased the gamma oscillation duration (Lee et al., 2014). While the direct interactions from astrocytic $[Ca^{2+}]_i$ transients and neuronal activity remain unclear in their study, it suggests that astrocytic $[Ca^{2+}]_i$ transients precede neuronal $[Ca^{2+}]_i$ transients, since the $[Ca^{2+}]_i$-dependent glutamate release from astrocytes lower the threshold for APs. This was investigated in the presented work by cross-correlating the astrocytic and neuronal $[Ca^{2+}]_i$ transients during CCH-GM. Results showed that astrocytic $[Ca^{2+}]_i$ and neuronal $[Ca^{2+}]_i$ transients do not follow a specific sequence or have a strong temporal correlation overall.

The cross-correlation is a good measure to find out whether two time series repeatedly act together or in a specific sequence relative to each other. The comparably low cross-correlation coefficients either mean that astrocytic $[Ca^{2+}]_i$ and neuronal $[Ca^{2+}]_i$ transients do not correlate, or that the correlations are more subtle. As the cross correlation always compares all

time points of a respective time series with another time series, sparse correlations could be overlooked. If for example each neuronal transient is preceded by an astrocytic $[Ca^{2+}]_i$ transient, but not all astrocytic $[Ca^{2+}]_i$ signals are followed by a neuronal event, the cross correlation would not detect this peak-wise correlation. The coefficient would indicate no correlation while some, but not all astrocytic $[Ca^{2+}]_i$ peaks show a similar pattern in their occurrence.

A way to work around this would be to isolate neuronal and astrocytic events with a feasible time window around it. A similar analysis was performed by Poskanzer and Yuste when analysing cortical state switches (Poskanzer and Yuste, 2016). However, this again relies on peak extraction, which as discussed, biases the results.

Future investigations need to refine analysis tools to potentially reveal a correlation of a certain subpopulation of astrocytic $[Ca^{2+}]_i$ events with neuronal $[Ca^{2+}]_i$ events. Such an approach would require classifying $[Ca^{2+}]_i$ events in astrocytes and/or identify potential subpopulations. It is known that $[Ca^{2+}]_i$ transients are triggered through different pathways and so far, $[Ca^{2+}]_i$ transients are mostly classified according to their size and position in the cell such as soma or micro domain (Agarwal et al., 2017; Shigetomi et al., 2013). In the presented study it was not possible to discriminate the subcellular structures due to limitations in the imaging resolution, since an epifluorescence microscope was used. Thus, the here observed $[Ca^{2+}]_i$ events are most likely a mix of differently triggered $[Ca^{2+}]_i$ transients. Potentially existing patterns or correlations in only a subset of the $[Ca^{2+}]_i$ events could therefore be masked. Ideally, other molecular factors, that discriminate $[Ca^{2+}]_i$ signals from other $[Ca^{2+}]_i$ signals should be used for a better understanding of the function and interaction of $[Ca^{2+}]_i$ transients in astrocytes. Moreover, could multiphoton approaches help to better resolve the spatial distribution also in the z-plane and therefore allow the distinction of different microdomains.

In conclusion, with the given methods I was not able to detect direct effects or correlations of astrocytic $[Ca^{2+}]_i$ signals during gamma oscillations. This can either mean that these correlations indeed do not exist, or the applied methods are not suited to distinguish subtle changes in the activity. While Lee et al make a strong case for astrocytic involvement during gamma oscillations (Lee et al., 2014), especially *in vivo*, from my *in vitro* studies I cannot confirm that $[Ca^{2+}]_i$ transients in astrocytes are involved or affected by CCH-induced gamma oscillations.

4. Methods

4.1. Molecular biological methods

All standard methods for plasmid cloning, transformation of competent E.coli bacteria cultures and PCR techniques were adapted from Howland, 1996 and are described in brief below:

4.1.1 PCR

DNA templates (100 ng) were each amplified by Phusion high-fidelity DNA polymerase (NEB, Frankfurt) 2 U/µL in 20 µl reaction volume supplied with respective flanking forward and reverse primers 10 µM each, 10 mM dNTPs, and Phusion reaction buffer. Amplification was achieved with 35 cycles of denaturation at 98° C for 10 s, annealing at 60° C for 30 s, extension at 75° C for 30 s/1kbp and a single final extension cycle at 60° C for 5 min in the ABI 7500 cycler (Applied Biosystems, Foster City, CA, USA).

4.1.2 DNA restriction, electrophoresis and gel purification

All DNA restriction enzymes were obtained from NewEngland Biolabs (Ipswich, Massachusetts, USA). DNA restriction for either qualitative check of purified plasmid or preparative digest for cloning was performed with 1 U of respective restriction enzyme per 1 µg of DNA in restriction buffer. Restriction conditions were kept according to manufacturer's instructions. Restriction reaction was stopped by heat inactivation at 65° C when necessary and results were checked by agarose gel electrophoresis. 1-2% (w/v) agarose were brought in solution in TAE buffer (20 mM Tris, 10 mM Sodium acetate, 0.5 mM EDTA, pH 7.8) and 0.5 µg/ml EtBr were added for visualization of DNA bands. DNA fragments were separated by electrophoresis at 150 V for 35 min. lambda-DNA (Fermentas/Thermo Fisher Scientific) digested with Sty-1 was used as size marker. DNA bands were visualized on transilluminator.

For gel extraction of DNA from preparative gels, respective bands-containing gel regions were carefully cut out and DNA was purified with the zymoclean gel DNA recovery kit (zymo research, Freiburg, Germany) according to the manufacturer's instructions. In brief, the DNA containing gel is melted and washed over anion-exchange column and DNA is eluted with 30 µl elution buffer.

4.1.3 Ligation

For cloning of rAAV constructs, inserts amplified with PCR were joined in rAAV backbone by ligation. The linear DNA fragments with compatible sticky ends were joined under ATP consumption with T4 DNA ligase (Roche, Penzberg) in 20 µl volume containing the ligase, ATP and reaction buffer. Backbone and insert were supplied in different molar ratios and 1 U of T4 ligase per 1 pM DNA was added. Ligation mix was incubated for 2 hrs at RT.

4.1.4 Plasmid amplification: Transformation and plasmid purification from E.coli

rAAV- vector plasmids were transformed into SURE competent *E.coli* (Stratagene, California). 100 µl of competent cells at a density of $1x10^8$ were thawed on ice and 1 µg of the plasmid DNA was added to the cells and incubated for 20 min on ice. Cells were then heat-shocked for 30 s at 42° C and immediately placed on ice again for 2 min. 300 µl of pre-warmed LB medium (10 g/l Bacto Trypton, 5 g/l Bacto Yeast Extract, 10 g/l NaCl, 4 mM MgSO4, 10 mM KCl, pH 7.6 (KOH)) were added. Cells were then incubated for 1 hr at 37° C before the bacteria suspension was plated on LB-agar plates (15 g/l Agar, 5 g/l Bacto Yeast Extract, 10 g/l NaCl, 4 mM MgSO4, 10 mM KCl, pH 7.6 (KOH)) containing 0.2 mg/mL ampicillin (Sigma-Aldrich, Steinheim) and incubated overnight at 37° C. Colonies were picked and grown in 2 ml starter culture LB-medium with ampicillin (Merck KGaA, Darmstadt, Germany) for 12 hrs at 37° C and 200 µl were used for inoculation of 200 mL TB medium (12 g/l tryptone, 24 g/l yeast extract, 4 ml/l glycerol, 0.17 M KH2PO4, 0.72 M K2HPO4) with ampicillin for overnight culture at 37° C.

Plasmids were purified from *E.coli* using HiSpeed Plasmid Maxi Kit (Quiagen, Venlo, Netherlands) according to the manufacturer's instructions. In brief, bacteria were pelleted at 6000 x g for 15 min at 4° C. Cells were resuspended and lysed for 5 min and subsequently neutralized. Insoluble protein phase was fractionated by centrifugation at 6000 x g for 30 min at 4° C. Supernatant was filtered and allowed to run over the HiSpeed Plasmid Maxi Kit column by gravity flow. After washing the column plasmid DNA was eluted with 500 µl ultra-pure water.

4.1.5 Cloning of rAAV vectors

pAAV-Syn-eGFP-TTC was kindly provided from Prof. Dr. Thomas Kuner. The pAAV-GFAP-eGFP-TTC was produced by isolating the eGFP-TTC fragment from the syn-eGFP-TTC construct using

XbaI and SalI restriction enzymes. The isolated 2786 bp eGFP-TTC fragment was inserted into GFAP-tdTomato backbone where the td-Tomato fragment had been excised with NehI and SalI, by sticky end ligation.

The pAAV-GFAP-eGFP-TTC-2A-KO plasmid was cloned by fusion PCR. The 2A-KO fragment from the pAAV-syn-tTa-2A-KusO (obtained from R. Sprengel) plasmid was amplified with custom made primers flanking the 2A-KusO including two flanking restriction sites (NotI and XhoI) on each end. (Primers1. 5'CCACCCGCAGTTCGAAAAACTCGAGGGCAGAGGAAGTCTTCTAA CATGC3', Primer 2: 5'GAT-AAGCTTGCGGCCGCTTTACTTGTACA 3'). Primer 1 is designed to be half complement of the 5' end of the TTC-coding region of the GFAP-eGFP-TTC plasmid. Similarly the 5' end of the TTC-coding region from the GFAP-eGFP-TTC coding plasmid including two flanking restriction site (EcoRI and NotI) was amplified (Primer 3: 5'AATCTTGATAGAATTCTAAGAGTA3', primer 4: 5' TCTGCCCTCGAGTTTTTCGAACT GCGGGTGGCTCCAC3'). The two amplified fragments were fused in a fusion PCR reaction with primers 1,3 and 4 as described in (Yon and Fried, 1989). The PCR product contains the fusion of the two fragments which was then digested with EcoRI to produce a sticky end. Likewise, the GFAP-eGFP-TTC plasmid was digested with EcoRI and NotI for sticky end ligation.

pAAV-GFAP-eGFP-TTC-DIO was kindly cloned by Michaela Kaiser. In brief, the GFAP promotor was PCR- amplified from the pAAV-GFAP-tdTomato (primer forward: TTTGGTACCAAGATCTAACAT-ATCCTGGTGTGGAGTAGGGGACGC, primer reverse: TTTCGAATTCTCGAGTCTAGAGCTAGCCTATAGTG AGTCGTATTAAGTAC) and subcloned into a cloning vector containing the MCS flanked by DIO recognition sites, using KpnI and EcoRI restriction sites. The eGFP-TTC fragment was isolated from the pAAV-Syn-eGFP-TTC with XbaI/NheI digestion and subcloned into the MCS of the DIO-containing construct.

All ligation and transformation was performed as described above. All plasmids were sequenced after cloning with GATC service. pAAV-GFAP-eGFP, pAAV-GFAP-GcaMP6f and pAAV-GFAP-tdTomato were obtained from addgene (eGFP: Cat#50473,https://www.addgene.org/50473/, GcaMP6: Cat#52925, https://www.addgene.org/52925/, tomato: Cat#44332 https://www.addgene.org/44332/).

4.1.6. Virus production: transfection of HEK293 and rAAV purification

Cell culture maintenance for virus production was kindly performed by Annette Herold. HEK293 cells were cultured in MEM, 5% or 10% FCS, 100 U/ml Penicillin/Streptomycin, 2 mM L-glutamine. Recombinant AAV (rAAV) vectors were produced in HEK293 cells, co-transfected with

helper plasmids encoding the rep and cap genes of serotype 1 and 2 adenovirus (pH21), adenoviral helper genes (pF6Δ) and the respective expression construct, as described in During et al., 2003.

HEK293 cells were plated in 10 cm cell culture dishes at a density of 4 x 10^6cells per dish and allowed to reach 50-60% confluence overnight. A total of 20 ng of plasmid mix was calcium-phosphate transfected and cells were stored at 37° C, 3% CO2 atmosphere. 60 hrs post transfection cells and supernatant was harvested and pelleted (3000 x g, 10 min). Supernatant was decanted and stored on ice for later virus purification, while the pellet was resuspended in TNT buffer (20 mM Tris, 150 mM NaCl, 1% TritonX-100, 10 mM MgCl2, pH 7.5) and incubated for 10 min at RT. 4 U/ml benzonase (Sigma-Aldrich, Steinheim) is added and incubated 1 hrs at 37° C. Supernatant and cell lysate are centrifuged for 10 min at 3000 x g and subsequently sterile filtered with 22 µm pore size filter to separate insoluble material. Virus purification was achieved by affinity chromatography using the ÄKTA prime plus system (GE Healthcare, Europe GmbH) in combination with a HiTrap sepharose column (1 ml HiTrap AVB Sepharose HP column, GE Healthcare GmbH). The column was equilibrated with 10 ml PBS (10 mM NaCl, 2.7 mM KCl, 10 mM Na2HPO4x2H2O, 1.8 mM KH2PO4) at 0.5 ml/min before virus-containing cell lysate and supernatant was pumped through the column at 2 ml/min to allow virus particles to bind to it. Virus particles were eluted with 50 mM glycine at pH 2.7 at a flow rate of 1 ml/min and collected in 1 ml fractions and neutralized with Tris-HCl pH 8.0. Fractions containing eluted virus were identified by the peak in UV absorbance. Respective fractions were washed three times in 4 ml sterile PBS and concentrated in cellulose concentrator tubes (Amicon Ultra tubes, Merck Millipore, Darmstadt, Germany) by spinning at 3000 x g for 4 min. Purified and concentrated virus was again sterile filtered (Acrodisc, Renner, Dannstadt-Schauernheim, Germany) and stored at -80° C until used.

4.1.7. Hippocampal slice cultures

Hippocampal slice cultures were prepared from 8-days-old rats. Animals were decapitated and their heads quickly placed in ice-cold dissection buffer (10 mM MgCl2, Merck; 20 mM HEPES in Ringer solution; pH 7.2)). Brains were quickly removed and while constantly kept in ice-cold dissection buffer the hippocampus was separated hemisphere-wise. Isolated hippocampi were cut into 350 µm thick slices with a tissue chopper (Campden Instruments Ltd., England). Slices were carefully placed on cell culture plate inlets (PicM0REG50, MerckMillipore, Darmstadt, Germany) and cultured in 6-well-plates with 1 ml hippocampal slice medium (50% MEM; 25% EBSS ; 25% horse serum , 2% B27, 2% Glucose (32% in MEM)). Slices were maintained at 37° C at

5% CO2. Every 3 days 50% of medium was exchanged. Hippocampal slice preparation was kindly carried out by Andrea Lewen. Slice cultures were infected with Ca^{2+} -indicator-expressing rAAVs at day 3 post preparation by placing 0.2 µl droplets of viral solution on the slice. Slices were used for imaging earliest on day 10 post infection.

4.2. Animals

4.2.1 Legal aspects

All animal handling and experimental procedures were performed according to the animal welfare guidelines of the Max Planck Society. Animal experiments were performed under the license at the Regierungspräsidium Karlsruhe G-100/15 and G-32/18.

4.2.2 Housing

Mice were housed individually or in pairs of two in Makrolon type II cages in an on-site animal facility. The facility is kept at a 12hrs/12hrs light/dark circle with the light phase starting at 7 am. Temperature is kept at 23-24° C and at a humidity of 56%. Animals had access to food and water *ad libitum* throughout the experiments. All procedures were performed during the light phase.

4.2.3 Stereotaxic rAAV delivery

For stereotactic injections animals were anesthetized either by isoflurane (Baxter, Unterschleiheim,Germany) inhalation (2% for anaesthesia initiation and 1.5% during operation) or by i.p. injection of anaesthesia mix consisting of Fentanyl (0,24 mg/kg body weight), Midazolam (0.93 mg/kg body weight) and Medetomidin (0,715 mg/kg body weight). Anaesthesia was monitored by testing pain reflexes before placing animals in the stereotactic frame and throughout the operation. Animals were placed in the stereotactic frame (David Kopf Instruments, Tujunga, CA USA) and eyes were covered with ointment (Bepanthene, Bayer, Leverkusen, Germany) to prevent damage. After exposing the skull its position was adjusted to level the hemispheres in all spatial dimensions using the digital display console. For Injections into the CA1 region of the hippocampus and cortex the following coordinates relative to bregma were used: HPC: anteroposterior (AP) -2.18 mm; mediolateral (ML) ± 1.5 mm; dorso-ventral (DV) from pial surface -1.2 mm for CA1, -0.45 for cortex. At the marked coordinates a small craniotomy was made using a dental drill (Osada Electronic, Los Angeles, CA, USA). A glass injection micropipette (inner diameter 9 µm, Blaubrand intraMark, Wertheim, Germany) was

filled with viral solution by applying negative pressure to the pipette using a syringe. At the respective injection sites a total volume of 100 nl was injected at a rate of approximately 30 nl/min. After 3 min post injection the micropipette was retracted, the scalp sutured. The anaesthesia was antagonized with an antidote mix of Atipamezol (1.898 mg/kg body weight), Flumazenil (0,506 mg/kg body weight) and Naloxon (0,304 mg/kg body weight). Animals were placed in their home cage on a heating plate to prevent hypothermia. On the days following operation animals were treated with Carprofen (5 mg/kg body weight) to reduce pain.

4.2.4 Perfusion

Perfusion was performed on anesthetized animals. Animals were injected with pentobarbital ("Narcoren", Janssen-Cilag GmbH, Neuss, Germany) at 500 mg/kg body weight and as soon as pain reflexes were absent the heart was exposed by thoracotomy. Animals were transcardially perfused through the left ventricle with 25 ml PBS followed by 25 ml of 4% PFA in PBS. The brain was removed from the skull and placed in 4% PFA at 4° C overnight for post fixation and washed and stored in PBS until further processing. Brains for RNAscope® assays were placed in 15% sucrose in PBS for 24 hrs and 30% sucrose for another 24 hrs before they were frozen into cryomold for cryosectioning.

4.2.5 Cryosections

For RNAscope® assay brains were embedded in cryo embedding medium (Jung, Leica Microsystems, Nussloch, Germany) and stored at -80° C until they were sliced. For slicing the cryotome (Leica, Wetzlar, Germany) was set to -22° C and the embedded brain was stored in the cryotome for 60 min prior slicing for temperature equilibration. Slices were cut at 20 µm thickness and stored free-floating in anti-freeze (25% Glycerol, 30% Ethylene glycol, 50 mM PBS) solution at -20° C.

4.2.6 Vibratome sections

For immunohistochemistry PFA-fixed brains were sliced coronal or horizontal at 70 µm thickness using a vibratome (Leica, Wetzlar, Germany). Sections were collected and stored free-floating in PBS for short term storage. For long-term storage slices were placed in anti-freeze solution and stored at -20° C.

4.3. Histological Assays

4.3.1 Immunofluorescence assays

For immunofluorescence assays slices were placed in 24-well plates free floating in PBS. All incubation steps were performed gently shaking. Slices were blocked for 2 hrs at RT in blocking buffer (5% normal goat serum, 0.5% TritonX-100, 1% bovine serum albumin in PBS) followed by 5 min wash in 0.5% TritonX-100 in PBS. Primary antibodies were applied according to table 1 in 0.5% TritonX-100, and 1% BSA in PBS at 4° C. Slices were washed 3 x 10 min in 0.5% TritonX-100 in PBS before fluorophore conjugated secondary antibody (dilutions specified in table 2) was applied and incubated for 2 hrs at RT. Slices were washed in PBS 2 x 10 min at RT and counterstained with DAPI diluted 1:10000 in PBS for 15 min at RT. After final wash in PBS slices were mounted on glass slides (Menzel-Gläser, Braunschweig , Germany), air dried for 10 min and embedded in aqua polymount (Polyscience, Warrington,USA).

Table 1: Primary antibodies

Primary antibody	Species	Dilution	Manufacturer	Cat#	Lot#
GFP	chicken	1:1000	Abcam	ab13970	236651-25
NeuN	mouse	1:1000	Merck	clone A60	2987527
GFAP	chicken	1:1000	Biolegend	PCK-591P	Poly28294
GFP	rabbit	1:1000	Abcam	ab 6556	GR249192-1

Table 2: Fluorophore conjugated secondary antibodies

Secondary antibody	Species	Dilution	Manufacturer	Cat#	Lot#
Cy3-conjugated α-chicken	donkey	1:400	Jackson Immuno Research	703-165-155	120431
Cy3-conjugated α-mouse	Goat	1:400	Jackson Immuno Research	115-165-003	134635
Cy3-conjugated α-rabbit	goat	1:400	Jackson Immuno Research	111-165-144	103953
FITC-conjugated α-chicken	donkey	1:400	Jackson Immuno Research	703-545-155	123496
FITC-conjugated α-rabbit	Goat	1:200	Jackson Immuno Research	111-095-144	94765

4.3.2 In situ hybridization RNAscope® and Immunofluorescence

RNAscope® assay was performed according to manufacturer's instructions with all solutions provided in RNAscope®2.5 HD Reagent Kit-RED (Advanced cell diagnostics Inc., Newark, California, USA). Cryosections were carefully washed in 50% EtOH and mounted on Superfrost glass slides (Thermo Fisher Scientific) and dried on a heat plate at 37° C for 30 min. Slices were then dehydrated with 70% EtOH for 5 min and 100% EtOH for 5 min by submerging the slides in the solution. Glass slides were then baked at 60° C on a heat plate. Before the RNAscope® assay was performed slices were treated 10 min with peroxidase at RT by placing 2 drops of the peroxidase solution on the horizontally stored slices. Slices were then submerged in boiling target retrieval buffer for 3 min, washed in ultra-pure water, and treated with protease for 15 min at 40° C in the HybeZ oven (Advanced cell diagnostics Inc., Newark, California, USA). Subsequently, slices were washed in ultra-pure water and approximately 40 µl of probe was applied to the slices and incubated for 2 hrs at 40° C in the HybeZ oven. Hybridization signals were amplified with the RNAscope® amplification kit, placing approximately 40 µl of each amplification buffer 1-6 on the slice and incubate them alternatingly 30 and 15 min at 40° C except for steps 5 and 6 which were performed at RT. Between each step slices were washed twice in wash buffer. Each slice was then incubated with 40 µl of detection solution for 10 min at RT and washed in water. After the RNA detection, slices were additionally immunolabeled for GFP protein. Immunofluorescence assay was performed as described above, however slices were kept mounted on glass slides and solutions were directly dropped on the slices.

4.3.3 Fixed tissue imaging

Immunofluorescence experiments as well as combined RNAscope® and immunofluorescence signals were imaged with a 10x objective of an epifluorescence microscope(Leica Microsystems, DM6000 for overview scans. High magnification images were taken with a confocal microscope (Leica Microsystems, SP8) using 63x objective (Leica Microsystems, #11506350) objectives. All fluorophores were imaged in sequential scans to avoid bleed-through. Fluorescent images were processed in Fiji (ImageJv1.51h, NIH, Bethesda, USA) and Adobe IllustratorC5 (Adobe systems, San Jose, USA).

4.4. Live imaging and electrophysiological recordings

4.4.1 Live imaging of slice cultures with LFP measurement

Hippocampal slice cultures were infected with two Ca^{2+} indicator expressing rAAVs simultaneously. One expressed the green fluorescent Ca^{2+} indicator GCaMP6f under control of the astrocyte specific gfABC1D-promotor (further referred to as GFAP), while the second virus expressed the red fluorescent Ca^{2+} indicator jRGeco1a under control of the neuron-specific synapsin promotor. After 3W incubation time slices were carefully cut out of the cultured membrane and placed in a submerged imaging chamber, perfused at 5 ml/min with oxygenized artificial cerebrospinal fluid (ACSF) (129 mM NaCl, 3 mM KCl, 1.25 mM NaH2PO4, 1.8 mM MgSO4, 1.6 mM CaCl2, 21 mM NaHCO3, and10 mM glucose, saturated with 95% O2, 5% CO2, pH 7.3;) at 32° C. $[Ca^{2+}]_i$ transients of astrocytes and neurons were recorded simultaneously using an Olympus BX51WI microscope equipped with 20X objective and a CCD camera (ORCA-ER, Hamamatsu Photonics, Hamamatsu, Japan) at 6.5 Hz and 13 ms exposure for each channel. One recording session was 2500 frames in 6.5 min. At the same time LFPs with a field electrode placed in the CA3 region of the slice as described here Justus schneider 2015. In brief, the GB150F-8P borosilicate glass electrodes (1–2 Mohm resistance) (Science Products GmbH, Hofheim, Germany) was back-filled with ACSF. With a mechanical micromanipulator (MM 33; Märzhäauser, Wetzlar, Germany) the electrode was positioned in pyramidal cell CA3 cell layer. Field potentials were amplified with EXT 10-2F amplifier (npi Electronic GmbH, Tamm, Germany). The signals were simultaneously low-pass filtered (3 kHz), and digitized with CED 1401 interface in the Spike2 software (Cambridge Electronic Design, Cambridge, United Kingdom). During the imaging sessions either carbachol (20 µM), carbachol+TTX (20 µM + 1 µM) or gabazine (5 µM) were washed in continuously, as indicated.

4.5. Data analysis

In case of the slice culture experiments image data was analysed using a version of the constrained non-negative matrix factorization (CNMF) algorithm described by Pnevmatikakis et al., 2016, modified by Lu et al., 2018 for compatibilty with MATLAB2018 (Mathworks Inc., Natick, Massachusetts, USA). Original scripts downloaded from GitHub repository: https://github.com/JinghaoLu/MIN1PIPE om 12.12.2018.

The outputs are the relative intensities of each ROI over time. All following analysis was performed using custom made MATLAB2018 routines. Peaks were extracted for each trace using the build-in MATLAB command “findpeaks” specifying three criteria; firstly the peak height

(5xSTD+Mean), peak prominence(0.005 for astrocytic and 0.05 for neuronal ROIs), minimal distance between peaks. Only peaks fulfilling all three criteria were used for determining the peak frequency over time as well as the peak slope ratios. Electrophysiological data was analysed with custom made MATLAB2018 scripts applying fast fourier transformation (FFT filter, pass-band: 5–200 Hz) and subsequently processed with Welch's algorithm as described in detail by Hollnagel et al., 2015. The power spectral density (PSD) was plotted and the time points of stable gamma oscillations were determined manually.

Cross-correlation as well as the shuffling of data was completed with custom made MATLAB 2018 routines. For the cross correlation the build-in command "xcorr" was applied with the limited lag and normalization parameters. The shuffling of data was achieved by sectioning each relative fluorescence trace of both astrocytic and neuronal traces into snippets of random size and randomizing the snippets' order. This was repeated 1000 times for each astrocytic neuronal ROI pair with randomized snippet length.

4.6 Chemicals

Chemicals/Reagents	Manufacturer
2-Propanol	Merck KGaA, Darmstadt, Germany
Acetone	Merck KGaA, Darmstadt, Germany
Agarose	Thermo Fisher Scientific Inc., Waltham, USA
Ampicillin	Merck KGaA, Darmstadt, Germany
Aqua polymount	Polyscience, Warrington,USA
Atipamezol	Prodivet Pharmaceuticals, Rearen, Belgium
B27	Thermo Fisher Scientific Inc., Waltham, MA USA
Bacto tryptone	BD Bioscience advanced, USA
Bacto Yeast Extract	BD Bioscience advanced, USA
Bovine Serum Albumin	Merck KGaA, Darmstadt, Germany
Calcium chloride	Merck KGaA, Darmstadt, Germany
Carprofen	Norbrook, Newry, Ireland
DAPI	Serva Electrophoresis, Heidelberg
DMEM	Thermo Fisher Scientific Inc., Waltham, USA
DPBS	Thermo Fisher Scientific Inc., Waltham, USA

EBSS	Thermo Fisher Scientific Inc., Waltham, USA
Ethidium bromide	Serva Electrophoresis, Heidelberg
Ethylene glycol	Merck, Darmstadt
Fentanyl	Janssen-Cilag GmbH, Neuss, Germany
Fetal calf serum (FCS)	Thermo Fisher Scientific Inc., Waltham, USA
Flumazenil	Fresenius Kabi Deutschland, Bad Homburg, Germany
Glucose	Merck KGaA, Darmstadt, Germany
Glycerol	Carl Roth GmbH, Karlsruhe, Germany
Glycine	GERBU Biotechnik GmbH, Heidelberg, Germany
HEPES	GERBU Biotechnik GmbH, Heidelberg, Germany
Horse serum	Thermo Fisher Scientific Inc., Waltham, USA
Hydrochloric acid	Merck KGaA, Darmstadt, Germany
Hydrogen peroxide	Merck KGaA, Darmstadt, Germany
Isoflurane-Baxter	Baxter, Unterschleiheim
KCl	Merck KGaA, Darmstadt, Germany
Ketamine	CP Pharma, Burgdorf, Germany
KH2PO4	Merck KGaA, Darmstadt, Germany
Medetomidin	Vetpharma animal Health, Barcelona, Spain
MEM	Thermo Fisher Scientific Inc., Waltham, USA
MgCl2	Merck KGaA, Darmstadt, Germany
MgSO4	Merck KGaA, Darmstadt, Germany
Midazolam	Hameln pharma plus GmbH, Hameln, Germany
NaCl	Merck KGaA, Darmstadt, Germany
NaH2HPO4	Merck KGaA, Darmstadt, Germany
NaHCO3	Merck KGaA, Darmstadt, Germany
Naloxon	Inresa Arzneimittel GmbH, Freiburg, Germany
NaOH	Merck KGaA, Darmstadt, Germany
Neurobasal (NB) medium	Thermo Fisher Scientific Inc., Waltham, USA
Normal goat serum	Vector laboratories, Burlingame, USA
Paraformaldehyde 37%	Merck, Darmstadt
Ringer solution	B. Braun, Melsungen
Sucrose	Carl Roth GmbH, Karlsruhe, Germany
Tris	Merck KGaA, Darmstadt, Germany
TritonX-100	Merck KGaA, Darmstadt, Germany

Trypsin-EDTA	Thermo Fisher Scientific Inc., Waltham, USA
Xylocaine	Astra Zeneca GmbH, Wedel, Germany

5. References

Adamsky, A., Kol, A., Kreisel, T., Doron, A., Ozeri-Engelhard, N., Melcer, T., Refaeli, R., Horn, H., Regev, L., Groysman, M., et al. (2018). Astrocytic activation generates de novo neuronal potentiation and memory enhancement. Cell *174*, 59-71.e14.

Agarwal, A., Wu, P.-H., Hughes, E.G., Fukaya, M., Tischfield, M.A., Langseth, A.J., Wirtz, D., and Bergles, D.E. (2017). Transient opening of the mitochondrial permeability transition pore induces microdomain calcium transients in astrocyte processes. Neuron *93*, 587-605.e7.

Ahnaou, A., Huysmans, H., Van De Casteele, T., and Drinkenburg, W.H.I.M. (2017). Cortical high gamma network oscillations and connectivity: A translational index for antipsychotics to normalize aberrant neurophysiological activity. Transl. Psychiatry *7,*1285.

Albakri, M.B., Jiang, Y., Genereaux, J., and Lajoie, P. (2018). Polyglutamine toxicity assays highlight the advantages of mScarlet for imaging in Saccharomyces cerevisiae. F1000Research *7,*1242.

Allaman, I., Belanger, M., and Magistretti, P.J. (2011). Astrocyte-neuron metabolic relationships: for better and for worse. Trends Neurosci. *34*, 76–87.

Araque, A., Parpura, V., Sanzgiri, R.P., and Haydon, P.G. (1999). Tripartite synapses: glia, the unacknowledged partner. Trends Neurosci. *22*, 208–215.

Araque, A., Carmignoto, G., Haydon, P.G., Oliet, S.H.R., Robitaille, R., and Volterra, A. (2014). Gliotransmitters travel in time and space. Neuron *81*, 728–739.

Attwell, D., Buchan, A.M., Charpak, S., Lauritzen, M., Macvicar, B.A., and Newman, E.A. (2010). Glial and neuronal control of brain blood flow. Nature *468*, 232–243.

Bartos, M., Vida, I., and Jonas, P. (2007). Synaptic mechanisms of synchronized gamma oscillations in inhibitory interneuron networks. Nat. Rev. Neurosci. *8*, 45–56.

Bazargani, N., and Attwell, D. (2016). Astrocyte calcium signaling: the third wave. Nat. Neurosci. *19*, 182–189.

Bekar, L.K., and Walz, W. (1999). Evidence for chloride ions as intracellular messenger substances in astrocytes. J. Neurophysiol. *82*, 248–254.

Von Bernhardi, R. (2007). Glial cell dysregulation: A new perspective on Alzheimer disease. Neurotox. Res. *12*, 215–232.

Bindocci, E., Savtchouk, I., Liaudet, N., Becker, D., Carriero, G., and Volterra, A. (2017). Three-dimensional Ca^{2+} imaging advances understanding of astrocyte biology. Science *356*, eaai8185.

Bragin, A., Jando, G., Nadasdy, Z., Hetke, J., Wise, K., and Buzsaki, G. (1995). Gamma (40-100 Hz) oscillation in the hippocampus of the behaving rat. J. Neurosci. *15*, 47–60.

Bruzzone, R., Hormuzdi, S.G., Barbe, M.T., Herb, A., and Monyer, H. (2003). Pannexins, a family of gap junction proteins expressed in brain. Proc. Natl. Acad. Sci. *100*, 13644–13649.

Buettner-Ennever, J., Grob, P., Akert, K., and Bizzini, B. (1981). Transsynaptic retrograde labeling in the oculomotor system of the monkey with [125I]tetanus toxin BIIb fragment. Neurosci. Lett. *26*, 233–238.

Bundgaard, M., and Abbott, N.J. (2008). All vertebrates started out with a glial blood-brain barrier 4–500 million years ago. Glia *56*, 699–708.

Bushong, E. a, Martone, M.E., Jones, Y.Z., and Ellisman, M.H. (2002). Protoplasmic astrocytes in CA1 stratum radiatum occupy separate anatomical domains. J. Neurosci. *22*, 183–192.

Buzsaki, G. (2006). Rhythms of the Brain (Oxford University Press).p.231ff

Buzsaki, G., and Draguhn, A. (2004). Neuronal Oscillations in Cortical Networks. Science *304*, 1–4.

Callaway, E.M. (2005). A molecular and genetic arsenal for systems neuroscience. Trends Neurosci. *28*, 196–201.

Di Castro, M.A., Chuquet, J., Liaudet, N., Bhaukaurally, K., Santello, M., Bouvier, D., Tiret, P., and Volterra, A. (2011). Local Ca2+ detection and modulation of synaptic release by astrocytes. Nat. Neurosci. *14*, 1276–1284.

Chever, O., Dossi, E., Pannasch, U., Derangeon, M., and Rouach, N. (2016). Astroglial networks promote neuronal coordination. Sci. Signal. *9*, ra6.

Coen, L., Osta, R., Maury, M., and Brûlet, P. (1997). Construction of hybrid proteins that migrate retrogradely and transynaptically into the central nervous system. Proc. Natl. Acad. Sci. U. S. A. *94*, 9400–9405.

Cornell-Bell, A., Finkbeiner, S., Cooper, M., and Smith, S. (1990). Glutamate induces calcium waves in cultured astrocytes: long-range glial signaling. Science *247*, 470–473.

Craig, A.M., and Kang, Y. (2007). Neurexin–neuroligin signaling in synapse development. Curr. Opin. Neurobiol. *17*, 43–52.

Csicsvari, J., Jamieson, B., Wise, K.D., and Buzsáki, G. (2003). Mechanisms of gamma oscillations in the hippocampus of the behaving rat. Neuron *37*, 311–322.

D'Ambrosio, R., Wenzel, J., Schwartzkroin, P.A., McKhann, G.M., and Janigro, D. (1998). Functional specialization and topographic segregation of hippocampal astrocytes. J. Neurosci. *18*, 4425–4438.

Dallérac, G., Zapata, J., and Rouach, N. (2018). Versatile control of synaptic circuits by astrocytes: where, when and how? Nat. Rev. Neurosci. *19*, 729–743.

Dermietzel, R., Traub, O., Hwang, T.K., Beyer, E., Bennett, M. V, Spray, D.C., and Willecke, K.

(1989). Differential expression of three gap junction proteins in developing and mature brain tissues. Proc. Natl. Acad. Sci. *86*, 10148–10152.

Deshpande, A., Bergami, M., Ghanem, A., Conzelmann, K.-K., Lepier, A., Gotz, M., and Berninger, B. (2013). Retrograde monosynaptic tracing reveals the temporal evolution of inputs onto new neurons in the adult dentate gyrus and olfactory bulb. Proc. Natl. Acad. Sci. *110*, E1152–E1161.

Ding, F., O'Donnell, J., Thrane, A.S., Zeppenfeld, D., Kang, H., Wang, F., and Nedergaard, M. (2013). α1-adrenergic receptors mediate coordinated Ca2+ signaling of cortical astrocytes in awake, behaving mice. Cell Calcium *54*.

Djukic, B., Casper, K.B., Philpot, B.D., Chin, L.-S., and McCarthy, K.D. (2007). conditional knock-out of kir4.1 leads to glial membrane depolarization, inhibition of potassium and glutamate uptake, and enhanced short-term synaptic potentiation. J. Neurosci. *27*, 11354–11365.

Durand, S., and Cimarelli, A. (2011). The inside out of lentiviral vectors. Viruses *3*, 132–159.

During, M., Young, D., Baer, K., Lawlor, P., and Klugmann, M. (2003). Development and optimization of adeno-associated virus vector transfer into the central nervous system. Methods Mol.Med. *76,*221-36

Fellin, T., Halassa, M.M., Terunuma, M., Succol, F., Takano, H., Frank, M., Moss, S.J., and Haydon, P.G. (2009). Endogenous nonneuronal modulators of synaptic transmission control cortical slow oscillations in vivo. Proc. Natl. Acad. Sci. U. S. A. *106*, 15037–15042.

Fellous, J.-M., and Sejnowski, T.J. (2000). Cholinergic induction of oscillations in the hippocampal slice in the slow (0.5–2 Hz), theta (5–12 Hz), and gamma (35–70 Hz) bands. Hippocampus *10*, 187–197.

Fiacco, T., and McCarthy, K.D. (2018). multiple lines of evidence indicate that gliotransmission does not occur under physiological conditions. J. Neurosci. *38*, 3–13.

Fiacco, T., Agulhon, C., Taves, S.R., Petravicz, J., Casper, K.B., Dong, X., Chen, J., and McCarthy, K.D. (2007). Selective stimulation of astrocyte calcium in situ does not affect neuronal excitatory synaptic activity. Neuron *54*, 611–626.

Fisahn, A., Pike, F.G., Buhl, E.H., and Paulsen, O. (1998). Cholinergic induction of network oscillations at 40 Hz in the hippocampus in vitro. Lett. to Nat. *394*, 3–6.

Fisahn, A., Contractor, A., Traub, R.D., Buhl, E.H., Heinemann, S.F., and McBain, C.J. (2004). distinct roles for the kainate receptor subunits glur5 and glur6 in kainate-induced hippocampal gamma oscillations. J. Neurosci. *24*, 9658–9668.

Freeman, M.R. (2010). Specification and morphogenesis of astrocytes. Science *330*, 774–778.

Fushiki, D., Yoshimura, R., and Endo, Y. (2010). Immunocytochemical study of gap junction-related protein, innexin 2, in Periplaneta americana (Blattodea: Blattidae). Appl. Entomol. Zool.

45, 245–251.

Giaume, C., Koulakoff, A., Roux, L., Holcman, D., and Rouach, N. (2010). Astroglial networks: a step further in neuroglial and gliovascular interactions. Nat. Rev. Neurosci. *11*, 87–99.

Ginger, M., Haberl, M., Conzelmann, K.-K., Schwarz, M.K., and Frick, A. (2013). Revealing the secrets of neuronal circuits with recombinant rabies virus technology. Front. Neural Circuits *7*, 2.

Glykys, J., and Mody, I. (2007). Activation of GABAA receptors: views from outside the synaptic cleft. Neuron *56*, 763–770.

Haberl, M.G., Viana da Silva, S., Guest, J.M., Ginger, M., Ghanem, A., Mulle, C., Oberlaender, M., Conzelmann, K.K., and Frick, A. (2015). An anterograde rabies virus vector for high-resolution large-scale reconstruction of 3D neuron morphology. Brain Struct. Funct. *220*, 1369–1379.

Hájos, N., Katona, I., Naiem, S.S., Mackie, K., Ledent, C., Mody, I., and Freund, T.F. (2000). Cannabinoids inhibit hippocampal GABAergic transmission and network oscillations. Eur. J. Neurosci. *12*, 3239–3249.

Henneberger, C., Papouin, T., Oliet, S.H.R., and Rusakov, D. a (2010). Long-term potentiation depends on release of D-serine from astrocytes. Nature *463*, 232–236.

Herreros, J., Lalli, G., Montecucco, C., and Schiavo, G. (2000a). Tetanus toxin fragment C binds to a protein present in neuronal cell lines and motoneurons. J. Neurochem. *74*, 1941–1950.

Herreros, J., Lalli, G., and Schiavo, G. (2000b). C-terminal half of tetanus toxin fragment C is sufficient for neuronal binding and interaction with a putative protein receptor. Biochem. J. *347 Pt 1*, 199–204.

Hollnagel, J.O., Haq U., Behrens R., Maslarova C.J., Mody A.I., and Heinemann, U. (2015). No evidence for role of extracellular choline-acetyltransferase in generation of gamma oscillations in rat hippocampal slices in vitro. Neuroscience *284*, 459–469.

Howland, J.L. (1996). Short protocols in molecular biology, third edition: Edited by F Ausubel, R Brent, R E Kingston, D D Moore, J G Seidman, J A Smith and K Struhl. P 836. John Wiley & Sons, New York. 1996. Biochem. Educ. *24*, 68.

Iadecola, C., and Nedergaard, M. (2007). Glial regulation of the cerebral microvasculature. Nat. Neurosci. *10*, 1369.

Jahn, R., and Südhof, T.C. (1999). Membrane Fusion and Exocytosis. Annu. Rev. Biochem. *68*, 863–911.

Jayant, K., Hirtz, J.J., Plante, I.J.-L., Tsai, D.M., De Boer, W.D.A.M., Semonche, A., Peterka, D.S., Owen, J.S., Sahin, O., Shepard, K.L., et al. (2017). Targeted intracellular voltage recordings from dendritic spines using quantum-dot-coated nanopipettes. Nat. Nanotechnol. *12*, 335–342.

Ji, D., and Wilson, M.A. (2007). Coordinated memory replay in the visual cortex and

hippocampus during sleep. Nat. Neurosci. *10*, 100–107.

Jourdain, P., Bergersen, L.H., Bhaukaurally, K., Bezzi, P., Santello, M., Domercq, M., Matute, C., Tonello, F., Gundersen, V., and Volterra, A. (2007). Glutamate exocytosis from astrocytes controls synaptic strength. Nat. Neurosci. *10*, 331–339.

Kettenmann, H., and Ransom, B. (2005). History of Neuroglia. In Neuroglia, H. Kettenmann, and B. Ransom, eds. (Oxford: Oxford University Press, New York), p.5ff

Kissa, K., Mordelet, E., Soudais, C., Kremer, E.J., Demeneix, B. a, Brûlet, P., and Coen, L. (2002). In vivo neuronal tracing with gfp-ttc gene delivery. Mol. Cell. Neurosci. *20*, 627–637.

Lalli, G., Bohnert, S., Deinhardt, K., Verastegui, C., and Schiavo, G. (2003). The journey of tetanus and botulinum neurotoxins in neurons. Trends Microbiol. *11*, 431–437.

Lee, C.H., and Ruben, P.C. (2008). Interaction between voltage-gated sodium channels and the neurotoxin, tetrodotoxin. Channels *2*, 407–412.

Lee, H.S., Ghetti, A., Pinto-Duarte, A., Wang, X., Dziewczapolski, G., Galimi, F., Huitron-Resendiz, Ss., Pina-Crespo, J.C., Roberts, A.J., Verma, I.M., et al. (2014). Astrocytes contribute to gamma oscillations and recognition memory. Proc. Natl. Acad. Sci. *32*, E3343–E3352.

Lu, J., Li, C., Singh-Alvarado, J., Zhou, Z.C., Fröhlich, F., Mooney, R., and Wang, F. (2018). MIN1PIPE: A miniscope 1-photon-based calcium imaging signal extraction pipeline. Cell Rep. *23*, 3673–3684.

Mazarakis, N.D., Azzouz, M., Rohll, J.B., Ellard, F.M., Wilkes, F.J., Olsen, A.L., Carter, E.E., Barber, R.D., Baban, D.F., Kingsman, S.M., et al. (2001). Rabies virus glycoprotein pseudotyping of lentiviral vectors enables retrograde axonal transport and access to the nervous system after peripheral delivery. Hum. Mol. Genet. *10*, 2109–2121.

Medina, J.M., Tabernero, A., and Giaume, C. (1999). Metabolic coupling and the role played by astrocytes in energy distribution and homeostasis. In The Functional Roles of Glial Cells in Health and Disease, (Springer), pp. 361–371.

Miana-Mena, F.J., Roux, S., Benichou, J.-C., Osta, R., and Brûlet, P. (2002). Neuronal activity-dependent membrane traffic at the neuromuscular junction. Proc. Natl. Acad. Sci. *99*, 3234–3239.

Miller, S.J., Philips, T., Kim, N., Dastgheyb, R., Chen, Z., Hsieh, Y.C., Daigle, J.G., Datta, M., Chew, J., Vidensky, S., et al. (2019). Molecularly defined cortical astroglia subpopulation modulates neurons via secretion of Norrin. Nat. Neurosci. *22*, 741–752.

Min, R., and Nevian, T. (2012). Astrocyte signaling controls spike timing–dependent depression at neocortical synapses. Nat. Neurosci. *15*, 746.

Mulligan, S.J., and MacVicar, B.A. (2004). Calcium transients in astrocyte endfeet cause

cerebrovascular constrictions. Nature *431*, 195–199.

Munro, P., Kojima, H., Dupont, J.L., Bossu, J.L., Poulain, B., and Boquet, P. (2001). High sensitivity of mouse neuronal cells to tetanus toxin requires a GPI-anchored protein. Biochem. Biophys. Res. Commun. *289*, 623–629.

Nakai, J., Ohkura, M., and Imoto, K. (2001). A high signal-to-noise Ca(2+) probe composed of a single green fluorescent protein. Nat. Biotechnol. *19*, 137–141.

Nimmerjahn, A., Mukamel, E. a, and Schnitzer, M.J. (2009). Motor behavior activates Bergmann glial networks. Neuron *62*, 400–412.

Nizar, K., Uhlirova, H., Tian, P., Saisan, P.A., Cheng, Q., Reznichenko, L., Weldy, K.L., Steed, T.C., Sridhar, V.B., MacDonald, C.L., et al. (2013). In vivo stimulus-induced vasodilation occurs without ip3 receptor activation and may precede astrocytic calcium increase. J. Neurosci. *33*, 8411 LP – 8422.

Osakda, F., Mori, T., Cetin, A.H., Marshel, J.H., Virgen, B., and Callaway, E.M. (2012). New rabies virus variants for monitoring and manipulating activity and gene expression in defined neural circuits. Neuron *71*, 617–631.

Panatier, A., and Robitaille, R. (2018). Astrocytic mGluR5 and the tripartite synapse. Nat. Commun. *323*, 29–34.

Panatier, A., Vallée, J., Haber, M., Murai, K.K., Lacaille, J.C., and Robitaille, R. (2011). Astrocytes are endogenous regulators of basal transmission at central synapses. Cell *146*, 785–798.

Pannasch, U., and Rouach, N. (2013). Emerging role for astroglial networks in information processing: From synapse to behavior. Trends Neurosci. *36*, 405–417.

Papouin, T., Dunphy, J.M., Tolman, M., Dineley, K.T., and Haydon, P.G. (2017). septal cholinergic neuromodulation tunes the astrocyte-dependent gating of hippocampal nmda receptors to wakefulness. Neuron *94*, 840-854.

Pascual, O., Casper, K.B., Kubera, C., Zhang, J., Revilla-Sanchez, R., Sul, J.-Y., Takano, H., Moss, S.J., McCarthy, K., and Haydon, P.G. (2005). Astrocytic purinergic signaling coordinates synaptic networks. Science *310*, 113–116.

Paukert, M., Agarwal, A., Cha, J., Doze, V.A., Kang, J.U., and Bergles, D.E. (2014). Norepinephrine controls astroglial responsiveness to local circuit activity. Neuron *82*, 1263–1270.

Perreault, M.C., Bernier, A.P., Renaud, J.S., Roux, S., and Glover, J.C. (2006). C fragment of tetanus toxin hybrid proteins evaluated for muscle-specific transsynaptic mapping of spinal motor circuitry in the newborn mouse. Neuroscience *141*, 803–816.

Petersen, O.H., Michalak, M., and Verkhratsky, A. (2005). Calcium signalling: past, present and future. Cell Calcium *38*, 161–169.

Petravicz, J., Fiacco, T.A., and McCarthy, K.D. (2008). Loss of IP3 receptor-dependent Ca2+ increases in hippocampal astrocytes does not affect baseline CA1 pyramidal neuron synaptic activity. J. Neurosci. *28*, 4967–4973.

Petravicz, J., Boyt, K.M., and McCarthy, K.D. (2014). Astrocyte IP3R2-dependent Ca2+ signaling is not a major modulator of neuronal pathways governing behavior. Front. Behav. Neurosci. *8*, 1–13.

Pirttimaki, T.M., Sims, R.E., Saunders, G., Antonio, S.A., Codadu, N.K., and Parri, H.R. (2017). Astrocyte mediated neuronal synchronisation properties revealed by false gliotransmitter release. J. Neurosci. *37*, 9859–9870.

Pnevmatikakis, E.A., Soudry, D., Gao, Y., Machado, T.A., Merel, J., Pfau, D., Reardon, T., Mu, Y., Lacefield, C., Yang, W., et al. (2016). Simultaneous Denoising, Deconvolution, and Demixing of Calcium Imaging Data. Neuron *89*, 285–299.

Porter, J.T., and McCarthy, K.D. (1996). Hippocampal astrocytes in situ respond to glutamate released from synaptic terminals. J. Neurosci. *16*, 5073–5081.

Poskanzer, K.E., and Molofsky, A. V (2018). Dynamism of an astrocyte in vivo: Perspectives on identity and function. Annu. Rev. Physiol. *80*, 143–157.

Poskanzer, K.E., and Yuste, R. (2016). Astrocytes regulate cortical state switching in vivo. Proc. Natl. Acad. Sci. *2016*, 1–10.

Prada, J., Sasi, M., Martin, C., Jablonka, S., Dandekar, T., and Blum, R. (2018). An open source tool for automatic spatiotemporal assessment of calcium transients and local 'signal-close-to-noise'activity in calcium imaging data. PLoS Comput. Biol. *14*, e1006054.

Price, D.L., Griffin, J., Young, A., Peck, K., and Stocks, A. (1975). Tetanus toxin: direct evidence for retrograde intraaxonal transport. Science *188*, 945–947.

Rancz, E.A., Franks, K.M., Schwarz, M.K., Pichler, B., Schaefer, A.T., and Margrie, T.W. (2011). Transfection via whole-cell recording in vivo: Bridging single-cell physiology, genetics and connectomics. Nat. Neurosci. *14*, 527–532.

Reinert, J.K. (2012). Characterization of recombinant AAV serotypes in the mouse olfactory bulb and cortex, Masters Thesis, University Heidelberg

Reinert, J.K., Sonntag, I., Sonntag, H., Sprengel, R., Pelzer, P., Lessle, S., Kaiser, M., and Kuner, T. (2019). retroLEAP: rAAV-based retrograde trans-synaptic labeling, expression and perturbation. BioRxiv.

Roux, S., Saint Cloment, C., Curie, T., Girard, E., Mena, F.J.M., Barbier, J., Osta, R., Molgó, J., and Brûlet, P. (2006). Brain-derived neurotrophic factor facilitates in vivo internalization of tetanus neurotoxin C-terminal fragment fusion proteins in mature mouse motor nerve terminals. Eur. J.

Neurosci. *24*, 1546–1554.

Schnell, M.J., McGettigan, J.P., Wirblich, C., and Papaneri, A. (2010). The cell biology of rabies virus: Using stealth to reach the brain. Nat. Rev. Microbiol. *8*, 51–61.

Schwarz, M.K., Scherbarth, A., Sprengel, R., Engelhardt, J., Theer, P., and Giese, G. (2015). Fluorescent-protein stabilization and high-resolution imaging of cleared, intact mouse brains. PLoS One *10*, 1–26.

Schwarz, Y., Zhao, N., Kirchhoff, F., and Bruns, D. (2017). Astrocytes control synaptic strength by two distinct v-SNARE-dependent release pathways. Nat. Neurosci. *20*, 1529–1539.

Shelton, M.K., and Mccarthy, K.D. (2000). Hippocampal astrocytes exhibit Ca2+-elevating muscarinic cholinergic and histaminergic receptors in situ. J. Neurochem. *74*, 555–563.

Shemiakina, I.I., Ermakova, G. V, Cranfill, P.J., Baird, M.A., Evans, R.A., Souslova, E.A., Staroverov, D.B., Gorokhovatsky, A.Y., Putintseva, E. V, Gorodnicheva, T. V, et al. (2012). A monomeric red fluorescent protein with low cytotoxicity. Nat. Commun. *3*, 1204.

Shigetomi, E., Bushong, E.A., Haustein, M.D., Tong, X., Jackson-Weaver, O., Kracun, S., Xu, J., Sofroniew, M. V, Ellisman, M.H., and Khakh, B.S. (2013). Imaging calcium microdomains within entire astrocyte territories and endfeet with GCaMPs expressed using adeno-associated viruses. J. Gen. Physiol. *141*, 633–647.

Shigetomi, E., Patel, S., and Khakh, B.S. (2016). Probing the complexities of astrocyte calcium signaling. Trends Cell Biol. *26*, 300–312.

Shute, C. C.D., and Lewis, P.R. (1963). Cholinesterase-containing systems of the brain of the rat. Nature *199*, 1160–1164.

Srinivasan, R., Huang, B.S., Venugopal, S., Johnston, A.D., Chai, H., Zeng, H., Golshani, P., and Khakh, B.S. (2015). Ca2+ signaling in astrocytes from Ip3r2−/− mice in brain slices and during startle responses in vivo. Nat. Neurosci. *18*, 708-717.

Srinivasan, R., Lu, T.-Y., Chai, H., Xu, J., Huang, B.S., Golshani, P., Coppola, G., and Khakh, B.S. (2016). New transgenic mouse lines for selectively targeting astrocytes and studying calcium signals in astrocyte processes in situ and in vivo. Neuron *92*,1181-1195.

Steriade, M. (2001). Impact of network activities on neuronal properties in corticothalamic systems. J. Neurophysiol. *86*, 1–39.

Takata, N., Mishima, T., Hisatsune, C., Nagai, T., Ebisui, E., Mikoshiba, K., and Hirase, H. (2011). Astrocyte Calcium Signaling Transforms Cholinergic Modulation to Cortical Plasticity In Vivo. J. Neurosci. *31*, 18155–18165.

Tang, W., Szokol, K., Jensen, V., Enger, R., Trivedi, C. a, Hvalby, Ø., Helm, P.J., Looger, L.L., Sprengel, R., and Nagelhus, E. A. (2015). Stimulation-evoked Ca2+ signals in astrocytic processes

at hippocampal CA3-CA1 synapses of adult mice are modulated by glutamate and ATP. J. Neurosci. *35*, 3016–3021.

Taylor, A.R., Robinson, M.B., Gifondorwa, D.J., Tytell, M., and Milligan, C.E. (2007). Regulation of heat shock protein 70 release in astrocytes: Role of signaling kinases. Dev. Neurobiol. *67*, 1815–1829.

Tervo, D.G.R., Hwang, B.Y., Viswanathan, S., Gaj, T., Lavzin, M., Ritola, K.D., Lindo, S., Michael, S., Kuleshova, E., Ojala, D., et al. (2016). A designer AAV variant permits efficient retrograde access to projection neurons. Neuron *92*, 372–382.

Theis, M., Söhl, G., Eiberger, J., and Willecke, K. (2005). Emerging complexities in identity and function of glial connexins. Trends Neurosci. *28*, 188–195.

Traub, R.D., Kopell, N., Bibbig, A., Buhl, E.H., LeBeau, F.E., and Whittington, M.A. (2001). Gap junctions between interneuron dendrites can enhance synchrony of gamma oscillations in distributed networks. J. Neurosci. *21*, 9478–9486.

Tsai, H.-H., Li, H., Fuentealba, L.C., Molofsky, A. V, Taveira-Marques, R., Zhuang, H., Tenney, A., Murnen, A.T., Fancy, S.P.J., Merkle, F., et al. (2012). Regional astrocyte allocation regulates CNS synaptogenesis and repair. Science *337*, 358 – 362.

Ventura, R., and Harris, K.M. (1999). Three-dimensional relationships between hippocampal synapses and astrocytes. J. Neurosci. *19*, 6897–6906.

Verkhratsky, A., and Nedergaard, M. (2017). Physiology of astroglia. Physiol. Rev. *98*, 239–389.

Verkhratsky, A., and Parpura, V. (2013). Calcium signaling in neuroglia. In Neuroglia, H. Kettenmann, and B. Ransom, eds. (Oxford University Press, New York), p. 320ff.

Volterra, A., and Steinhäuser, C. (2004). Glial modulation of synaptic transmission in the hippocampus. Glia *47*, 249–257.

Wallraff, A., Köhling, R., Heinemann, U., Theis, M., Willecke, K., and Steinhäuser, C. (2006). The impact of astrocytic gap junctional coupling on potassium buffering in the hippocampus. J. Neurosci. *26*, 5438 – 5447.

Wang, Y., Wang, F., Wang, R., Zhao, P., and Xia, Q. (2015). 2A self-cleaving peptide-based multi-gene expression system in the silkworm Bombyx mori. Sci. Rep. *5,* 16273.

Whittington, M.A., Traub, R.D., and Jefferys, J.G.R. (1995). Synchronized oscillations in interneuron networks driven by metabotropic glutamate receptor activation. Nature *373*, 612–615.

Wickersham, I.R., Lyon, D.C., Barnard, R.J.O., Mori, T., Conzelmann, K., Young, J. a T., and Callaway, E.M. (2009). monosynaptic restriction of transsynaptic tracing from single, genetically targeted neurons. Neuron *53*, 639–647.

Witter, M.P. (1993). Organization of the entorhinal-hippocampal system: a review of current anatomical data. Hippocampus *3*, 33–44.

Yon, J., and Fried, M. (1989). Precise gene fusion by PCR. Nucleic Acids Res. *17*, 4895.

Zhang, Q., Pangršič, T., Kreft, M., Kržan, M., Li, N., Sul, J.Y., Halassa, M., Van Bockstaele, E., Zorec, R., and Haydon, P.G. (2004). Fusion-related release of glutamate from astrocytes. J. Biol. Chem. *279*, 12724–12733.

Zingg, B., Chou, X. lin, Zhang, Z. gang, Mesik, L., Liang, F., Tao, H.W., and Zhang, L.I. (2017). AAV-mediated anterograde transsynaptic tagging: mapping corticocollicular input-defined neural pathways for defense behaviors. Neuron *93*, 33–47.

Acknowledgements

It would not have been possible to complete this PhD thesis without the support, encouragement and inspiration of many people, whom I want to thank here.

First of all I want to sincerely thank my advisor Dr. Rolf Sprengel for giving me the opportunity to work in his lab. He gave me guidance throughout the course of my PhD and fostered critical thinking and independence. Moreover, I want to thank Rolf Sprengel for conceptualizing the calcium imaging project. I am also deeply thankful to Prof. Dr. Andreas Draguhn for accepting me as his PhD student and appreciate his participation in evaluating this work as well as for being a member of my TAC. Moreover, I want to thank Andreas for initiating the DFG grant "SFB1134" which provided funding for this project and my position. I also want to thank Dr. Ana Oliveira and Prof. Dr. Christoph Schuster for being a member in my committee and for participating in the evaluation of this work.

I thank Annette Herold for providing technical assistance and help with anything in the lab and for being such a warmhearted person. I also want to thank Michaela Kaiser for helping me out with cloning work and advice when my cloning just would not work. Also very important for the daily work were all the past and present members of the "Sprengel-group"; Ahmed Eltokhi, Thorsten Bus, Ilaria Bertocchi, Desiree Ditzel and Timm Hondrich. I thank all of you for helping out with little things and nice words during the everyday challenges one faces in the lab.

I want to thank all the people at the Institute of Anatomy in the department for cellular biology as well as the functional neuroanatomy department who welcomed me and provided an excellent work environment as well as generous access to lab equipment, when we moved over from Max Planck Institute at the beginning of my PhD. Especially, I want to thank Mirka Kokocinska for being a great office-mate. Furthermore, I want to thank Janine Reinert and Ivo Sonntag for initiating the exciting "TTC-project" and for being great collaborations partners and for multiple rounds of proof-reading this thesis. I also have to thank Oliver Kann, Justus Schneider, Shehab Elzoheiry, Jan-Oli Hollnagel and Andrea Lewen from the Physiology department for not only collaborating with me for the calcium imaging but also for vivid exchange on problems and advices and for making this a very pleasant project. Similarly, I want to thank Elke Kirschbaum from IWR for the excellent collaboration on the analysis of calcium imaging data and for helping me out with questions about cross-correlations. Many thanks to Martin Both for his help in the analysis of my data and many advising sessions over mensa food as well as his general mentorship not only regarding life science. I also appreciate the in- and

output from all the members of the calcium imaging club who participated in creating a calcium imaging network in Heidelberg neuroscience community.

I thank all my friends from Heidelberg and the Bergstrasse, some of which accompanying me since the first semester and longer: Selina Kaiser, Naja Benz, Jakob Trendel, Jule Buhmann, Simon Gottwalt, Sam Corless and Nezha Benabdallah and all the Oberdoerfler. I am deeply thankful for their friendship and constant support through years of studies and this PhD.

Most importantly I wish to thank my family, my parents Ruth und Volker, my sisters Sarah and Annika (and husbands Frank and Christoph). I feel deeply privileged to have grown up in such a warm and loving family. You are the best family I can imagine. Furthermore, I want to thank my in-law-family Margarete and Andi as well as my sister-in-law Elsa and Paul, for your support through years of studies. You always listened to my problems and helped with words and deeds and made this work possible. This dissertation would not have been possible without my new-built family; my husband Ivo Sonntag. I thank you for loving me, believing in me and supporting me and for offering valuable and professional advice throughout the PhD. Without your encouragement I would not have finished this thesis.